Systems Health Management and Prognosis using

Physics Based Modeling and Machine Learning

by

Rajesh Kumar Neerukatti

A Dissertation Presented in Partial Fulfillment
of the Requirements for the Degree
Doctor of Philosophy

Approved July 2016 by the
Graduate Supervisory Committee:

Aditi Chattopadhyay, Chair
Hanqing Jiang
Yongming Liu
John Rajadas
Masoud Yekani Fard

ARIZONA STATE UNIVERSITY

August 2016

ABSTRACT

There is a concerted effort in developing robust systems health monitoring/management (SHM) technology as a means to reduce the life cycle costs, improve availability, extend life and minimize downtime of various platforms including aerospace and civil infrastructure. The implementation of a robust SHM system requires a collaborative effort in a variety of areas such as sensor development, damage detection and localization, physics based models, and prognosis models for residual useful life (RUL) estimation. Damage localization and prediction is further complicated by geometric, material, loading, and environmental variabilities. Therefore, it is essential to develop robust SHM methodologies by taking into account such uncertainties. In this research, damage localization and RUL estimation of two different physical systems are addressed: (i) fatigue crack propagation in metallic materials under complex multiaxial loading and (ii) temporal scour prediction near bridge piers. With little modifications, the methodologies developed can be applied to other systems.

Current practice in fatigue life prediction is based on either physics based modeling or data-driven methods, and is limited to predicting RUL for simple geometries under uniaxial loading conditions. In this research, crack initiation and propagation behavior under uniaxial and complex biaxial fatigue loading is addressed. The crack propagation behavior is studied by performing extensive material characterization and fatigue testing under in-plane biaxial loading, both in-phase and out-of-phase, with different biaxiality ratios. A hybrid prognosis model, which combines machine learning with physics based modeling, is developed to account for the uncertainties in crack

i

propagation and fatigue life prediction due to variabilities in material microstructural characteristics, crack localization information and environmental changes. The methodology iteratively combines localization information with hybrid prognosis models using sequential Bayesian techniques. The results show significant improvements in the localization and prediction accuracy under varying temperature.

For civil infrastructure, especially bridges, pier scour is a major failure mechanism. Currently available techniques are developed from a design perspective and provide highly conservative scour estimates. In this research, a fully probabilistic scour prediction methodology is developed using machine learning to accurately predict scour in real-time under varying flow conditions.

To my family,

especially my mom and dad,

for their continual support, inspiration, and patience

ACKNOWLEDGMENTS

TABLE OF CONTENTS

LIST OF TABLES

LIST OF FIGURES

Figure   Page

Figure   Page

Figure   Page

1   INTRODUCTION

1.1   Motivation

Systems health monitoring/management (SHM) and prognosis is an emerging research area critical to both current and future multidisciplinary problems for aerospace and civil infrastructures (Coelho, Das, Chattopadhyay, Papandreou-Suppappola, & Peralta, 2007; Farrar & Worden, 2007; Giurgiutiu, 2007; Hensberry, Kovvali, & Chattopadhyay, 2013; Yongming Liu & Mahadevan, 2007a, 2009; Subhasish Mohanty, Chattopadhyay, & Peralta, 2010). A comprehensive SHM framework consists of (i) multiscale modeling, (ii) damage localization, and (iii) prognosis. The goal of an SHM framework is to detect and localize damage in a structure to assess the current state and predict the residual useful life (RUL). An integrated framework for SHM of metallic structures that includes multiscale modeling, localization, and prognosis has been developed by Chattopadhyay et al. (2009). However, a comprehensive generalized framework to transfer information (back and forth) between each of the three components of the SHM framework is not available. Damage localization and prognosis are generally considered as two separate tasks in the SHM framework, and the information transfer is always in one direction (from localization to prognosis). Localization provides an estimate of the size and location of damage, and prognosis models are used to predict how this damage evolves over time. For real-time applications, the localization algorithms, which are computationally expensive, will have to be run continuously even when the structure is not damaged, since there is no prior information about the damage initiation. To resolve this issue, multiscale modeling can be used to predict the number of

1

fatigue cycles for damage initiation, and the localization algorithms can then be run based on the results of multiscale modeling.

Available localization techniques (Hensberry et al., 2013) use a generic fixed prior, which leads to low accuracy and high uncertainty in damage estimates. As a result, there is a need to develop an integrated methodology that transfers information easily between the individual components of the SHM framework. One of the methodologies developed in this dissertation is to use the information from prognosis prior to the localization algorithm, which will significantly improve the localization accuracy. Since the methodology highly depends on the results of the prognosis model, there is a need to develop a highly robust prognosis model capable of predicting damage under complex uniaxial and biaxial loading. Physics-based models provide accurate fatigue life predictions for simple geometries under uniaxial loading. For complex geometries and random loading conditions, closed form solutions are often unavailable. Therefore, machine learning techniques, which learn from the available data, will be helpful in making accurate predictions for complex geometries under complex uniaxial and biaxial loading conditions. A generalized SHM framework should also be capable of being applied to completely different applications, such as civil infrastructure, with very little modification to the algorithm.

Bridge scour is the removal of sediments around bridge piers due to the turbulent horseshoe vortices created by the flowing water, and it is the most common cause of highway bridge failures in the United States (Mueller & Wagner, 2005). However, predicting the scour near bridge piers is a very complex problem. Most of the scour prediction techniques are based on the design (predicting the maximum possible scour

2

over a 100-year period), and there are currently no techniques available for real-time scour prediction. Therefore, the algorithms developed for fatigue life prediction in aluminum alloys can be modified to predict the temporal scour near bridge piers.

In this thesis, effort has been dedicated to developing a generalized SHM framework to accurately detect and predict damage under a variety of loading conditions. Damage detection and prediction in two different physical systems are studied: (i) fatigue crack propagation in metallic materials under complex multiaxial loading and (ii) temporal scour prediction near bridge piers. Specifically, a sequential Bayesian framework for integrating damage detection algorithms with damage prediction algorithms is developed. The background of relevant research is discussed in Section 1.2 and Section 1.3.

1.2   Background of Material Characterization and Fatigue Life Prediction in Metals

Accurate estimation of fatigue life of metallic components under complex loading conditions is critical to the safety and reliability of aerospace vehicles. The majority of currently available fatigue life prediction models (Grell & Laz, 2010; J. Harter, 2004; J. Newman, 1982; J. C. Newman Jr., 1992; J. C. N. Newman, 1984; Ray & Patankar, 2001a, 2001b; Zapatero & Domínguez, 1990) are deficient in predicting damage in complex structures under random or flight profile service loads. The inherent inaccuracy in these models is due to the stochastic nature of crack propagation in metallic structures. A significant amount of work has been reported on the development of reliable prognostic frameworks. These approaches are either physics based or purely data-driven. Current research primarily focuses on integrating machine learning techniques with

3

physics-based models to make accurate predictions. Machine learning techniques do not use physics-based information, making their prediction accuracy inferior to those based on physics, particularly when there is sparse data or incomplete knowledge. Physics-based approaches, on the other hand, are also inadequate because they have difficulty adapting to variations due to material scatter, environmental changes, and other unclassifiable but significant sources of noise. Thus, a hybrid prognostic model, which uses a synergetic fusion of physics-based modeling information and data-driven machine learning algorithms (Tibshirani, 2011; Tipping, 2001), is expected to provide more accurate and reliable information on damage prognosis and RUL.

For a specimen under uniaxial constant amplitude loading, the fatigue crack growth phenomena can be captured using Paris' Law (Paris & Erdogan, 1963). In contrast, the crack growth caused by variable amplitude loading is characterized by acceleration and retardation effects (J. Harter, 2004; J. Newman, 1982), which significantly affect the RUL. Currently, there are many physics-based models (J. Harter, 2004; Yongming Liu & Mahadevan, 2007b; J. C. Newman Jr., 1992; Ray & Patankar, 2001a, 2001b) to model crack growth with acceleration and retardation effects. These models capture the fatigue crack growth phenomena reasonably well under variable loading, but they are limited to simple geometries and make predictions in a deterministic framework. Therefore, they are unable to capture the uncertainty in fatigue crack growth (Yongming Liu & Mahadevan, 2007a; Zapatero & Domínguez, 1990). Ling et al. (Ling & Mahadevan, 2012) proposed a method for the integration of structural health monitoring with fatigue damage prognosis. The prognosis methodology uses a fracture mechanics-based crack growth model, focusing on predictions under uncertainties in the

data and model errors using Wheeler's retardation model. Ling et al. (Ling, Shantz, Mahadevan, & Sankararaman, 2011) also presented a method for predicting the uncertainty in loading by investigating techniques such as rain-flow counting, Markov chain method, and autoregressive moving average (ARMA) model. Sankararaman et al. (2009) presented a prognosis methodology under variable amplitude multi-axial loading, where an equivalent stress intensity factor (SIF) as a function of the crack length and the loading condition is used. Liu et al. (2009) proposed a methodology to calculate the equivalent initial flaw size distribution based on the Kitagawa-Takahashi diagram, which is independent of the applied load and only depends on the threshold SIF. Though this method provides good results, it requires the experimentally measured threshold SIF. Hu et al. (Hu, Shen, Zhang, Meng, & Zhang, 2012) presented a method for fatigue life prediction using a damage mechanics-based approach where continuum damage mechanics principles were used to predict the corrosion fatigue crack initiation life of Al 2024-T62 alloy. This method effectively predicts the damage evolution, but it does not provide information on RUL. Grell et al. (2010) developed a probabilistic interface for the Air Force Grow (AFGROW) life prediction software, which was demonstrated on compact tension, single edge notched tension, and single lap joint specimens. This study allowed each of the parameters to be modeled as a distribution. However, as this study is based on AFGROW software, which uses analytical formulations for predicting the fatigue life, it is limited to specimens with simple geometries. Ozaltun et al. (2010) developed an energy-based fatigue life prediction framework for calculating RUL in gas turbine components. The study shows good results; however, it is limited to constant amplitude cyclic loading, and it does not consider overloads and underloads, which are

5

very common in the structural components of aircraft. Several other methods (J. A. Harter, 1999, 1999; Kermanidis & Pantelakis, 2001; J. Newman, 1981; Schijve, Skorupa, Skorupa, Machniewicz, & Gruszczynski, 2004) have been proposed for fatigue crack growth modeling. These models are mostly analytical and use a factor to account for geometry of the specimen in their formulation, resulting in limited applicability. Liu et al. (2010) and Mohanty et al. (2010) developed a purely data-driven, GP-based prognosis framework, combining on-line and off-line information, for damage state and RUL estimation of metallic and composite structural hotspots under complex loading, such as random and Fighter Aircraft Loading STAndard For Fatigue (FALSTAFF) (Chattopadhyay & Mohanty, 2011; Subhasish Mohanty, Chattopadhyay, Peralta, & Quech, 2010). Mohanty et al. (Subhashish Mohanty, Chattopadhyay, & Rajadas, 2012) also presented a passive, sensing-based strain mapping approach for real-time damage state estimation under random loading. In this method, the strains were predicted at any time using new loading information and an estimated reference model. The damage states were then evaluated by comparing the predicted and actual strains via correlation analysis. Although these models provide very accurate results, the accuracy of prediction is dependent on the available training data. In the initial stage, where there is less training data, the prediction is not accurate. However, the prediction accuracy increases over time as more training data becomes available. Wang et al. (2012) presented a generic probabilistic framework for health prognostics and uncertainty management. The generic framework is formulated using four core elements, namely the system health index, offline learning scheme, online prediction scheme, and uncertainty propagation map. Relevance vector machine (RVM), which is a sparse Bayes learning scheme, was used to

speed up the data processing as it considers only a few neighboring kernels, irrespective of the data size.

In an SHM framework, another important component is damage localization. The goal is to reliably locate and predict damage in complex structures, while accounting for the uncertainties in sensor measurements and maintaining robustness to variation in environmental parameters (such as temperature). Guided wave-based localization methods (Kim, Chattopadhyay, & Nguyen, 2011; Kishimoto, Inoue, Hamada, & Shibuya, 1995; Lu, Ye, & Su, 2006) utilize time-of-flight information for estimating the damage location, and they have gained significant popularity in recent years. In the Lamb wave localization method, feature extraction is first applied to measured sensor signals in order to obtain the time-of-flight information. Time-frequency signal processing techniques allow joint time and frequency domain analysis of signals, and the techniques have been utilized for extracting time-frequency features capturing the time-of-flight information in structures (Papandreou-Suppappola, 2002). However, a key limitation in the algorithm is the use of a fixed and generic prior over the entire probable damage region (Hensberry et al., 2013). In the case of fatigue loading where the crack length increases with the number of cycles, this fixed and generic prior leads to inaccuracies and high variance in the damage location estimates. The accuracy of the localization models is highly dependent on the uncertainties in the sensor data and environmental uncertainties, such as temperature and humidity.

In this dissertation, the uncertainties in sensor data and temperature are also considered. As the temperature increases, it affects the material properties, which in turn

affect the wave speed. Using a fixed prior under changing temperature will lead to erroneous damage location estimates. Therefore, a dynamic and more informative prior that changes as the fatigue crack grows will provide accurate damage estimates. A prognosis model capable of predicting the crack length at any given instant of time will give a very informative prior, which can be used to improve the accuracy of the localization algorithm. Since the prognosis algorithm is a key component of this framework, it should be capable of predicting damage under a variety of loading conditions that the component is expected to experience.

Aerospace components are typically subjected to multiaxial loads; therefore, an SHM framework should be capable of predicting the crack growth and RUL under these complex loading conditions. To develop reliable prognosis models, it is necessary to understand the crack propagation behavior under biaxial loading, which is different compared to uniaxial loading. The crack initiation and propagation depends on a number -of factors, such as load biaxiality ratio, phase difference, and proportionality. The crack growth under mixed-mode loading is significantly different from that of uniaxial loading where K_I (mode-I stress intensity factor) is the primary crack driving force. Erdogan and Sih (1963) proposed a hypothesis for mixed-mode fracture based on the maximum tangential stress criterion, and they postulated that the crack under mixed-mode loading extends in the direction perpendicular to the maximum tangential stress (under elastic conditions) ahead of the crack tip. Sih (1974) proposed that the crack extends in the direction of minimum strain energy density. The maximum tangential stress and minimum strain energy criteria predict similar crack propagation directions and are applicable to stable crack growth regime. Hallback and Nilsson (1994) proposed that the

cracks propagate in a direction collinear with the plane of maximum shear stress rather than propagating perpendicular to the plane of maximum tangential stress. This model is valid for unstable crack growth in microstructurally small cracks and under severe plastic deformation under torsion. It is important to note that these models were developed based on either axial-torsion loading or by applying intermediate mode-II loading on mode-I loading. A limited amount of research has been reported on the material behavior under in-plane biaxial loads (Mall & Perel, 2015). Hopper and Miller (1977) studied fatigue crack propagation in biaxially stressed notched and un-notched plates, and they found that the rate of crack propagation is affected by the biaxial stress state near the crack tip. Anderson and Garret (1980) observed that the crack growth rate is affected significantly by the change in biaxial stress field. Sunder and Ilchenko (2011) performed biaxial tests on cruciform coupons by superimposing constant amplitude loading with quasi-static load, simulating cabin pressure; they computed characteristic mode-I stress intensity factor, accounting for instantaneous biaxiality. Lee and Taylor (2011) observed that the fatigue crack growth is faster in out-of-phase loading than in-phase loading. Misak et al. (2013) investigated the behavior of 7075-T6 aluminum alloy under in-plane biaxial tension with varying biaxiality ratios and characterized the relationship between crack growth rate and energy release rate. Mall and Perel (2015) performed tension-tension fatigue tests under out-of-phase loading and observed that two cracks initiated and propagated due to the phase difference. Meischel et al. (2015) quantified the influence of very high cycle fatigue on the fatigue life of Al 7075 alloys using constant and variable amplitude loading. However, there is no reported literature on the study of fatigue behavior bridging microscale phenomena to crack propagation and fatigue life under a

9

wide range of complex biaxial loading.

In this dissertation, an effort has been made to develop a generalized SHM and prognosis framework for damage prediction in aerospace components (Al 2024-T351 and Al 7075-T651) under uniaxial and biaxial loading. For RUL prediction in Al 2024-T351 under uniaxial loading, a fully probabilistic approach combining localization and prognosis has been developed to improve both the localization and prediction accuracy (Hensberry et al., 2013; Neerukatti, Hensberry, Kovvali, & Chattopadhyay, 2015; Neerukatti, Liu, Kovvali, & Chattopadhyay, 2014). Furthermore, data from a multiscale model (Zhang, Johnston, & Chattopadhyay, 2014) has been used to predict the number of cycles for damage initiation, based on which the localization algorithm is initialized. To develop a prognosis model for RUL prediction in Al 7075-T651 under biaxial loading, comprehensive material characterization and fatigue testing was first conducted under in-plane biaxial loading to understand the crack propagation behavior. The prognosis algorithm developed for uniaxial loading was further extended to predict damage under biaxial in-phase and out-of-phase loading.

1.3   Background of Scour Prediction near Bridge Piers

Bridge scour is the removal of sediments from around a bridge pier, compromising the integrity of the structure (Warren, 2011). It has been estimated that 60% of all bridge failures result from scour (M. N. Landers, 1992), and it is the most common reason for highway bridge failure in the United States, where 46 out of 86 major bridge failures from 1961 to 1976 were a result of scour near the piers. Safety of the bridges (e.g. Custer Creek Bridge, Glanrhyd Creek Bridge, and Schoharie Creek Bridge) was compromised

due to scour caused by flash floods, which left the foundations of the piers vulnerable. Therefore, it is essential to ensure the safety of bridges and predict major scour events that may occur in the future. To forecast these events, a time-dependent scour prognosis model is essential.

Many studies (Ettema, Melville, & Barkdoll, 1998; Ettema et al., 1998; Lim & Cheng, 1998; Bruce W. Melville, 1997; Mia & Nago, 2003; Parola, Mahavadi, Brown, & Khoury, 1996) have been carried out in order to understand the mechanism of scour around bridge piers. Many parameters, such as velocity, flow depth, median particle size, pier diameter, gradation, and type of soil (cohesive or non-cohesive), influence the scour evolution, and, as a result, it is very difficult to formulate a mathematical model for scour prediction. Due to the complex nature of the scouring process, an inclusive theory for predicting the local scour around bridge piers has not been achieved (Pal, Singh, & Tiwari, 2011).

Empirical equations (Abed & Gasser, 1993; Ettema et al., 1998; Froehlich, 1989; B. W. Melville, 1992; J. Richardson & Richardson, 1994) are widely used for predicting the scour depth at bridge piers. These equations differ from each other in the factors considered for constructing the model laboratory/field conditions. The most commonly used equation is the Colorado State University equation recommended by the US Department of Transportation's Hydraulic Engineering Circular no. 18 (HEC-18) (E. Richardson & Davis, 2001). In 2001, a modified HEC-18 equation was presented, which had a correction factor (K4) for armoring by bed material size. In 2012, K4 in the HEC-18 equation was removed. Landers et al. (1996) evaluated selected empirical equations

using 139 scour measurements in live-bed and clear water conditions. Their study indicated that none of the selected equations predicted the scour depth accurately for all the measured conditions. However, the HEC-18 equation performed better compared to other equations.

Soft computing techniques, such as neural networks, are being used for civil engineering applications (Azamathulla, Deo, & Deolalikar, 2008; S. M. Bateni, Borghei, & Jeng, 2007; S. Mohyeddin Bateni, Jeng, & Melville, 2007; Firat & Gungor, 2009; Jiang & Adeli, 2004). Azamathulla et al. (2008) presented the use of alternative neural networks to predict the scour below spillways. The results indicate that neuro-fuzzy scheme provides better estimates of the scour compared to empirical equations. However, this study was limited to predicting the scour depth in ski-jump type spillways. Bateni et al. (2007) presented a neural network methodology for predicting the scour depth around bridge piers. This methodology more accurately predicts the scour depth compared to the empirical equations, but it does not provide the confidence intervals for the predictions. McIntosh (1989) showed that neural networks give better results when compared to empirical equations; however, a neural network (NN) model needs to set up different learning parameters, the number of hidden layers, and the number of nodes in a particular hidden layer (Azamathulla et al., 2008). In addition, large training sets are required to find the optimal values for the above parameters, and the NN model suffers from the problem of local minima. As the number of learning parameters increase, the objective function for optimization becomes higher dimensional, and the optimization process may yield to local minima. Support Vector Regression (SVR) has been used by researchers to predict the scour depth (Goel & Pal, 2009; Mohamed, Abdelreheem, & Abdelazim, 2009;

Pal et al., 2011). Studies indicate that SVR gives accuracy between 25% and 40% for a scour depth of approximately 2m. However, these models still do not predict the time-dependent scour.

There are only a few time-dependent scour models in the literature (S. Mohyeddin Bateni et al., 2007; Hong, Goyal, Chiew, & Chua, 2012; Mia & Nago, 2003). Mia and Nago (2003) developed a design method for predicting time-dependent scour at cylindrical bridge piers. However, this study was limited to clear water scour under laboratory conditions. Bateni et al. (2007) presented the use of Bayesian neural networks to predict the time-dependent scour in which both time-dependent and equilibrium scour depth were calculated. This study was solely done on experimental laboratory datasets. Hong et al. (2012) developed an SVR-based approach to predict the time-dependent scour under different sediment conditions and was able to capture the physics of the scouring process by considering parameters such as actual and critical Froude number. All the methods described above are deterministic regression methods that do not provide the confidence with which the predictions are made. A scour depth predicted with unknown confidence can result in failure of the bridge structures.

All these methods (Azamathulla et al., 2008, 2008; S. Mohyeddin Bateni et al., 2007; Firat & Gungor, 2009; McIntosh, 1989; Mueller & Wagner, 2005; Pal et al., 2011) formulate empirical equations and predict the scour depth for a given set of flow conditions, and they do not predict the rate at which the scour depth increases or decreases. Therefore, these methods can be used from a design point of view but not for temporal scour monitoring, as they only predict the maximum scour possible for a given

set of flow conditions. For temporal scour monitoring, measurement uncertainty plays a critical role in the predictions. In a generic prognostics framework, the measured value is considered as the true value. In the case of scour depth, there are no reliable tools to measure the scour depth accurately and continuously. Therefore, the prognostics framework should consider the measurement uncertainty to make reliable predictions of scour depth.

In this dissertation, an integrated methodology combining measurement model with prognosis model in a sequential Bayesian framework is developed to predict the temporal scour depth under both laboratory and field conditions (Neerukatti, Fard, Kim, & Chattopadhyay, 2014; Neerukatti, Kim, Yekani Fard, & Chattopadhyay, 2013). The measurement model was obtained from the preliminary radio frequency identification sensor data, and the prognosis model was developed using Gaussian process (Rasmussen & Williams, 2006). The developed methodology is very accurate, capable of accounting for large measurement uncertainties, and capable of making accurate predictions using corrupt scour data.

1.4   Objectives of the Work

The overreaching goal of the present work is to develop a comprehensive SHM framework that combines damage localization and prediction to enhance the accuracy of RUL predictions under large uncertainties. The following are the principal objectives of this work:

1.4.1 Fatigue Life Prediction in Metals

- Determine stress intensity factor as a function of crack tip location and loading for complex geometries using quasi-static finite element model under uniaxial loading

- Implement machine learning algorithms to create a mapping for the stress intensity factor as a function of the crack tip locations and loading conditions

- Develop a robust hybrid prognosis model through integrating physics based modeling with machine learning techniques

- Develop a fully probabilistic framework that iteratively integrates the hybrid prognosis with damage localization algorithm to improve localization accuracy

- Validate the developed model under constant loading, random loading, and overloads

- Characterize crack initiation and propagation behavior under in-phase and out-of-phase biaxial loading

- Determine energy release rate as a function of single and multiple crack tip locations and create a mapping using machine learning algorithms

- Develop hybrid prognosis model to predict single and multiple crack propagation under complex biaxial loads

1.4.2 Temporal Scour Prediction near Bridge Piers

- Develop a fully probabilistic Gaussian process-based prognosis model to accurately predict the temporal scour near bridge piers in both laboratory and field conditions

- Incorporate measurement uncertainty into the prognosis model by integrating it with a stochastic filtering approach using sequential Bayesian techniques

- Modify the integrated prognosis model to make predictions in the presence of corrupt scour data

1.5 Outline

This dissertation is structured as follows:

Chapter 2 introduces the development and validation of a hybrid prognosis model for crack growth and fatigue life prediction. The model is validated for complex geometries under a variety of uniaxial loading conditions. The prognosis model is then integrated with a localization algorithm using stochastic filtering. The improved localization accuracy obtained with the prognosis model as a prior to the localization algorithm, instead of using the conventional prior, is demonstrated.

Chapter 3 presents the results of characterization of fatigue crack propagation under in-plane biaxial loading. The influence of non-proportionality and phase difference on the crack growth behavior is studied. The formulations for the hybrid prognosis model to predict crack propagation under biaxial loading are presented. Finally, the algorithm is validated using the experimental fatigue test data.

Chapter 4 presents the development of a fully probabilistic adaptive integrated approach to predict temporal scour near bridge piers. The effect of measurement and prediction uncertainties and the sensitivity of the algorithm to these uncertainties are presented. Furthermore, the capability of the algorithm to make predictions under corrupt scour data is presented to demonstrate the robustness of the proposed approach over traditional scour prediction models.

Chapter 5 summarizes the research work reported in this dissertation and emphasizes the important contributions. Suggestions and recommendations on future research and directions are discussed at the end of this chapter.

2   DAMAGE PROGNOSIS UNDER UNIAXIAL LOADING

2.1   Introduction

The development of a reliable SHM and prognostics framework, which can accurately predict the fatigue life of critical metallic components subjected to a variety of in-service loading conditions, is important for many engineering applications. The two key elements of the framework discussed in this chapter are (i) localization and (ii) prognosis. Prognosis algorithms are typically used for predicting the RUL of a component, given the current state information from a localization model. However, as discussed in Chapter 1, significant uncertainties are associated with localization models especially under changing environmental conditions such as temperature (Hensberry, Kovvali, & Chattopadhyay, 2013). Therefore, it is necessary to improve the localization accuracy to improve the accuracy in RUL predictions.

In this research, a novel integrated structural damage localization method is developed for the prediction of fatigue crack growth in aluminum components subjected to uniaxial fatigue loading. A hybrid prognosis model is developed (Neerukatti, Liu, Kovvali, & Chattopadhyay, 2014), by integrating physics based model with data-driven machine learning techniques to adaptively predict the fatigue life. The goal is to improve the accuracy of prediction, by combining knowledge of the underlying mechanics of crack growth behavior and future/anticipated loading conditions. As discussed in Chapter 1, physics based models are limited by the assumptions made and are applicable to simple geometry and loading conditions. They can be computationally intensive and most modeling techniques do not account for variability in loading and/or environmental conditions. To the contrary, machine learning techniques can account for variability in

service conditions, material scatter by learning and adapting using the available data at each time step. Therefore, a hybrid model that synergistically combines both of these approaches is expected to yield accurate damage and RUL estimates. The developed prognosis model is then integrated with a fully probabilistic localization model in a sequential Bayesian framework to improve the crack location estimation accuracy. Specifically, particle filtering is used to iteratively combine the predicted crack location from prognosis model with the estimated crack location from localization algorithm to probabilistically estimate the crack location at each time instant. At each time step, the crack location predicted by the prognosis model is used as *a priori* knowledge (dynamic prior) and combined with the likelihood function of the localization algorithm for accurate crack location estimation.

This chapter is organized as follows. First, the theory for hybrid prognosis model along with the formulations of all the methodologies used is presented. The results of validation of the prognosis model under varying loading conditions and complex geometries are presented next. Finally, the integrated approach which combines the prognosis model with localization model along with the results is presented.

2.2 Hybrid Prognosis Theory

The hybrid prognosis framework presented in this chapter considers simple crack growth models, whose behaviors are inferred and updated using data-driven machine learning approaches. The combination of physics based and data-driven approaches allows for the consideration of proper damage mechanisms while correcting for material variations and uncertainty in the model parameters using data-driven model updating.

Thus, although simple physics models are used, the accuracy of the hybrid framework is far greater than those of data-driven or physics based models alone.

Linear elastic fracture mechanics (LEFM) (Paris & Erdogan, 1963) states that the crack growth rate (da/dN) is a function of the SIF range (ΔK):

$$\frac{da}{dN} = f(\Delta K), \hspace{3cm} (2.1)$$

where $\Delta K = K_{max} - K_{min}$. Most fracture theories (J. C. Newman Jr., 1992; J. C. N. Newman, 1984; Suresh, 1998) use the LEFM model with some modifications to account for variability in loading. Due to the exponential nature of crack growth, the relationship between crack growth rate and SIF is generally described using log–log transforms. The commonly observed trend showing three critical zones, stages I–III of crack growth, is shown in Figure 2.1. The prediction of crack initiation in stage I is often subject to large errors with respect to life since cracks can grow on the order of O^3 or O^4. Typically, prognosis algorithms are applied during stage II or sub-critical crack growth and are used to predict ultimate fracture.
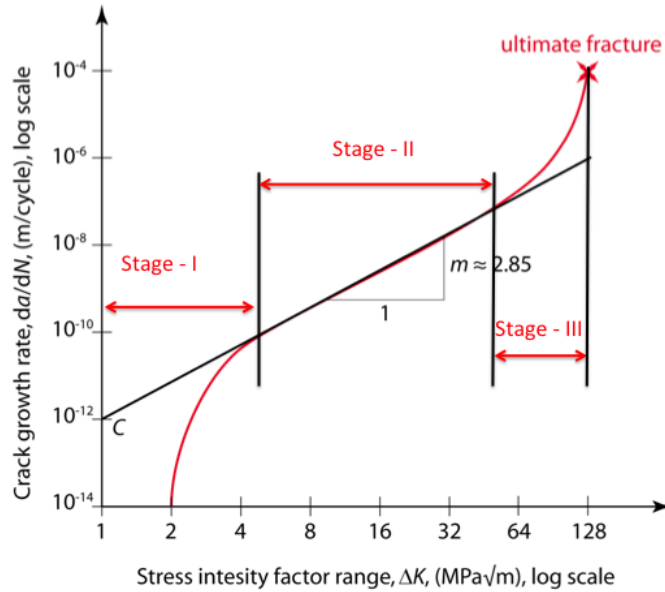
Figure 2.1 Relationship between Crack Growth Rate and SIF.

In some cases, such as constant amplitude loading, this regime is linear, and models such as Paris' Law are well suited to capture this behavior. For cases such as overloads and underloads, this regime can be highly nonlinear and discontinuous, requiring the use of advanced physics based models, which are often unavailable for complex geometries. In the hybrid prognosis framework presented here, the exact relationship between crack growth rate and SIF is inferred from the available data based on the assumption of a linear relationship with non-constant coefficients in log space. The coefficients of the linear fit are a function of historical crack growth data, future loading (i.e., overloads/underloads), material properties and cycles, and they are continuously evolving and adapting as more data become available. This is shown in Equation 2.2, where C_1 and C_2 are the adaptive coefficients, M denotes material parameter, P

represents loading, and subscripts *N-ΔN* and *N+ΔN* denote previous and future loading cycle:

$$\log \frac{da}{dN} = C_1\big(a_{N-\Delta N}, M, P_{N,N+\Delta N}, N\big)$$
$$+ C_2\big(a_{N-\Delta N}, M, P_{N,N+\Delta N}, N\big) \log(\Delta K). \tag{2.2}$$

Initial estimates for these parameters (i.e., prior to data acquisition) can be obtained through the basic material constants used in Paris' Law, which reduces the crack growth rate estimation to a classical Paris' Law extrapolation. In a typical SHM framework, damage detection, localization, and classification is based upon inputs from an embedded sensing system (Hensberry, Kovvali, Liu, Chattopadhyay, & Papandreou-Suppappola, 2012; Soni, Kim, & Chattopadhyay, 2010a). Since the SHM framework provides data on crack length and locations as well as load monitoring and cycle counting using rainflow counting algorithms (Downing & Socie, 1982), the coefficients can be updated; the nonlinear and discontinuous behavior can be modeled and captured. In order to predict the fatigue crack growth of a specimen, Equation 2.2 needs to be formulated in terms of measureable parameters and integrated until ultimate fracture. Therefore, the parameters in Equation 2.2 must be written in terms of these data, and SIF must be related to known or quantifiable parameters.

SIF can be expressed as a general function of crack length:

$$K_N = f\ (a_N, P_N, S), \tag{2.3}$$

where *S* is a geometric parameter. For simple structures, analytical expressions of SIF are available that describe its dependence on geometry, crack length, and applied load. When

22

an analytical expression is available, it can be directly substituted into Equation 2.1, and the future crack growth can then be calculated. However, in the absence of this information (e.g., for complex geometries), numerical methods must be utilized to estimate SIF. Either method is acceptable and suitable for use in the developed framework. In the current hybrid approach, a physics based formulation is used to compute SIF for a given specimen geometry under fatigue loading and a data-driven component is used for determining the model parameters C_1 and C_2.

In order to predict RUL, Equation 2.2 is numerically integrated until the crack growth rate becomes unstable. The crack length at a given cycle is written as

$$a_N = \int_0^N e^{c_1 + c_2 \log(\Delta K)} dN. \tag{2.4}$$

However, the load states can be discontinuous, and it is more appropriate to write it discretely, as follows:

$$a_N = \sum_{N=0}^N e^{c_1 + c_2 \log(\Delta K)} \Delta N, \tag{2.5}$$

To update the model with preliminary data, the integration bounds are altered, and the summation is then written as

$$a_{N+\Delta N} = a_N + \sum_{N=N+1}^{N+\Delta N} e^{c_1 + c_2 \log(\Delta K)} \Delta N. \tag{2.6}$$

However, the measured crack length will most likely be a noisy measurement with some mean (μ) and variance (σ^2) with a certain probability of detection/quantification.

Considering the uncertainty, the distribution on crack length as a function of cycles becomes

$$P(a_{N+\Delta N}) = \sum_{N}^{N+\Delta N} e^{c_1 + c_2 \log(\Delta K)} \Delta N + P(a_N), \tag{2.7}$$

where p(.) is the probability distribution.

The uncertainty in the predicted crack length is due to the error associated with the calculation of *ΔK* either analytically or numerically. Therefore, the measurement of *ΔK* will have a mean value with some variance, and this variance translates into confidence in the prediction of the crack length. Prior to integration, the non-constant coefficients C_1 and C_2 must be determined. A least squares regression algorithm is used to calculate these coefficients. The training data for the algorithm are heterogeneous in nature, originating from multiple sources. Although only *in-situ* measured data is necessary to determine C_1 and C_2, the introduction of additional data from previous experiments, expert knowledge, coefficients of Paris' Law, and advanced multiscale models can drastically improve the results. The linear relationship in Equation 2.2 is tested through cross validation on the training data. If the cross validation error is greater than 15%, a higher order relationship is used to accurately model the crack growth behavior. The developed hybrid prognosis model can be applied at the first instance of crack initiation or at any measured point in time. The framework is numerically efficient and suitable for real-time applications.

2.2.1 Calculation of SIF for a Given Specimen

The only model parameter that is necessary as an input for the developed prognosis model is SIF. Finite element analysis (FEA) can be used to calculate SIF for any specimen (with complex geometry) as a function of the crack tip location. Therefore, FEA simulations were conducted for different crack tip locations to serve as the training data. A learning model (regression) was then used to map the data, allowing for evaluation of the SIF for any given crack tip location obtained from the experiments. Two different learning techniques, least absolute shrinkage and selection operator (LASSO) (Tibshirani 1996) and relevance vector machine (RVM) (Tipping, 2001) have been investigated in this study. LASSO is a deterministic regression model whereas RVM is a fully probabilistic regression model. The difference in using these methods is described in the sections 2.2.1.1 and 2.2.1.2 . Once the SIF was obtained for any given crack length from the mapping, and the coefficients were obtained by fitting the data of the previous crack growth rate and SIF in Equation 2.2, the crack growth rate at any given cycle can be obtained. The future crack length for any given number of cycles was then computed using Equation 2.6.

2.2.1.1 Least Absolute Shrinkage and Selection Operator

Tibshirani (1996) developed the LASSO technique to improve the accuracy of regression and eliminate the outliers that contribute to errors. Here, the algorithm is explained briefly. Let the data points be (x^i, y_i), $i=1,2,...,N$, where $x^i=(x_{i1},...,x_{ip})$ are the predictor variables and y_i are the responses. The aim is to find a functional for y_i as a function of the inputs x^i using the least number of β_j:

$$y = \alpha + \sum_j \beta_j \, x_j. \tag{2.8}$$

Let α, $\beta = (\beta_1, ..., \beta_p)^T$ be the set of model parameters, then the LASSO estimate (α, β) is defined by:

$$(\hat{\alpha}, \hat{\beta}) = \arg\min \left\{ \sum_{i=1}^{N} \left(y_i - \alpha - \sum_j \beta_j \, x_{ij} \right)^2 \right\}$$
$$\text{subject to } \sum_j |\beta_j| \le t, \tag{2.9}$$

where $t \ge 0$ is the tuning parameter that controls the amount of shrinkage that is applied to the estimates. The solution to equation 2.9 is a quadratic programming problem with linear inequality constraints (Bertsekas, 1999). Let β^o_j be the full least squares estimates and let $t_0 = \Sigma |\beta^o_j|$. Values of $t < t_0$ will cause shrinkage of the solutions towards zero, and some coefficients may be exactly equal to zero. This leads to sparseness in the solution, eliminating the outliers in the process. The accuracy of the fit depends on the type of kernel function used. Kernel functions are continuous, symmetric, and generally have a positive semi-definite Gram matrix. Positive semi-definite kernels satisfy Mercer's theorem, which ensures that the kernels have no non-negative eigenvalues. A positive definite kernel means that the optimization problem is convex and thus ensures a unique solution. The choice of kernel depends on the data being modeled. A polynomial kernel can be used to model feature conjugations up to the order of the chosen polynomial, and a radial basis function kernel can be used to model circles or hyperspheres.

2.2.1.2 Relevance Vector Machine

The drawbacks of support vector machines (SVM) are that several basis functions are used and their numbers increase with the training data. In addition, the predictions are not probabilistic, and the kernel function must satisfy Mercer's condition, which requires it to be continuously symmetric. Tipping (2001) introduced a learning technique called the RVM, which is a Bayesian treatment of the SVM and does not have any of the above limitations. It is a fully probabilistic framework where the prior over the weights is governed by a set of hyper-parameters (HPs), one associated with each weight, and the most probable values are iteratively estimated from the data. The posterior distributions of many of the weights are peaked around zero, achieving sparsity. RVM is a supervised learning problem in which a set of examples of input vectors $\{x_n, n=1,...,N\}$ along with corresponding targets $\{t_n, n=1,...,N\}$ are given. The aim is to set up a model of the dependency of the targets on the inputs with the objective of making accurate predictions of the targets (t) for previously unseen values of x. Generally, predictions are based upon some function $y(x)$ defined over the input space, and "learning" is the process of inferring this function. A function $y(x)$ can be written in the following form:

$$y(x; w) = \sum_{i=1}^{M} w_i \Psi_i(x) = w^T \phi(x), \tag{2.10}$$

where the output is a linearly weighted sum of M nonlinear and fixed-basis functions:

$$\phi(x) = \left(\Psi_1(x), \Psi_2(x), \dots, \Psi_M(x)\right)^T, w = (w_1, w_2, \dots, w_M)^T. \tag{2.11}$$

The adjustable parameters (weights) $w = (w_1, w_2,..., w_M)^T$ appear linearly, and the objective is to estimate the optimal values for these parameters. Functions similar to those implemented in SVM are considered, and the function $y(x)$ is written as:

$$y(x; w) = \sum_{i=1}^{N} w_i K(x, x_i) + w_0,$$ (2.12)

where, $K(x,x_i)$ is the kernel function. In contrast to SVM, RVM uses considerably fewer number of kernel functions while offering good accuracy. The predictors are sparse and contain few non-zero w_i parameters since the majority of the parameters are set to zero during the learning process; moreover, only those that are relevant are used for optimal predictions. The process of learning the weights and making predictions is briefly described here.

Given a data set of input–target pairs $\{x_n, t_n, n=1,...,N\}$ and considering scalar-valued target functions from the standard probabilistic formulation alone, the targets are assumed to be samples from the model having additive noise:

$$t_n = y(x_n; w) + \varepsilon_n,$$ (2.13)

where the noise is assumed to be a mean-zero Gaussian with a variance σ^2. Thus,

$$p(t_n|x) = N(t_n|y(x_n), \sigma^2)$$ (2.14)

is a Gaussian distribution over t_n with a mean $y(x_n)$ and variance σ^2. Due to the assumption of the independence of t_n, the likelihood of the complete data set can be written as

$$p(t|w, \sigma^2) = (2\pi\sigma^2)^{-N/2} exp\left\{-\frac{1}{2\sigma^2}\|t - \Phi w\|^2\right\}, \tag{2.15}$$

where, $t = (t_1 \ldots t_N)^T$, $w = (w_1 \ldots w_N)^T$, and Φ is the Nx $(N+1)$ design matrix with $\Phi = [\phi(x_1), \phi(x_2), \ldots \phi(x_N)]^T$. As there is a HP associated with each training point in the data, the maximum likelihood estimation of w and σ^2 is expected to lead to overfitting. To avoid this, an additional constraint is commonly imposed in the form of a penalty term. In this approach, the parameters are constrained by imposing an explicit prior probability distribution over them. A zero-mean Gaussian prior distribution is chosen over w, as follows:

$$p(w|\alpha) = \prod_{i=0}^{N} N(w_i|0, \alpha_i^{-1}), \tag{2.16}$$

where α is a vector of $N+1$ HPs. Then, a prior is defined over α and the noise variance, σ^2. These parameters are scale parameters, and hence the prior is defined using a Gamma distribution:

$$p(\alpha) = \prod_{i=0}^{N} Gamma(a_i|a, b), p(\beta) = Gamma(\beta|c, d), \tag{2.17}$$

with $\beta = \sigma^{-2}$, and

$$Gamma(\alpha|a, b) = \Gamma(a)^{-1} b^a \alpha^{a-1} e^{-b\alpha}, \tag{2.18}$$

where $\Gamma(a) = \int_0^\infty t^{a-1} e^{-t} dt$ is the "gamma function."

The parameters α and β are set to the HP posterior mode:

$$p(t_*|t, \alpha_{MP}, \sigma_{MP}^2) = \int p(t_*|w, \sigma_{MP}^2) p(w|t, \alpha_{MP}, \sigma_{MP}^2) \, dw, \qquad (2.19)$$

where a_{MP}, S_{MP}^2 are the most probable values obtained using the type-II maximum likelihood method (Berger, 1985). Both the terms in the integrand are Gaussians, hence giving

$$p(t_*|t, \alpha_{MP}, \sigma_{MP}^2) = N(t_*|y_*, \sigma_*^2), \qquad (2.20)$$

with

$$y_* = \mu^T \phi(x_*), \sigma_*^2 = \sigma_{MP}^2 + \phi(x_*)^T \Sigma \phi(x_*), \qquad (2.21)$$

where y_* and σ_*^2 are the mean and variance of the predicted values.

2.3   Prognosis Model Validation

2.3.1   Prediction under Constant Amplitude Loading

The efficiency of the hybrid prognosis model is illustrated using a compact tension (CT) test article (Figure 2.2) with available test data. Wu and Ni (2004) conducted 30 constant amplitude fatigue tests on the CT samples to generate a statistically large dataset of the crack growth curves. CT specimens, 50 mm wide and 12 mm thick, were fabricated from 2024-T351 aluminum alloy according to the ASTM standard E647-93. The specimens were pre-cracked up to 15 mm, with crack lengths extending to 18 mm. A constant amplitude load, with a maximum amplitude of 4.5 kN and minimum amplitude of 0.9 kN, was applied during both the pre-cracking and fatigue tests. The crack lengths were measured using images taken with a microscope until the specimen fractured. The constant amplitude-loading envelope is shown in Figure 2.3.
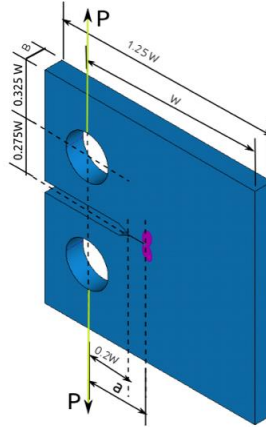
Figure 2.2 CT Specimen Subjected to Constant and Random Amplitude Loading.
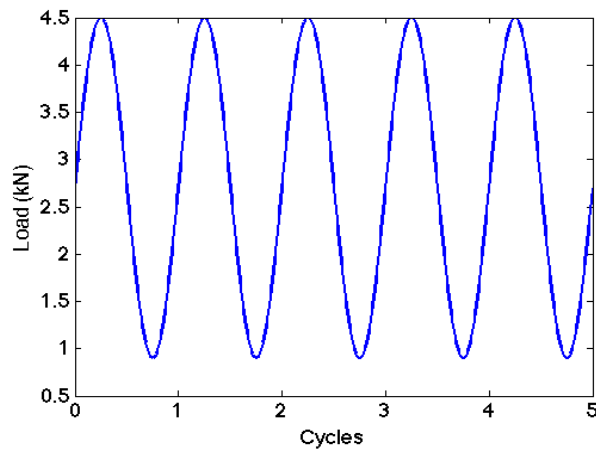
Figure 2.3 Constant Amplitude Loading Envelope.

An analytical expression for SIF as a function of the crack length (*a*), geometry, and load for a CT specimen was used to solve the differential equation shown in Equation 2.2. The analytical expression for SIF for CT specimens is shown in Equation 2.22, and the variables are defined in Figure 2.3:

31

$$K_{max} = \frac{P_{max}}{B} \sqrt{\frac{\pi}{W}} \left[16.7 \left(\frac{a}{W}\right)^{\frac{1}{2}} - 104.7 \left(\frac{a}{W}\right)^{\frac{3}{2}} + 369.9 \left(\frac{a}{W}\right)^{\frac{5}{2}} \right.$$

$$\left. - 573.8 \left(\frac{a}{W}\right)^{\frac{7}{2}} + 360.5 \left(\frac{a}{W}\right)^{\frac{9}{2}} \right]$$

(2.22)

$$K_{min} = \frac{P_{min}}{B} \sqrt{\frac{\pi}{W}} \left[16.7 \left(\frac{a}{W}\right)^{\frac{1}{2}} - 104.7 \left(\frac{a}{W}\right)^{\frac{3}{2}} + 369.9 \left(\frac{a}{W}\right)^{\frac{5}{2}} \right.$$

$$\left. - 573.8 \left(\frac{a}{W}\right)^{\frac{7}{2}} + 360.5 \left(\frac{a}{W}\right)^{\frac{9}{2}} \right],$$

where, P_{max} is the maximum amplitude and P_{min} is the minimum amplitude of the cyclic loading. To start the prediction at a given cycle, the non-constant coefficients must first be determined. This was achieved using a linear fit model for all acquired data points (i.e., all known $\frac{da}{dN}$ and $\mathrm{D}K$), with two additional training data points (from previous experiments or Paris' Law constants). In order for the data to be regressed, they must be transformed from crack length versus cycles to crack growth rate versus SIF. Numerical differentiation of Equation 2.4 was performed for this purpose. The training data points are derived from cross validation of the training data at each time step. The crack length in the final time step of the training data is calculated by initializing the additional training points to appropriate values. They were then inferred by setting the cross validation error within 15% of the actual value. As the crack length increased and more data points were available, the weight of the training data was reduced, relying primarily on the measured data. Once the coefficients were evaluated, RUL was estimated based on

the number of cycles required for the crack to reach a critical length. Considering a very small number of cycles ($\mathrm{D}N$), the crack length at $N + \mathrm{D}N$ cycles was obtained as:

$$a_{N+\Delta N} = a_N + \frac{da}{dN}\Delta N, \tag{2.23}$$

where a_N is the crack length after N cycles.
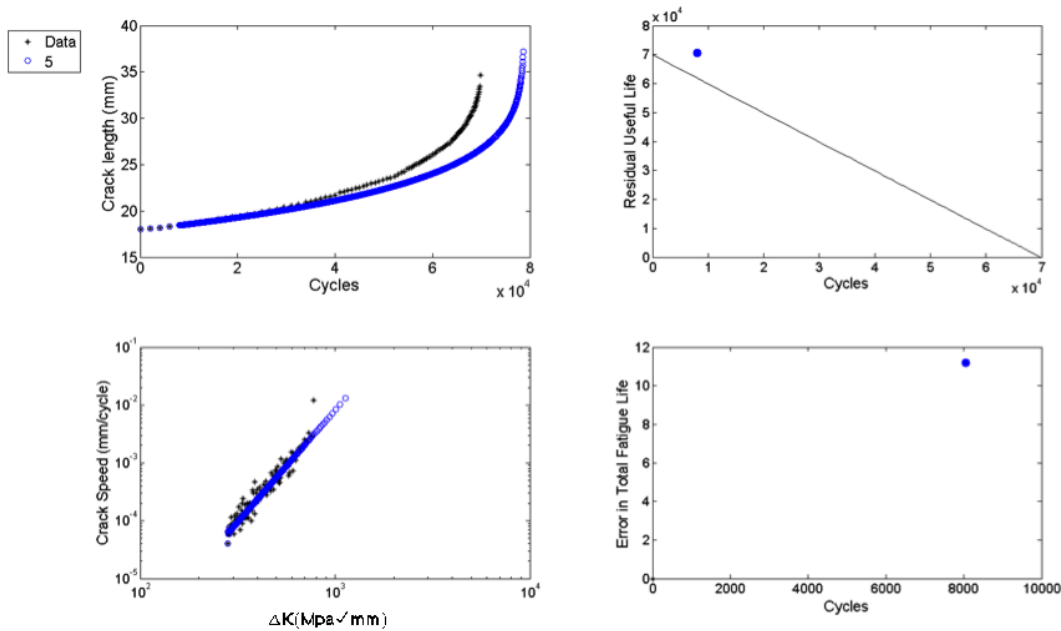
Figure 2.4 Initial Prediction Starting at 8000 Cycles.

The methodology was applied to several starting points to demonstrate the convergence of RUL as more data became available. The experimental crack length dataset and initial prediction as well as the data transformed into prediction space are shown in Figure 2.4. The first subplot shows the variation of crack length with the number of cycles. The maximum crack length before fracture was 35 mm. The second subplot shows the RUL estimation at different stages of the crack growth regime. The

33

dark line shows the actual RUL of the specimen. Estimated RUL that falls above the line indicates over-prediction of RUL while that which falls below the line indicates under-prediction. The third subplot shows the relationship between ΔK and the crack growth rate. Although this plot is nonlinear, it was assumed to be linear for every step. The hybrid model was updated iteratively as more data points were available, and the coefficients C_1 and C_2 were updated. The fourth subplot shows the error in estimation of the RUL at different stages of the crack growth regime. The error is defined as $(RUL - RUL_{predicted})/RUL$. Regression was performed on the first five data points plus the two additional points (the first and last data points corresponding to the x-axis in the third subplot). The legend on the top left corner of the figure shows the index of the data point for which the prediction is made. The cumulative results of several predictions superimposed on Figure 2.4 are shown in Figure 2.5. The results in Figure 2.5 utilize all available data to determine the non-constant coefficients of Equation 2.2. However, by reducing the amount of data used for regression, the algorithm is more suitable for adapting to small changes in crack growth rates. To illustrate this, only the last five available data points were used for regressing Equation 2.2. The predictions starting at the fifth available data point and considering only the previous five points for regression are shown in Figure 2.6.

34
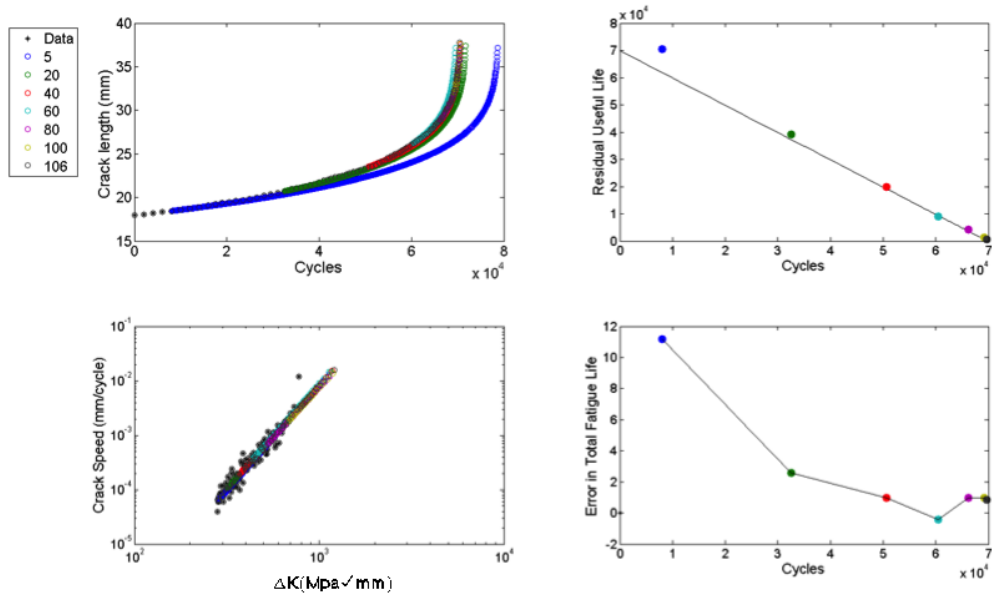
Figure 2.5 Multiple Predictions Made using the Hybrid Framework Simulating a Real-
time Experiment.
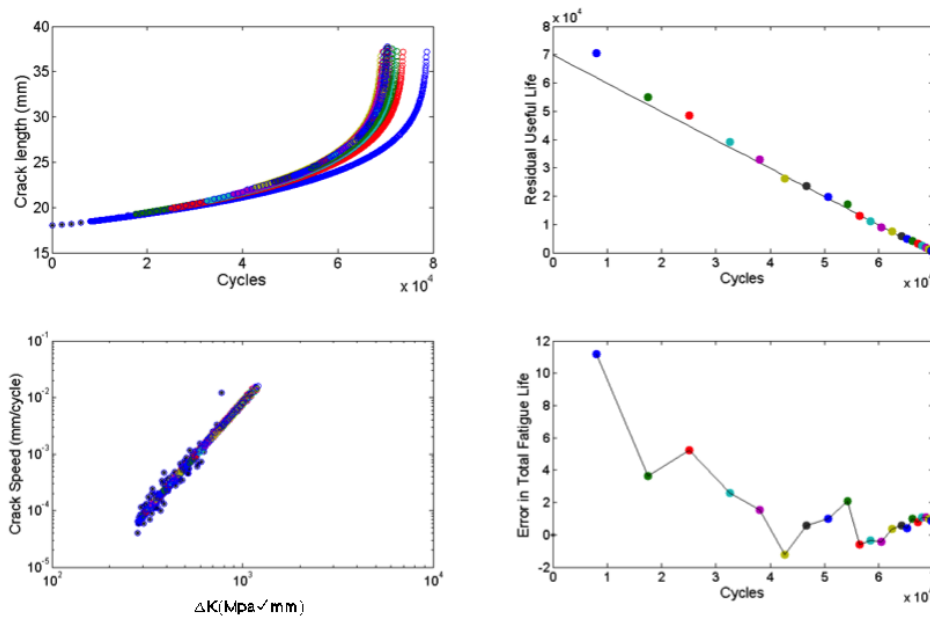
Figure 2.6 Multiple Predictions Made using the Previous Five Data Points at Every
Iteration.

The results of Figure 2.6 show the capability of the hybrid model to predict RUL with an error of less than 10% during the initial crack growth regime and 2% as more data are obtained. The variation of coefficients C_1 and C_2 with the number of cycles is shown in Figure 2.7. The coefficients start from a very low value and, as more data are obtained, they adapt to provide better estimates.
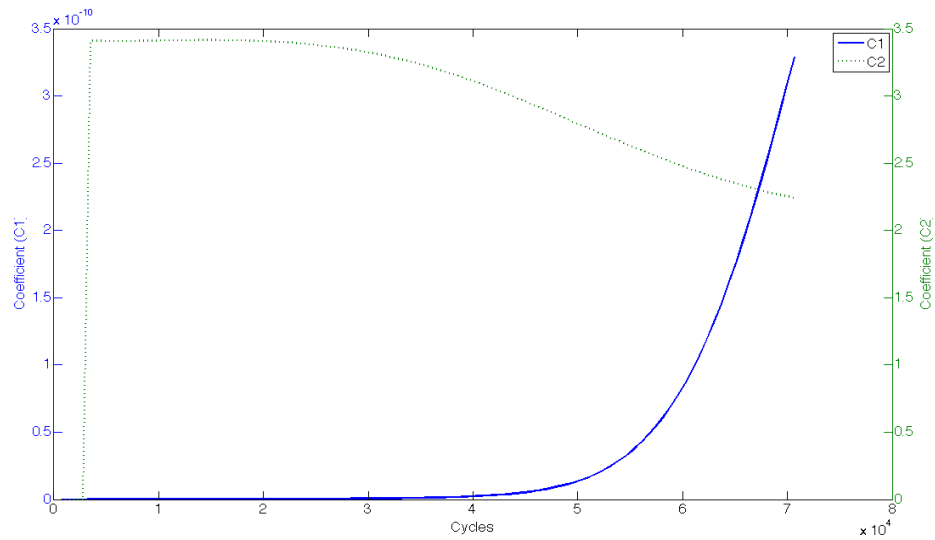
Figure 2.7 Variation of the Coefficients (C_1 & C_2) with Number of Cycles for Constant Amplitude Loading.

2.3.2 Prediction under Random Loading

Wu and Ni (2004) published a dataset for crack growth under random loading of CT specimens similar to those used in the constant amplitude loading tests. A band-limited (5–15 Hz) and uniformly distributed power spectrum density function was used to generate random signals with a mean value of 5 kN, a random amplitude with a mean of 1.118 kN, and a standard deviation of 0.552 kN. The profile of the loading envelope is

36

shown in Figure 2.8. The SIF calculation and training methodology was identical to that of the constant loading. However, the training data were modified based on the mean values of the random dataset, and the results for multiple predictions are shown in Figure 2.9. The results show the capability of the hybrid model to predict RUL under random loading conditions. As more training data become available, the model is able to predict RUL with an error of less than 5%. The variation of coefficients C_1 & C_2 is shown in Figure 2.10. The coefficients start from a very low value and adapt themselves to give accurate estimates of RUL as more data are obtained.
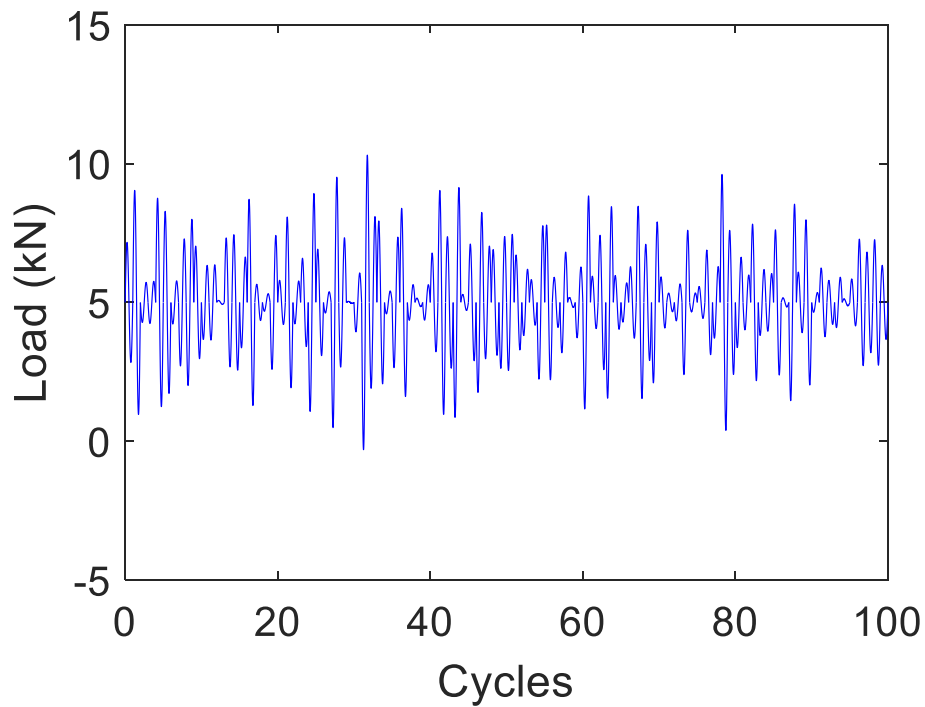
Figure 2.8 Profile of the Random Loading Envelope.
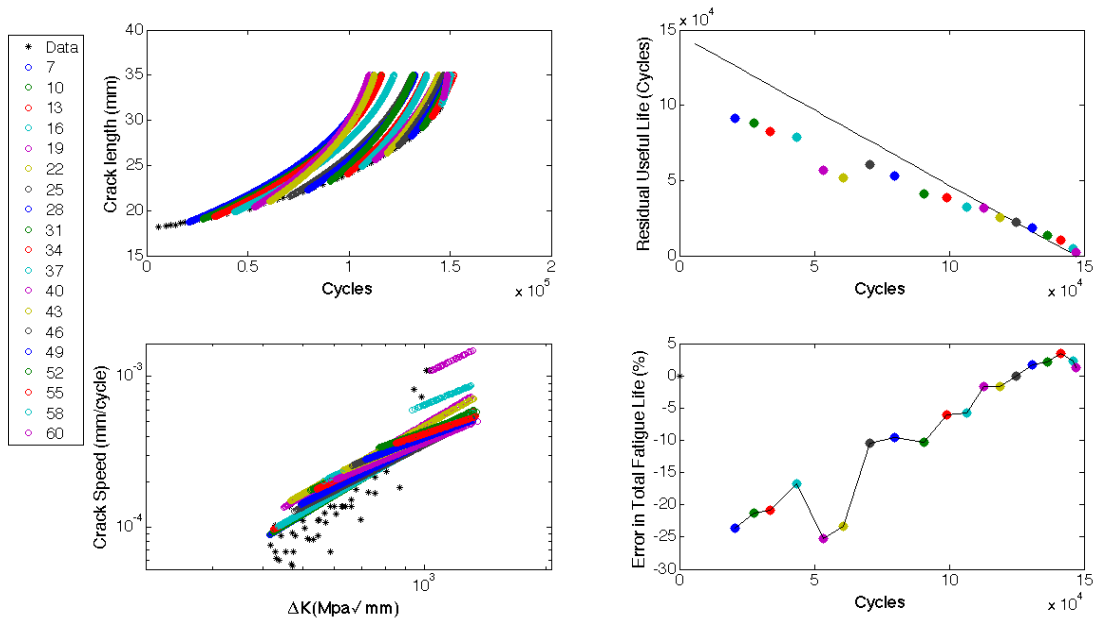
Figure 2.9 Multiple Predictions Made under Random Loading using Previous Five Data

Points at Every Iteration.
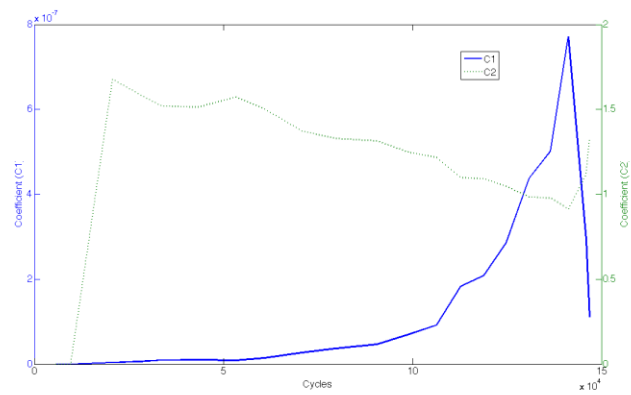
Figure 2.10 Variation of the Model Parameters (C_1 & C_2) with Number of Cycles for

Random Loading.

2.3.3   Prediction under Overloads

McMaster and Smith (2001) published a dataset for crack growth in an Al 2024-T351 center-cracked specimen under overloads. The specimen was 100 mm wide, 250 mm long, and 14 mm thick. The overload test consisted of three overload excursions applied at crack length intervals of *2a/W* = 0.4, 0.5, 0.6. A 4 mm hole was made at the center of the specimen, followed by electro-discharge machining of a starter notch 2 mm in length with a height of 0.2 mm. The geometry of the test article is shown in Figure 2.11.
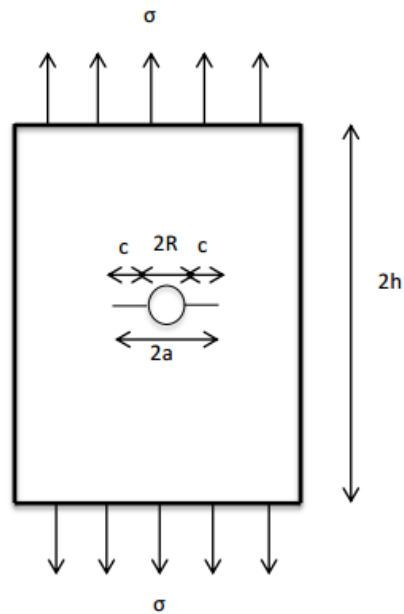
Figure 2.11 Plate with a Central Hole under Constant Amplitude Loading with Overload at Specific Intervals.

SIF for the center-cracked plate was calculated based on the formulation by Murakami (Murakami, 1987), as shown in Equation 2.24, where *a* is the crack length, *S* is the geometric factor, and *P* is the magnitude of applied loading.

$$K = SP\sqrt{\pi a}$$

$$S = \varphi * \psi$$

$$\alpha = \frac{a}{W}, \lambda = \frac{\pi}{2}\alpha, \delta = \frac{a}{R}, \gamma = \frac{R}{W}, \beta = \frac{\alpha - \gamma}{1 - \gamma}$$

$$\varphi = \frac{\pi\left[\sqrt{\frac{1}{\alpha}(tan\lambda + gsin2\lambda)}\left(1 + \frac{\varepsilon^2(2 - \varepsilon^2)}{1 - \varepsilon}\right)\right] - \sqrt{1 + 2g}}{\pi - 1}$$

$$g = 0.13(\frac{2}{\pi}arctan\delta)^2$$

$$\varepsilon = \alpha\frac{2}{\pi}arctan(0.6\sqrt[3]{\delta})$$

$$\psi = \xi(3\beta^{\frac{2P}{3}} - 2\sqrt{\xi}\beta^F)$$

$$P = \log\left(\xi^{-\frac{3}{2}}\right)/\log\beta^*$$

$$\beta^* = \frac{\gamma\delta}{\gamma(2\delta-1)+1}.$$

(2.24)

The algorithm for determining the non-constant coefficients was modified to capture the crack closure phenomenon associated with overloads. Typical overload behavior in the log–log plot of crack growth rate versus SIF is illustrated in Figure 2.12. A linear growth rate was observed in stage II; however, once the specimen has been overloaded, the crack closure phenomenon (Carlson, Kardomateas, & Bates, 1991) reduced the growth rate slope significantly. This new behavior continued until it reached the original linear response. However, since the hybrid prognosis model adapts to new data, an initial linear model was more than adequate to yield good predictions. For this sample, the training

data used to calculate the slopes of the overload region were averaged from the experimental data.
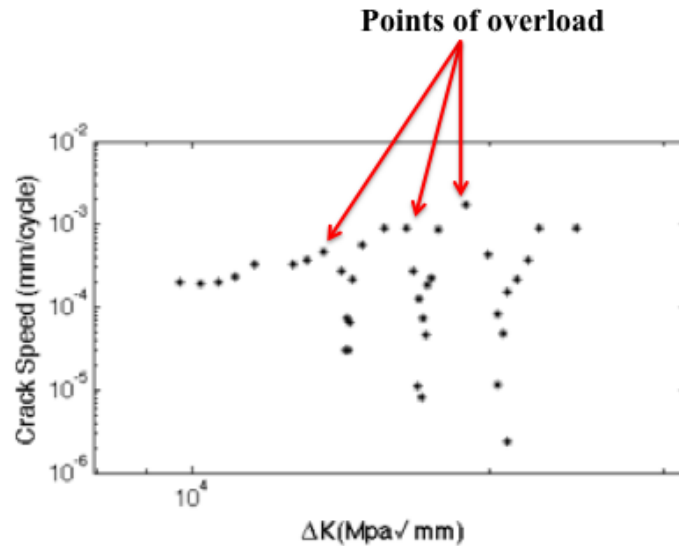
Figure 2.12 Overloads Cause Discontinuities in the Crack Growth Rate vs SIF curve due to Crack Closure.

A brief overview of the algorithm for predictions under overloads is provided for clarity. Initially, as there is no overload, the algorithm predicts the RUL with the same method used for random loading. Once there is an overload, the crack growth rate decreases significantly. In the prognosis model, after an overload, the crack growth rate is reduced to a fixed value, the exponential coefficient, C_2, is set to a high value, and estimates of these parameters are taken from training data. Once an overload is detected, the algorithm starts to fit a new line from the data point at which the overload occurs. The fitting of this new line will continue until the slope of the line obtained using the new data point matches the slope of the original fit before the overload. This procedure will be

41

repeated for different overloads to estimate RUL. In order to consider overloads in RUL, the times at which the overload excursions occur must be either assumed or modeled. To make the prediction, it is assumed that the cycles at which the experimental overloads occur are known, similar to an "oracle" approach, and the results are shown in Figure 2.13. However, if the number of overloads and the times when they occur are unknown (as is the case for most problems), the prediction results can vary and are strongly dependent on load occurrence. For example, the same specimen was simulated with three overloads at random cycles, as shown in Figure 2.14. The results show prediction capabilities within 5% for randomized future loading.
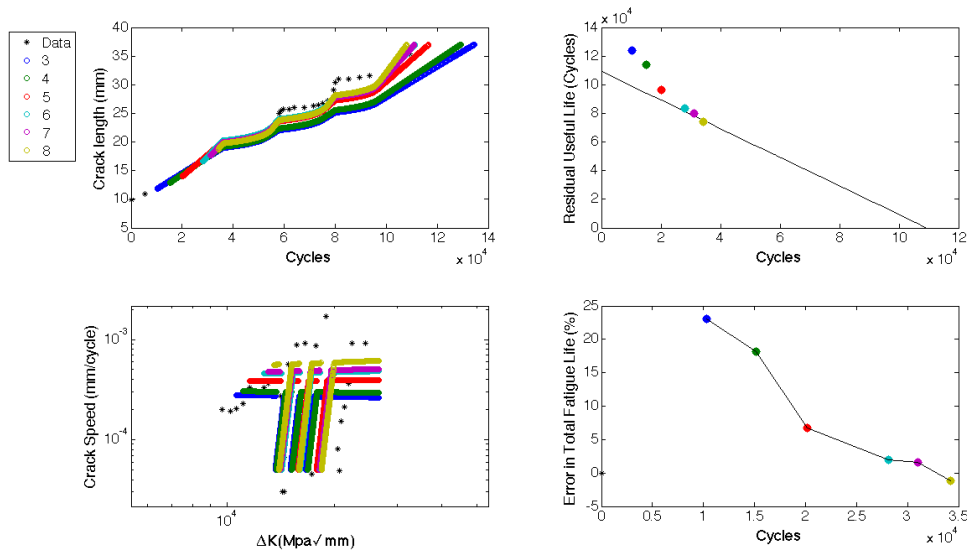
Figure 2.13 Multiple Predictions Made with Known Overload Data.
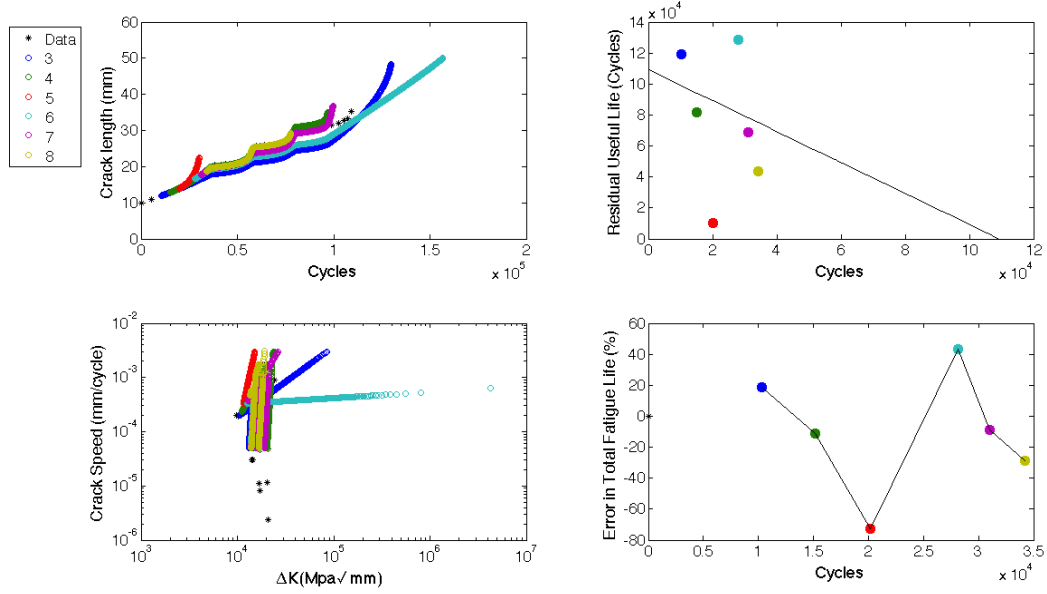
Figure 2.14 Multiple Predictions Made using Unknown Overload Data.

To demonstrate the robustness of the algorithm, the number of overloads was assumed randomly, and Figure 2.15 – Figure 2.15c show the prediction for different numbers of assumed overloads.
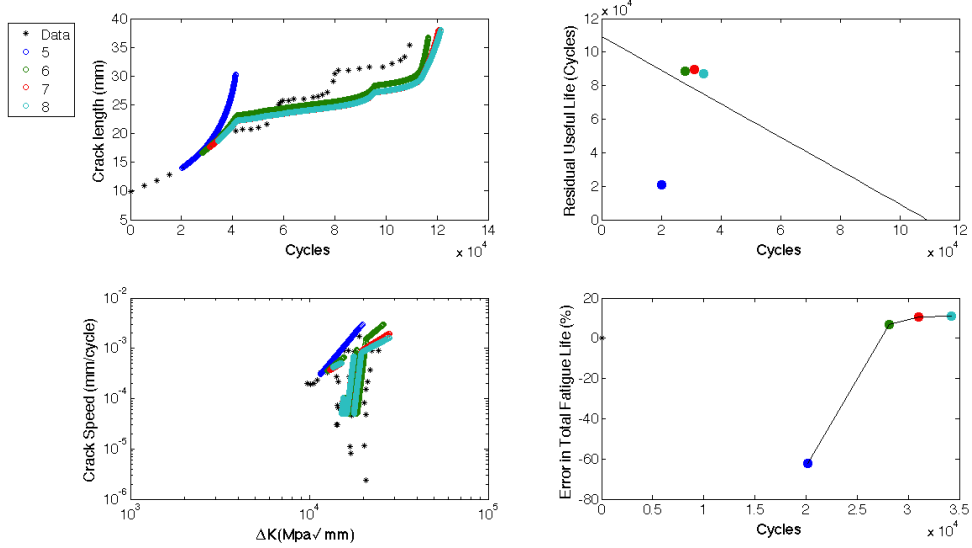
(a) Number of assumed overloads = 2
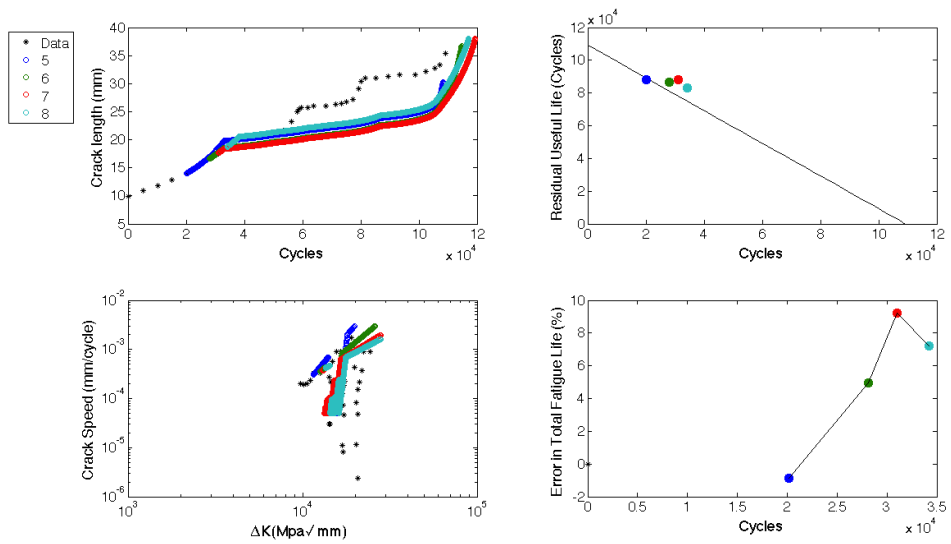
(b) Number of assumed overloads = 4
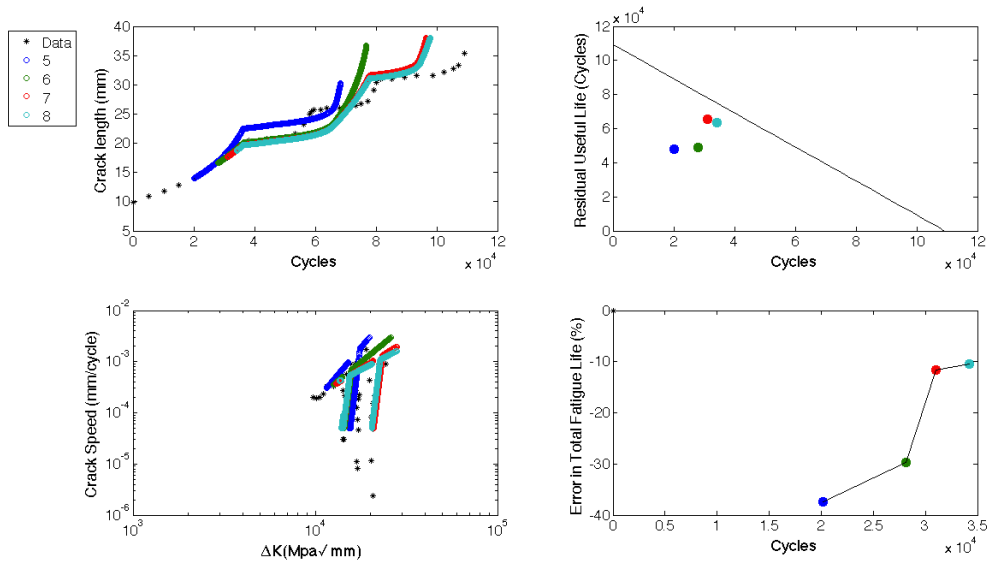
(c) Number of assumed overloads = 5

Figure 2.15 Multiple Predictions Made with Unknown Number of Assumed Overloads.

The results of Figure 2.15 show the adaptability of the algorithm to predict RUL with an error of less than $\pm 10\%$, even under an unknown number of overloads and their occurrence times.

2.3.4 Prediction for Complex Geometry

An Al2024-T351 lug joint subjected to fatigue loading was instrumented and interrogated to validate the prognosis methodology on a specimen with complex geometry. The dimensions of the lug joint are shown in Figure 2.16.
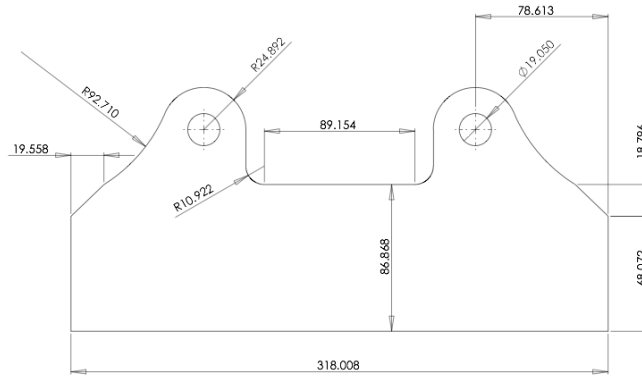
Figure 2.16 Dimensions of the Lug Joint (mm)

The lug joint was cyclically loaded with a maximum load of 13 kN and a load ratio of 0.1 at a frequency of 5 Hz. To track the crack growth, two cameras were mounted onto the frame, each focusing on the crack at the front and rear of the specimen. The captured images were used to calculate the crack length. The crack tip locations as a function of fatigue cycles are given in Table 2.1, considering the left bottom corner of the lug joint as the origin.

Table 2.1 Crack Tip Locations at Different Time Instances (Cycles).

Cycles	Crack tip location (x, y) (mm)	Crack Length (mm)
90457	(109.46, 83.8)	5.15
91585	(108.60, 79.72)	7.44
92883	(108.54, 79.64)	7.63
93057	(108.45, 77.08)	10.31
94201	(108.14, 75.28)	12.02
94384	(107.90, 73.80)	12.56
94548	(107.90, 73.59)	13.32
94716	(107.42, 71.68)	15.47

46

95014	(107.62, 70.99)	15.88
95287	(106.94, 68.68)	18.32
95387	(106.94, 67.36)	18.47
95439	(106.62, 66.20)	21.09
95663	(106.50, 63.33)	21.57

2.3.4.1   Evaluate SIF as a Function of Crack Tip Location

In order to evaluate SIF, a quasi-static finite element simulation of the three-dimensional lug joint (shown in Figure 2.17) was conducted using ABAQUS/Standard (Simulia, 2007). The crack propagation direction was modeled normal to the plane of the crack front for SIF calculation.
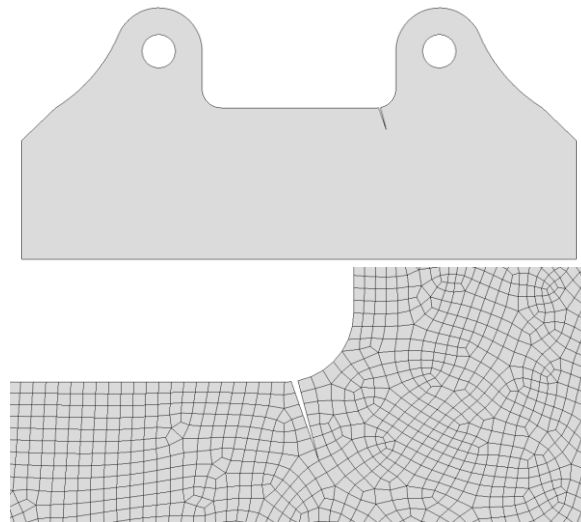
Figure 2.17 Finite Element Model of the Lug Joint with Crack.

A grid 15 mm x 25 mm was made at one shoulder of the lug joint, and the crack tip was modeled for 17 different locations on the grid. The left pinhole on the lug joint

47

was fixed in all directions, and the right pinhole was allowed to move along the direction of the loading, simulating the experimental setup. It was observed that the SIF varied linearly with loading, as shown in Table 2.2. In the current approach, SIF was first calculated for unit load. Then, for any given loading, the calculated SIF was multiplied by the load to get the new value for that particular load. The next step in the developed approach was mapping the SIF as a function of the crack tip locations. Two methods were used for this purpose: (i) LASSO, and (ii) RVM. The SIF values for different crack tip locations for a load of 13kN are listed in Table 2.3.

Table 2.2 SIF for Different Crack Tip Locations and Loads.

Crack tip (x,y) (mm)	Load (kN)	SIF (Pa√mm)
(109.00, 79.50)	13	1.08E+07
(109.00, 79.50)	1.3	1.08E+06
(104.00, 79.50)	13	1.35E+07
(104.00, 79.50)	7.5	6.75E+06
(113.16, 84.53)	13	2.58E+06
(113.16, 84.53)	3.25	6.45E+05

Table 2.3 SIF Calculated using FEM for Different Crack Tip Locations.

Crack Tip (x,y)	SIF (Pa√mm)
(109.00, 79.50)	1.08E+07
(109.00, 74.50)	1.09E+07
(108.71, 69.05)	1.39E+07
(109.00, 64.50)	1.85E+07
(109.00, 59.50)	2.45E+07
(104.00, 79.50)	1.35E+07
(104.00, 74.50)	1.47E+07
(104.00, 69.50)	1.83E+07
(104.00, 64.50)	2.06E+07
(104.00, 59.50)	2.24E+07
(99.00, 74.50)	2.16E+07
(99.00, 69.50)	1.89E+07
(99.00, 64.50)	2.05E+07
(99.00, 59.50)	2.48E+07
(109.00, 82.00)	9.60E+06
(111.50, 84.50)	2.93E+06
(113.16, 84.53)	2.58E+06

2.3.4.2 SIF Mapping using LASSO

To create the SIF mapping, the input variables were the crack tip coordinates x and y, and the output variable was SIF. There were 17 data points (i.e., 17 pairs of x and y) and one SIF value for each data point. Two different kernel functions were used to

formulate the regression model, (i) exponential and (ii) Gaussian kernel, and the results are shown below.

Exponential kernel:

The exponential kernel is a radial basis function kernel that is closely related to the Gaussian kernel, with the only difference being that there is no square of the norm:

$$k(x, y) = \exp\left(-\frac{\|x - y\|}{2\sigma^2}\right), \tag{2.25}$$

where σ^2 is the variance of the distribution. The SIF mapping and basis function weights are shown in Figure 2.18.

(a) Mapping   (b) Basis function weights
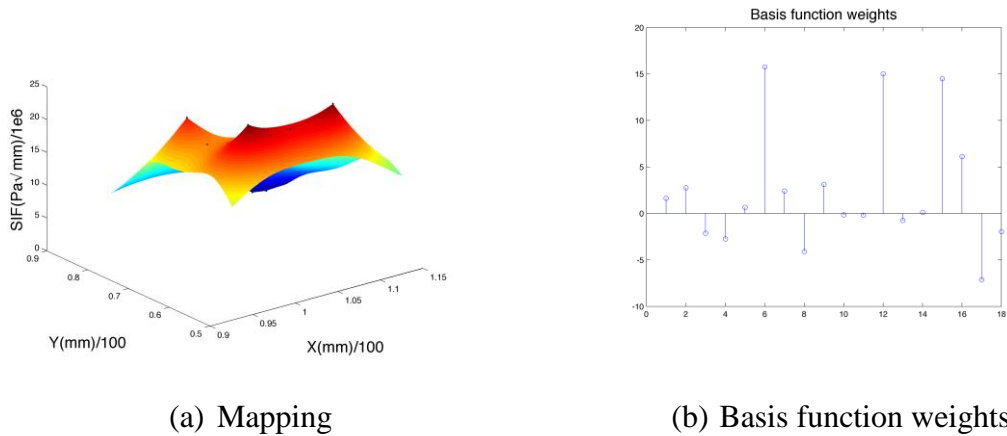
Figure 2.18 SIF Mapping using Exponential Kernel Function.

Gaussian kernel:

The Gaussian kernel is also an example of the radial basis function kernel given as:

$$k(x, y) = \exp\left(-\frac{\|x-y\|^2}{2\sigma^2}\right), \tag{2.26}$$

where σ^2 is the variance of the Gaussian distribution. The SIF mapping and basis function weights are shown in Figure 2.19. Most of the basis function weights were set to zero due to the additional constraints imposed during the optimization procedure.

(a) Mapping   (b) Basis function weights
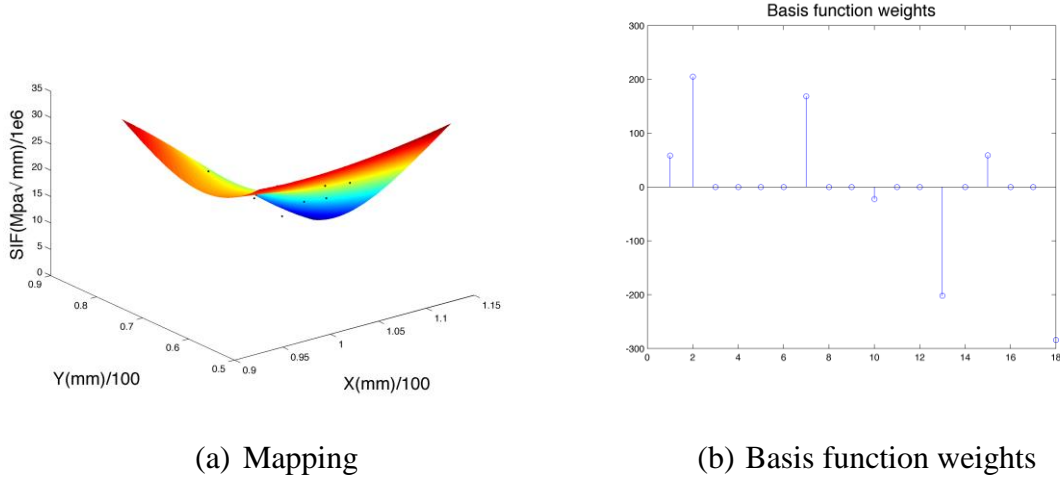
Figure 2.19 SIF mapping using Gaussian kernel function

Combination of Gaussian and exponential kernels:

Using a single kernel may not yield good results, regardless of the degree to which the parameters of the kernels are optimized. In such cases, a linear combination of the kernels can be used. The results of the mapping (Figure 2.20) show that using a combination of kernels produces a very good fit for the data:

$$k(x,y) = \exp(-\frac{\|x-y\|^2}{2S^2}) + \exp(-\frac{\|x-y\|}{2S^2}) \tag{2.27}$$
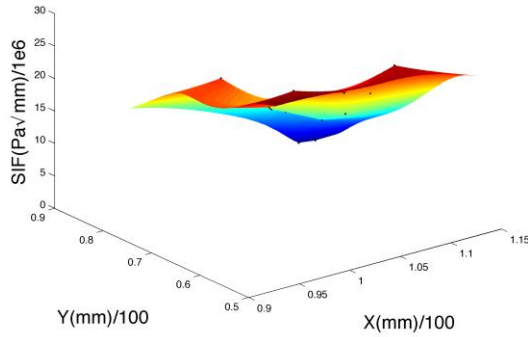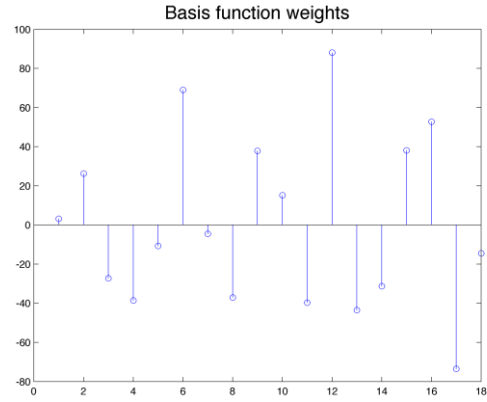
(a) Mapping   (b) Basis function weights

Figure 2.20 SIF Mapping using a Combination of Gaussian and Exponential Kernel Functions.

2.3.4.3   SIF Mapping using RVM

SIF mapping using RVM was created utilizing Equations 2.20 and 2.21. The input parameters were the crack tip coordinates (x, y), and the output parameter was the SIF for a given crack tip location. While the LASSO is a useful tool for robust regression, it yields a point estimate for the regressed model. RVM is a powerful technique that enables full probabilistic regression, and it has the additional advantage of providing a measure of uncertainty (confidence intervals) to the regressed estimate. Thus, using RVM for the SIF mapping allows a probability distribution on SIF as a function of the x and y position to be obtained. In this setting, the uncertainty in SIF was transferred naturally to uncertainty in crack growth rate for subsequent use in the prognosis model.

The inputs that were used for the mapping included 17 data points, and the predictions were plotted on a grid of 201 by 301 points, for a total of 60501 data points. For each of the 60501 grid points, a lower bound and an upper bound (2σ) were established, based on the variance of the prediction. The input data was mapped with

52

RVM using a Gaussian kernel, and the obtained fit with lower and upper bounds is shown in Figure 2.21. The vertical lines on the surface show the 95% confidence bounds of the predicted SIF. For this set of input and output data, the Gaussian kernel provided good results based on cross validation; hence, this kernel was used for the mapping.

(a) Mapping   (b) Enlarged view of the mapping
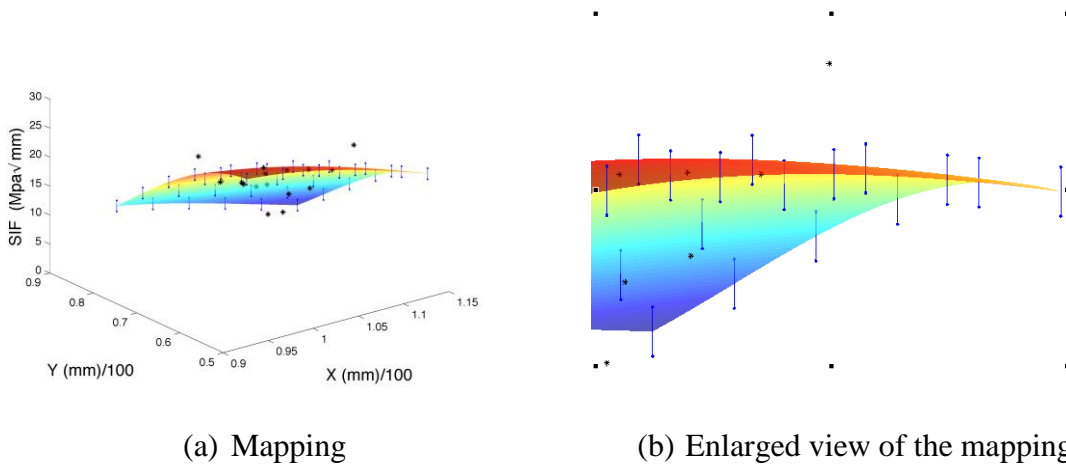
Figure 2.21 SIF Mapping Using RVM.

2.3.4.4   Prediction using Hybrid Prognosis

The future crack length at any given cycle was first predicted using deterministic regression by mapping the SIF versus crack growth rate (Equation 2.1) utilizing the surface fitting toolbox in MATLAB (MathWorks, 2012). Then, as the experiment continued and the crack tip location was identified, the SIF was determined for the obtained crack tip location from the mapping. Next, Equation 2.2 was used to evaluate the crack growth rate at any given instant, and Equation 2.5 was used to predict the future crack length at any given number of cycles. Figure 2.22 shows the results of the prediction of crack length in this deterministic framework. The crack length at 93000 cycles was not calculated properly due to a problem with the camera image. Nonetheless,

the prognosis model was able to predict the crack length with an error of less than 7% for almost the entire crack growth regime.

(a) Crack length prediction   (b) Error in prediction
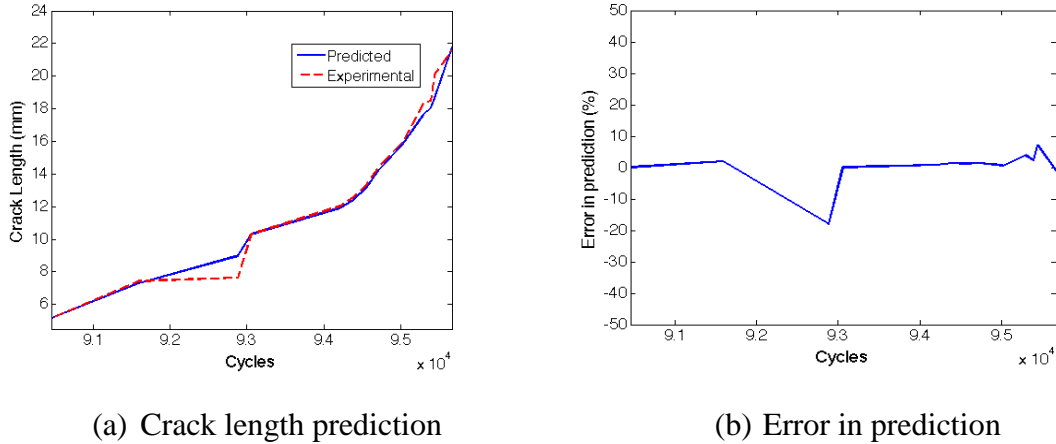
Figure 2.22 Deterministic crack length prediction using hybrid prognosis

The prediction of the crack length was then made in a probabilistic framework, which offers the capability of confidence intervals. However, uncertainty in the prediction of the crack length arises from uncertainty in the prediction of SIF. When SIF was evaluated using RVM, the variance in prediction was obtained when evaluating the mean value at the test point. This variance translates into the confidence in the prediction of the crack length. Figure 23 shows the prediction with confidence intervals. The experimental crack length in Figure 2.23 is very close to the lower bound of the 95% confidence interval, which highlights the capability of the algorithm to slightly over-predict the crack length as a fail-safe prediction.
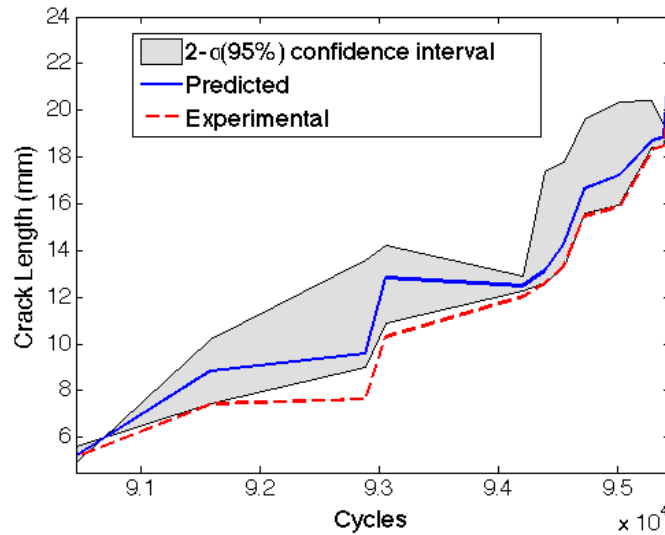
Figure 2.23 Probabilistic Crack Length Prediction using Hybrid Prognosis.

2.3.4.5   Comparison with Paris' Law

In order to validate the developed hybrid prognosis model, the results were compared with those obtained using Paris' Law. The SIF obtained from the mapping using RVM was utilized to calculate the crack growth rate using Paris' Law. As the material used was Al2024-T351, the Paris' coefficients C and m were 3.3e-10 and 2.3 respectively. Using these coefficients and the SIF obtained using RVM, the crack growth rate was calculated at any given cycle. Once the crack growth rate was obtained at a given cycle (N), the future crack length at cycle ($N+\Delta N$) was calculated using Equation 2.23.
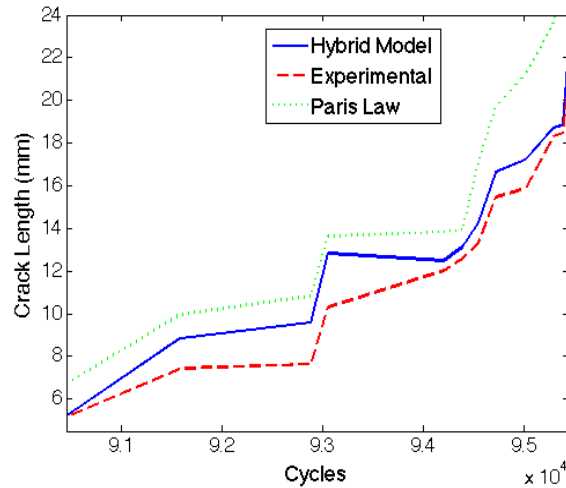
Figure 2.24 Comparison between the Hybrid Prognosis Model and Paris' Law.

Figure 2.24 shows a comparison of the predicted crack lengths using the hybrid model and Paris' law. Using Paris' law, the crack length was highly over-predicted, as shown in Figure 2.24, whereas the hybrid model only over-predicted crack length within the 95% confidence interval (Figure 2.23), which is the best possible scenario for any practical application.

2.4 Robust Damage Localization using the Hybrid Prognosis Model

In a typical SHM framework, damage localization and prognosis are performed independently, with localization occurring first. Localization algorithms (Hensberry et al., 2013) typically search the entire probable damage region (prior), which leads to large errors and uncertainties in the localization results. To overcome this issue, a novel integrated was developed for effective damage localization. The developed method uses sequential Bayesian techniques to combine a physics based damage prognosis model with a data-driven probabilistic damage localization approach. Particle filtering (PF) (Doucet,

Freitas, & Gordon, 2001) is used to iteratively update crack length predictions obtained using the prognosis model with the estimated crack location from a Lamb wave-based probabilistic crack localization algorithm (Hensberry et al., 2013). The prognosis model uses information from physics based modeling to accurately predict the crack propagation and combines this with a data-driven approach to account for the variability in loading conditions and material scatter. The localization algorithm uses a probabilistic framework to account for uncertainty in the time-of-flight measurements. Robustness to multipath effects and unknown temperature variations is achieved using multi-sensor time-of-flight information in conjunction with data association (Bar-Shalom, 1987; Bar-Shalom, Daum, & Huang, 2009), and the technique has been shown to be capable of localizing fatigue damage in complex structures at unknown temperatures (Hensberry et al., 2013). However, a key limitation of the algorithm is the use of a fixed and generic prior over the entire probable damage region. In the case of fatigue loading where the crack length increases with the number of cycles, this fixed and generic prior leads to inaccuracies and high variance in the damage location estimates. Therefore, in this work, a dynamic and more informative prior obtained from the physics based prognosis model is incorporated into the localization framework for dynamic damage estimation and prediction. Use of this dynamic prior will significantly increase the overall effectiveness of the algorithm since the domain of probable damage locations is smaller than when a fixed prior is used. Even though there is a small computational overhead in constantly adapting the prior, i.e., using the prognosis model at every time step, the overall efficiency remains high since the prognosis model is very efficient. Thus, the sequential Bayesian framework utilized here optimally combines the predicted and estimated crack

tip locations dynamically with uncertainty quantification. The developed method was validated experimentally on an aluminum 2024-T351 lug joint subjected to uniaxial fatigue loading. The growing crack length was measured at different time instances using high-resolution images, and the corresponding Lamb wave measurements were recorded. The crack location estimates obtained with and without the dynamic prior were then compared in order to demonstrate the benefits of integrating the damage prognosis model and localization algorithm using particle filtering.

2.4.1 Damage Localization Algorithm

In conventional time-of-flight-based damage localization schemes, a known fixed wave speed is used, based on the assumption that it is representative of the true wave speed in the structure. In reality, however, structural components are often interrogated at unknown and varying temperatures, and the wave speed is thus both unknown and can change with the temperature. Further, even a small change in the wave speed can result in significantly different time-of-flight and damage localization results. When attempting to localize damage at unknown temperatures, the largest factor contributing to error is uncertainty in the speed of the wave that is interrogating the damage (Raghavan & Cesnik, 2008). In order to achieve a damage localization capability that is robust to unknown temperature variation effects, the temperature estimation and velocity compensation algorithm presented by Hensberry et al. (2013) was utilized.

A complete description of the damage localization algorithm can be found in Hensberry (2013); a brief description is presented here. In this approach, time-of-flight information is first extracted from Lamb wave sensor measurements using the grouped

matching pursuit decomposition (MPD) algorithm with a Gaussian time-frequency (Papandreou-Suppappola, 2002) dictionary. The probabilistic damage localization algorithm uses a Bayesian framework to optimally combine information from prior knowledge about the damage location with information from (noisy) time-of-flight measurements obtained from wave-based sensor data. The grouped MPD of a received sensor signal contains several wave components with respective time-of-flights. However, it is not known which of these correspond to the A_0 wave reflected from the damage and which to boundary reflections and other paths unrelated to the damage. Since the localization algorithm specifically requires time-of-flight information for the damage-reflected waves, this uncertainty must be quantified and addressed. Thus, probabilistic data association is utilized to account for this measurement origin uncertainty within the estimation framework. The time-of-flight estimates from all the sensor paths are then collected and fused to estimate the damage location.

2.4.2 Integrating Localization with Prognosis

The integrated structural damage localization and prognostic method optimally combines the Lamb wave measurement-based localization method with the physics based adaptive prognosis model in a sequential Bayesian framework. Particle filter is used to adaptively track the position of the growing crack by combining the likelihood function obtained from the probabilistic localization method with the predicted prior distribution from the prognosis model. The predicted crack distribution obtained from the prognosis model is a specification for the crack length a (Equation 2.23) and needs to be converted to crack position $\overline{X} = (x, y)$. In the present study, the increment in crack length has been

used to predict the crack tip location as follows. The increment in crack length at a given number of cycles is

$$\Delta a_N = a_{N+\Delta N} - a_N = \sum_{N=N+1}^{N+\Delta N} e^{c_1 + c_2 \log(\Delta K)} \Delta N. \tag{2.28}$$

The predicted crack tip location at ($N+\Delta N$) cycles is then given by

$$\bar{X}_{N+\Delta N} = \bar{X}_N + \Delta a_N * (\sin\theta, \cos\theta), \tag{2.29}$$

where θ denotes the angle of propagation of the crack, determined at each time step by averaging the previous crack directions. Further, the standard deviation of the predicted crack length ($\bar{\sigma} = (\sigma_x, \sigma_y)$) is

$$\bar{\sigma}_{N+\Delta N} = \sigma_{N+\Delta N} * (\sin\theta, \cos\theta), \tag{2.30}$$

where, $\bar{\sigma}_{N+\Delta N}$ is the standard deviation in the predicted crack length at ($N+\Delta N$) cycles. Together, Equations 2.23 and 2.28–2.30 define the Markovian state dynamics model used for tracking the crack tip location with the particle filter:

$$\bar{X}_{N+\Delta N} | \bar{X}_N \sim p(\bar{X}_{N+\Delta N} | \bar{X}_N). \tag{2.31}$$

The measurement model relating the time-of-flight extracted from sensor data to the crack location is given by

$$\tau_{N+\Delta N} | \bar{X}_{N+\Delta N} \sim p(\tau_{N+\Delta N} | \bar{X}_{N+\Delta N}). \tag{2.32}$$

Given the probabilistic damage evolution and measurement models and the time-of-flight extracted from the measured sensor data, the crack location can be optimally

estimated in a sequential Bayesian framework using stochastic filtering. For the non-linear and non-Gaussian state-space model employed here, the sequential Monte Carlo technique of PF is suitable. Particle filter estimates the posterior distribution of the state variables in a sequential Bayesian framework by representing the distributions using particles and weights. Further, PF is used to integrate information from the damage prognosis (state dynamics) model and the damage localization (measurement) model with time-of-flight sensor data to adaptively estimate the crack tip location. The sequential Bayesian framework for iteratively computing the posterior distribution on the crack location $p(\bar{X}_N|\tau_N)$ can be written as

$$p(\bar{X}_N|\tau_{1:N}) \propto p(\tau_N|\bar{X}_N) \int p(\bar{X}_N|\bar{X}_{N-1}) \, p(\bar{X}_{1:N-1}|\tau_{N-1}) \, d\bar{X}_{N-1}, \tag{2.33}$$

where N denotes fatigue cycles. The PF representation of the posterior probability distribution is an approximation using particles and associated weights $w_n^{(k)}$, given by

$$p(\bar{X}_N|\tau_N) \approx \sum_{k=1}^{\Omega} W_N^{(K)} \delta \left(\bar{X}_N - \bar{X}_N^{(k)} \right), \tag{2.34}$$

where Ω is the number of particles and $\delta(.)$ is the Dirac delta function. The PF iteratively updates the particles and weights via sequential importance sampling (Gordon, Salmond, & Smith, 1993). Following the SIS procedure at each time step (fatigue cycles), particles are sampled from the state distribution $p(\bar{X}_{N+\Delta N}|\bar{X}_N)$, and the weights are updated using the measurement likelihood $p(\tau_N|\bar{X}_{N+\Delta N})$. Resampling is then performed as needed to avoid degeneracy. The crack location estimate $\widehat{(x,y)}_N$, given t_N, is then computed as the expected value of the estimated posterior as

61

$$\hat{\bar{X}}_N = E[(\bar{X}_N | \tau_N)] \approx \sum_{k-1}^{\Omega} W_N^{(K)} \bar{X}_N^{(k)}. \qquad (2.35)$$

Using multiscale modeling (Zhang, Johnston, & Chattopadhyay, 2014), the crack initiation location and cycles required for the crack to reach a length of 1 mm can be predicted with high accuracy. Based on this information, the algorithm is initialized using a Gaussian distribution for the crack location with a mean of (208.5, 84.5) and a standard deviation of 1 mm.

In summary, the crack length at any given cycle is predicted using Equation 2.23. It is then converted to crack tip location using Equations 2.29–2.30. The posterior over the predicted crack tip location is obtained using Equation 2.31. The crack tip location is estimated using this posterior as a prior to the localization algorithm. Therefore, at any given cycle, the predicted and estimated crack tip locations are available. These values are combined using the PF, and the crack tip locations are updated using Equation 2.35.

2.4.3   Results of the Integrated Approach

To study the performance of the developed integrated structural damage localization and prognostic method, a bulk aluminum 2024-T351 lug joint was instrumented and subjected to fatigue loading and interrogated. The dimensions of the lug joint are shown in Figure 2.25.
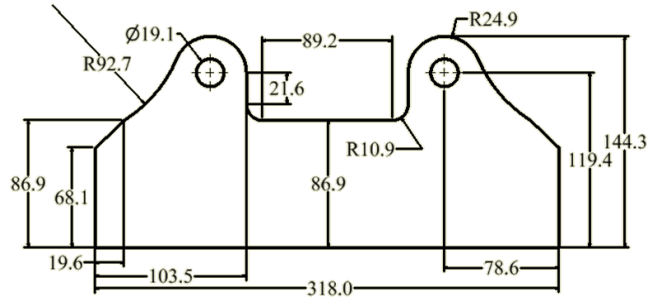
Figure 2.25 Dimensions of the Aluminum 2024-T351 Lug Joint (mm).

Circular lead zirconium titanate transducers (PZTs) 6.33 mm in diameter with a thickness of 0.25 mm (American Piezo Ltd.) were installed on the specimen for collecting Lamb wave data. The PZT sensors were bonded to the specimen using an off-the-shelf cyanoacrylate adhesive. Seven PZTs were instrumented on the lug joint, with a symmetric configuration about the lug joint's plane of symmetry. The locations of the PZTs can be seen in Figure 2.26. The aluminum lug joint, which was machined from a bulk Al 2024-T351 plate, was cyclically loaded between 1.3 kN and 13 kN (load ratio of 0.1) at a rate of 5 Hz. To track the crack growth, a camera with a macro lens was mounted in front of the specimen and focused on one of two hot spots (top and bottom shoulders). Another camera was placed behind the fatigue frame and focused on both hot spots, and images were captured along with the sensor data. The images were then used to compute the crack length through digital measurements using calibrated images. The fatigue experiment setup is shown in Figure 2.27.
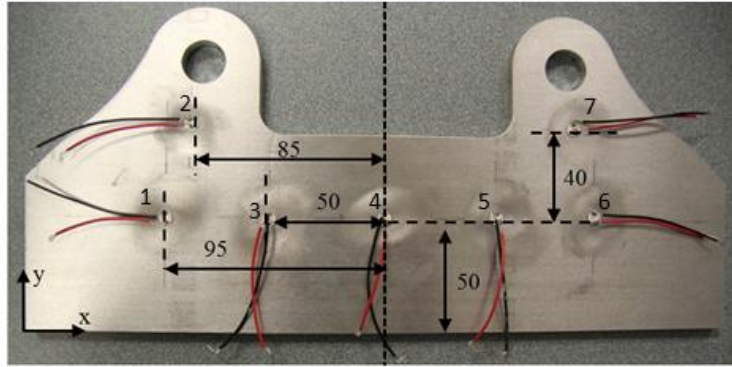
Figure 2.26 Instrumented Aluminum Lug Joint with PZT Sensors (Dimensions in mm).
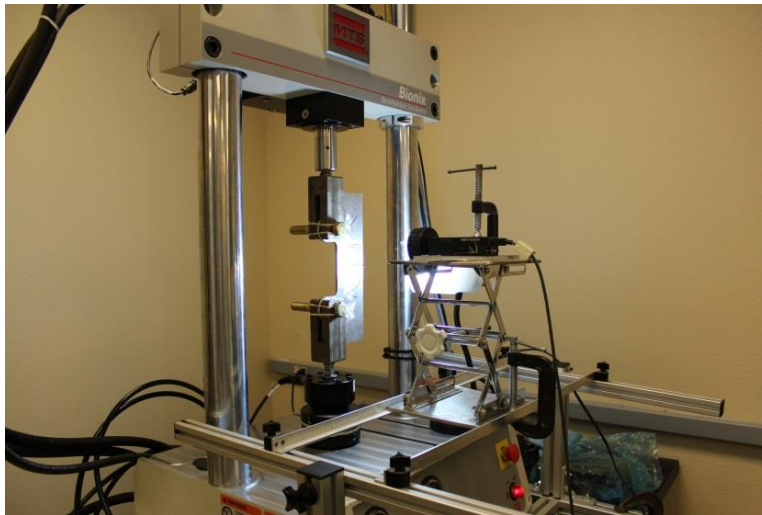
Figure 2.27 Fatigue of Lug Joint; Experimental Setup

The fatigue crack length was measured at different time instances (fatigue cycles), and corresponding Lamb wave data were collected using the PZT sensors. A National Instruments data acquisition system (model NI PXI 1042) with a 14-bit Arbitrary Waveform Generator (AWG, model NI PXI-5412) and a 12-bit high-speed digitizer (DIG, model NI PXI-5105) was utilized to interrogate the specimen. The actuation signal was a windowed cosine with a 250 kHz central frequency for temperature estimation and

a 500 kHz central frequency for damage localization. A round-robin approach was used to collect data from all sensor paths. The response along each sensor path was measured ten times and averaged in order to increase the signal-to-noise ratio.

In order to test the robustness of the damage localization algorithm to temperature variations, Lamb wave data were collected from the lug joint over a range of temperatures using a Cascade-Tek forced air lab oven. Specifically, at 13 different stages of fatigue load, the lug joint was removed from the fatigue frame, placed in the oven, and interrogated using the PZTs at temperatures of 20 °C, 40 °C, 60 °C, and 80 °C. Temperatures higher than 80 °C were not investigated due to the limited operating temperature range of the bonding adhesive and the PZT wiring. After each round of sensor data collection, the lug joint was cooled to room temperature and reinstalled on the fatigue frame, and the test was continued. The data from the lug joint fatigue experiment were used to validate the damage localization and prognosis algorithms. First, the prognosis model was applied for prediction of the crack length in the lug joint. The prediction results over the entire crack growth regime are shown in Figure 2.28. It can be seen that the crack length was predicted with very high accuracy (error $\leq$ 1 mm), and prediction errors decreased towards the end of the crack growth regime as more data was used. The confidence intervals in Figure 2.28 show that the algorithm was able to predict the crack length with 95% confidence over the entire crack growth regime. Note that the experimental crack length curve remains the same for all the temperatures (20 °C, 40 °C, 60 °C and 80 °C) because the fatigue test was performed at room temperature (the sample was removed from the fatigue frame, heated in an oven only when collecting PZT signals

at different temperatures, and cooled to room temperature before continuing the fatigue test). Therefore, thermal effects were not considered in the prognosis model.
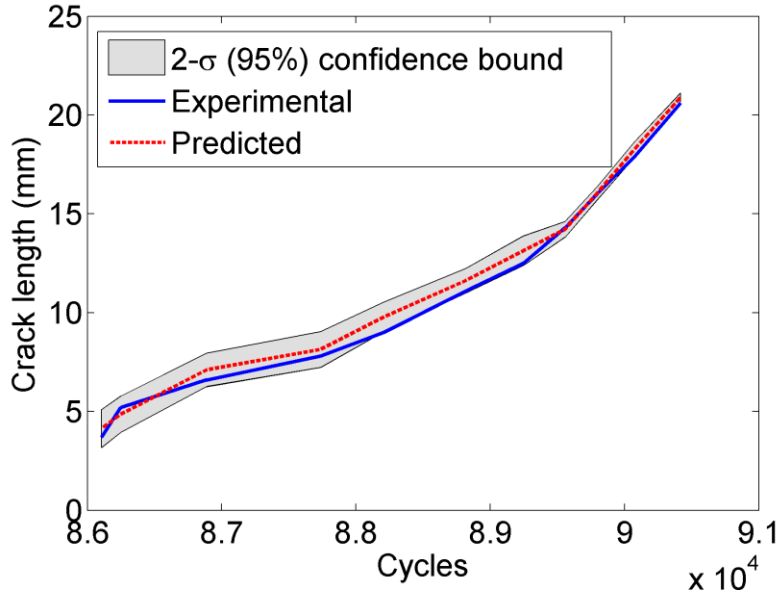
Figure 2.28 Prediction of Fatigue Crack Length in the Lug Joint Specimen using the Hybrid Prognosis Model.

Next, the damage localization method was applied to predict the crack length in the lug joint. The time-of-flight and corrected velocity for each sensor path were used to calculate a temperature estimate, and the estimates from all the sensor paths were averaged to obtain the overall estimated temperature. This process was applied to the experimental lug joint data that were available for the temperatures of 20 °C, 40 °C, 60 °C, and 80 °C. Figure 2.29 shows the results of the temperature estimation.
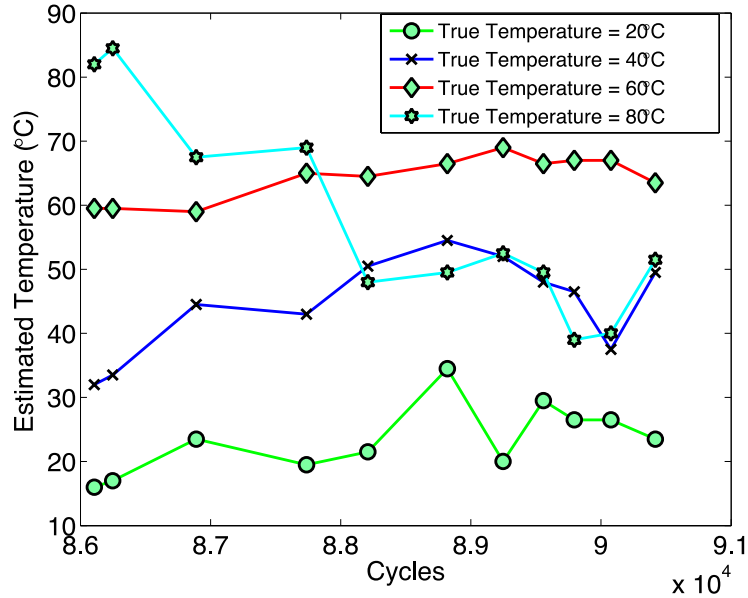
Figure 2.29 Temperature Estimation in the Lug Joint.

It can be seen that the temperature estimation method is very accurate in the 20 °C, 40 °C, and 60 °C cases, with a mean deviation of roughly 5 °C. The inaccuracy of the temperature estimates for the 80 °C case can be attributed to the use of PZTs beyond their rated temperature operation range of 70 °C. The prior crack location probability distribution used in the probabilistic localization algorithm was next defined using a fixed prior that covers the entire expected area of crack tip locations. From finite element simulations and previous work on lug joints (Soni, Kim, & Chattopadhyay, 2010b), it has been shown that under specified loading conditions, the hot spots for fatigue crack growth are the shoulders of the lug joint. Therefore, a truncated multivariate Gaussian prior probability was applied to the lug joint near the shoulder where the crack originated, with a mean location of (211, 80) mm (see Figure 2.25) and covariance parameters of 15 mm, 15 mm, 0 mm, and 0 mm, respectively. A brief discussion of the performance using the localization method with the fixed prior is given here. Figure 2.30 shows the

experimental and estimated crack tip locations on the lug joint at a temperature of 20 °C for 86106 and 90417 fatigue cycles, respectively. The marker "X" shows the experimental crack tip location while the "diamond marker" shows the estimated crack tip location.

(a) Experimental and estimated crack tip at 86106 fatigue cycles

(b) Experimental and estimated crack tip locations at 90417 fatigue cycles
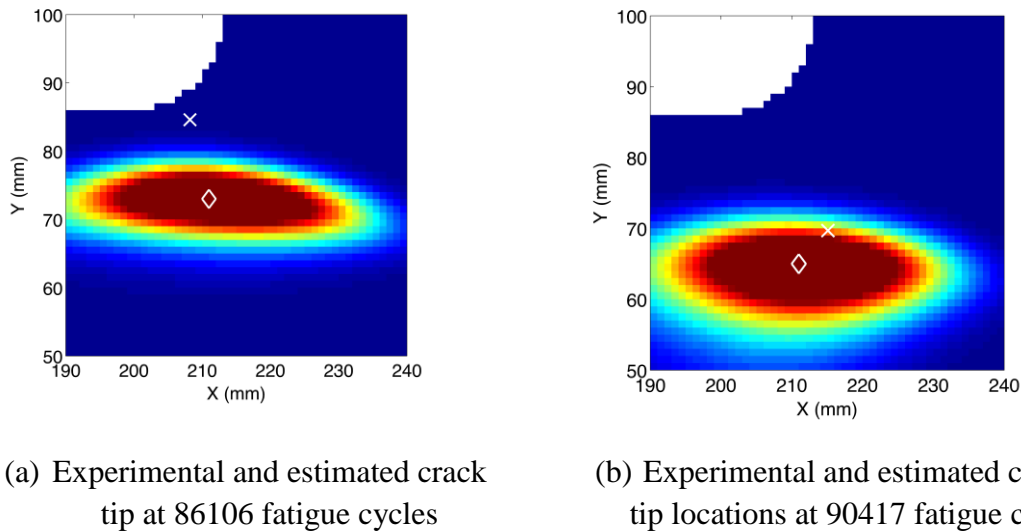
Figure 2.30 Crack Location Estimation Performance at 20 °C using the Probabilistic Localization Method with a Fixed Prior.

For the four temperatures and 13 crack lengths tested, the average crack tip localization error was found to be approximately 9 mm. The significant error and uncertainty in the localization is due to the assumed general fixed prior distribution that covers the entire crack growth area. With an adaptive and more focused prior, both the bias and variance would decrease significantly, resulting in a more useful and robust damage localization system. Finally, the integrated damage localization algorithm was applied to estimate the crack tip location in the lug joint specimen. The prognosis model was used to compute a physics based prior that is adaptively combined with the likelihood function of the data-driven localization algorithm, using the particle filter for accurate crack location

estimation. The number of particles in the particle filter was set to 1000, which was found to be sufficient to obtain accurate estimates of the posterior crack length distribution. Figures 31a–31d show the experimental and estimated crack tip locations at 20 °C for four different fatigue loading stages.
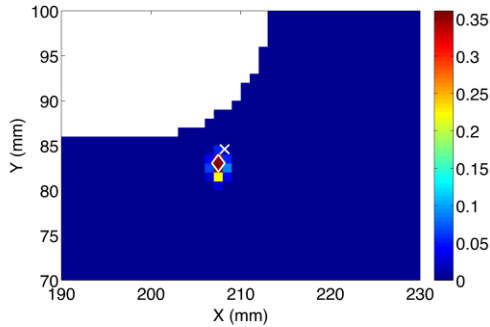
(a) Experimental and estimated crack tip location at 86106 cycles (20 °C)
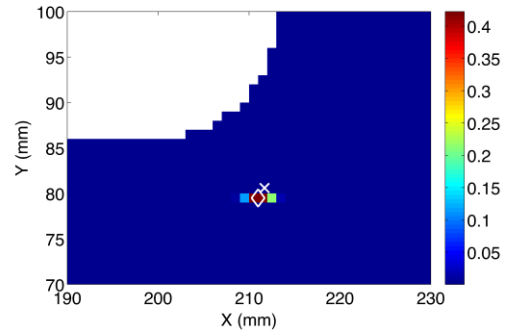
(b) Experimental and estimated crack tip location at 88208 cycles (20 °C)
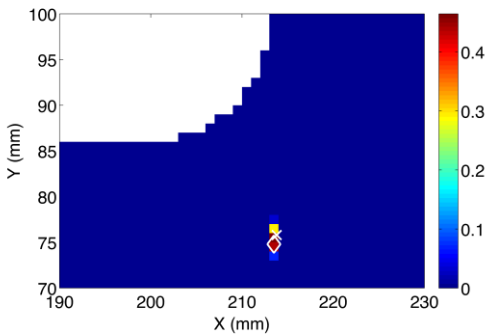
(c) Experimental and estimated crack tip location at 89557 cycles (20 °C)
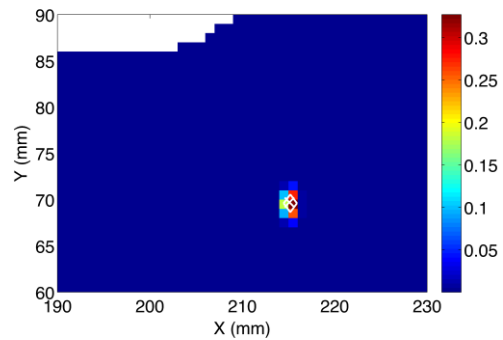
(d) Experimental and estimated crack tip location at 90417 cycles (20 °C)

Figure 2.31 Crack Location Estimation at 20 °C using the Integrated Damage Localization Approach.

Comparisons of Figure 2.30a with Figure 2.31a and Figure 2.30b with Figure 2.31d show a significant increase in the prediction accuracy (and decrease in uncertainty)

with use of the dynamic prior. The crack tip locations were estimated using the integrated method for all the temperatures (20 °C, 40 °C, 60 °C, and 80 °C). The results show that the crack tip location was predicted with high accuracy and low uncertainty, even at a temperature of 80 °C. The results of crack tip location prediction at 20 °C, 40 °C, 60 °C, and 80 °C are shown in Figure 2.32.
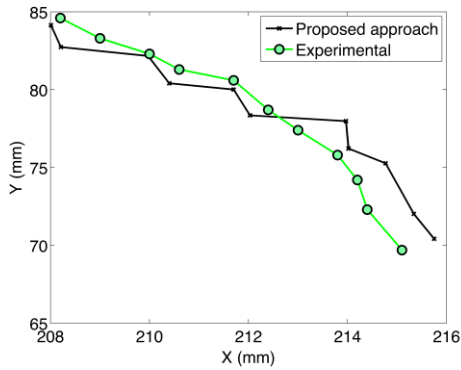
(a) Crack tip locations at 20 °C
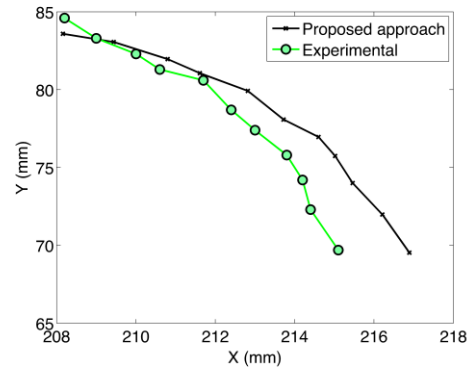
(b) Crack tip locations at 40 °C
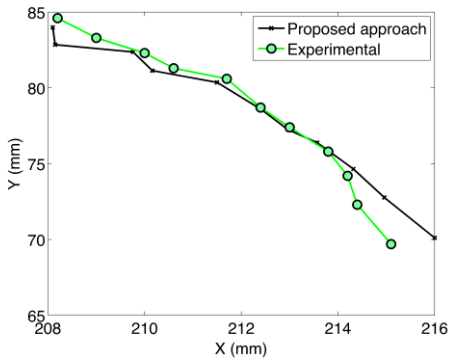
(c) Crack tip locations at 60 °C
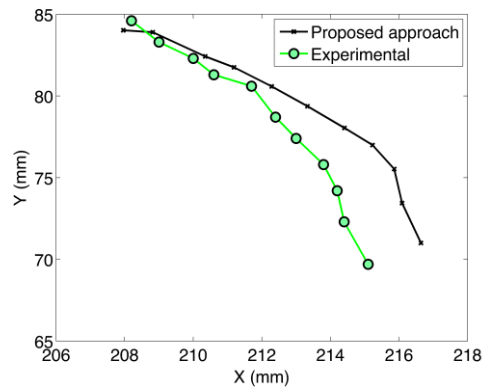
(d) Crack tip locations at 80 °C

Figure 2.32 Crack Location Estimation using the Integrated Damage Localization Approach.
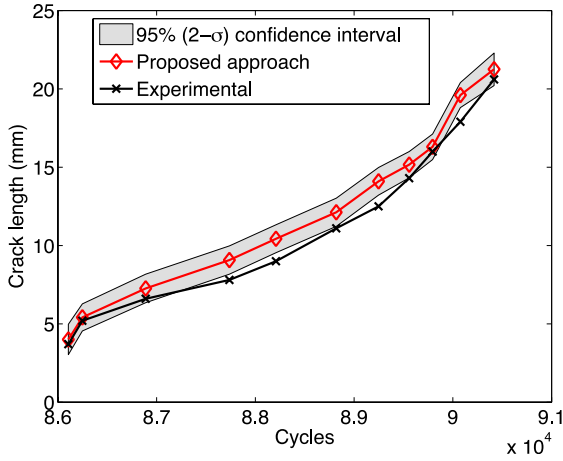
(a) Crack length estimation at 20 °C
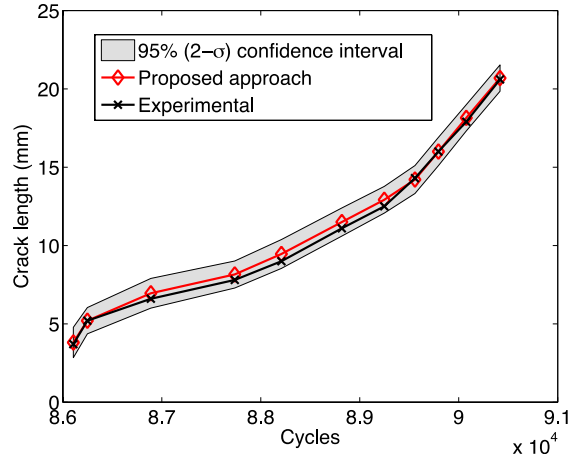
(b) Crack length estimation at 40 °C
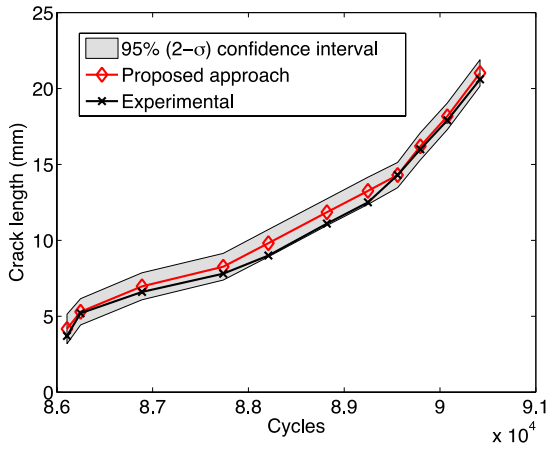
(c) Crack length estimation at 60 °C
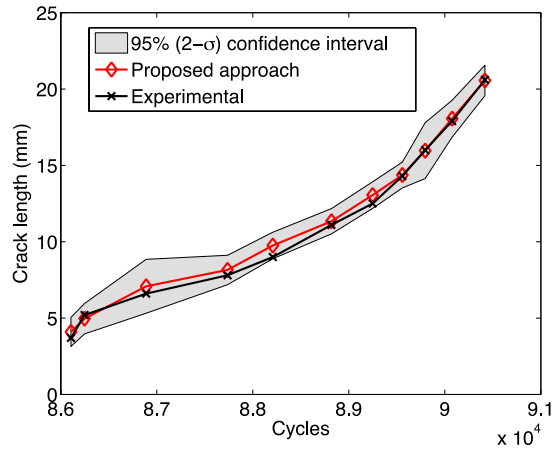
(d) Crack length estimation at 80 °C

Figure 2.33 Crack Length Estimation using the Integrated Damage Localization
Approach.

Figure 2.33 shows the estimation of crack length using the integrated approach. It can be seen that the integrated algorithm is able to predict crack tip locations more accurately (to within 1 mm of the experimentally observed values) than the probabilistic localization algorithm alone. Using the developed algorithm, the search domain for the crack tip location is significantly smaller, and hence the framework is more computationally efficient. The tradeoff for this method is the computational time required

71

for using the prognosis model as a prior knowledge. Since the prognosis model uses the results from FE simulations, the parameters of which are stored in the form of a dictionary, it is very computationally efficient. Overall, the total computational time is significantly reduced using the integrated approach. All the simulations have been run on a 2.3-GHz Intel Core i5 Processor. The computational time for the prognosis model was 2.31 s. For the first run of the localization algorithm without prior knowledge, the computational time was 4519 s, and using dynamic prior, the computational time was 925 s. Figure 2.34a and Figure 2.34b show the absolute and relative error in crack location prediction for different temperatures at various crack lengths, respectively. Absolute error is measured as the error in estimation of crack length, whereas relative error is measured as the error in estimated crack length compared to the actual crack length. The maximum error in predicting crack length occurred at a temperature of 20 °C as opposed to 80 °C, which is not intuitive. This is due to the fact that the estimated crack length followed a zigzag pattern (see Figure 2.32a). As the error is calculated using the crack length, and since the crack length at 20 °C is larger due to the zigzag pattern, the error shown in Figure 2.34 is larger at 20 °C. The zigzag pattern can be attributed to the PF scheme, where the particles are generated randomly with values higher or lower than the crack length. The data were first collected for all the temperatures, and the analysis was then run for each temperature separately. Figure 2.32 and Figure 2.33 show that, though the crack length estimation error was large for 20 °C, the estimated crack tip locations were much closer to the actual crack tip locations. The results for 40 °C, 60 °C, and 80 °C show that the average absolute and relative errors in predicting crack length are less than 1 mm and 8%, respectively.

72
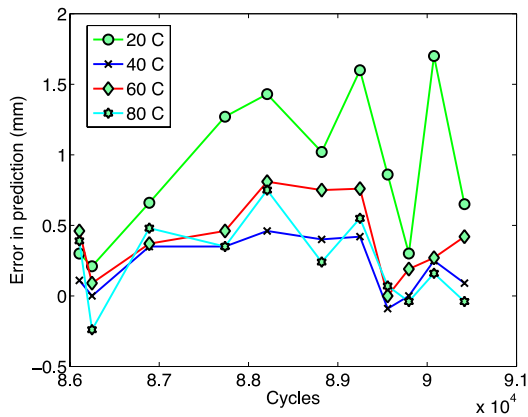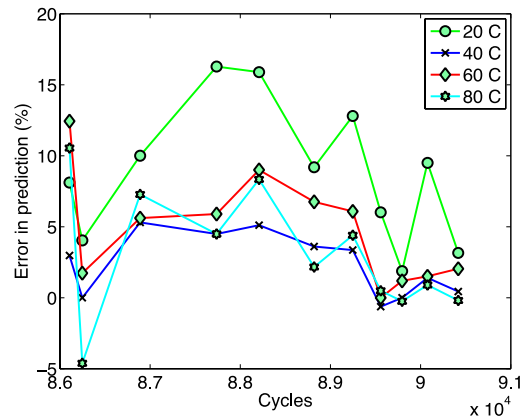
(a) Absolute error   (b) Relative error

Figure 2.34 Error in the Estimated Crack Length at Different Temperatures.

Figure 2.35 compares the predictions of crack length using different methods (i.e., prognosis, localization, and integrated approach). The results show that, although the error in crack length estimation using the localization algorithm is large, the integrated approach combines the error with the predicted value (prognosis) and estimates a crack length closer to the experimental crack length. While there is a large uncertainty associated with the localization algorithm, when combined with the dynamic prior, the uncertainty in prediction is reduced, as shown in Figure 2.33.
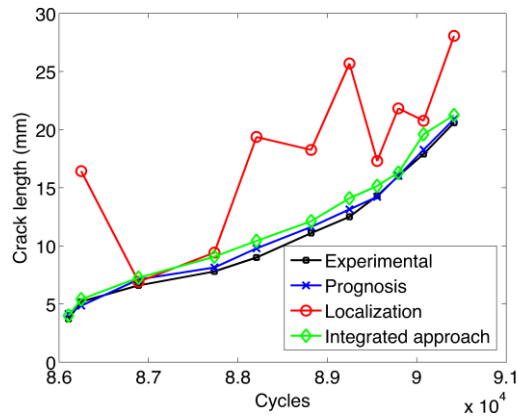
(a) Crack lengths at 20 °C   (b) Crack lengths at 40 °C
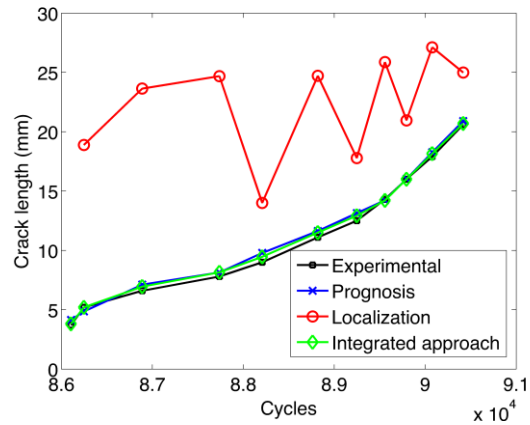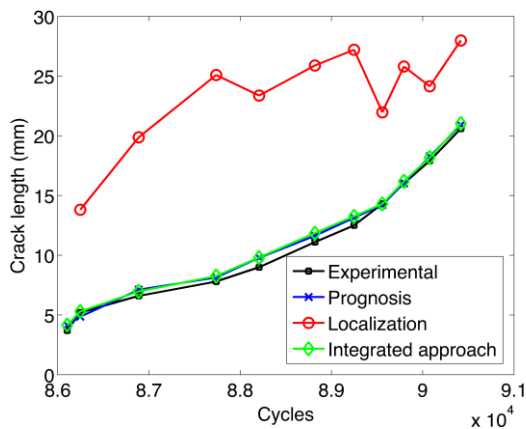
(c) Crack lengths at 60 °C   (d) Crack lengths at 80 °C
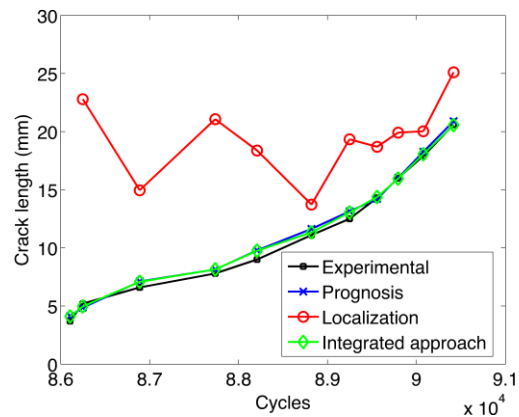
Figure 2.35 Comparison of Crack Length Prediction using Prognosis, Localization, and Integrated Approach.

2.5   Summary

In this chapter, a hybrid prognosis methodology has been developed that integrates a simple physics based approach with experimental data. The algorithm provides high fidelity predictions of RUL for CT specimens subject to various loading conditions. Linear fit models were initially used to extrapolate and predict the crack

growth behavior. The RUL was predicted within ± 5 % of the actual RUL for constant amplitude loading. The methodology was applied to random loading conditions; the mean of the random data set (load) was used as the initial training data. The RUL prediction was within ± 5% for the random loading case, reducing to ± 2% as the amount of training data increased. The algorithm was then modified to incorporate the crack closure phenomenon observed during overload. An error of ± 5% was observed if the assumed point of overload was known. However, even when the overload points were unknown, the algorithm was still able to predict within 5% error given enough training data for overload behavior. The algorithm was then validated with the experimental data from the fatigue test conducted on an Al 2024-T351 lug joint. The algorithm was able to predict the crack length at any given instant with an error of less than 7% for most of the crack growth regime. The developed methodology was compared with Paris' Law and found to yield much more accurate results.

The prognosis model was also used to improve the accuracy of damage localization. A novel integrated framework has been developed for effective damage localization and prognosis in metallic structures with complex geometries. The method combines the hybrid prognosis model with a data-driven damage localization approach to estimate crack growth robustly under unknown temperatures. The Lamb wave measurement-based localization algorithm requires appropriate prior knowledge of the probable damage location for reliable estimation performance. Rather than using a generic and fixed prior, the developed method incorporates a dynamic prior obtained from the highly accurate prognosis model. Using PF, the predicted crack locations from the prognostic model were iteratively combined with the estimated crack locations from

the localization algorithm to obtain improved estimates. Online temperature estimation was performed to achieve robust localization performance. The developed methodology was validated on an Al2024-T351 lug joint subjected to fatigue loading. PZT sensor data were collected at temperatures of 20 °C, 40 °C, 60 °C, and 80 °C. Results from application of the algorithm to the experimental data show that temperature estimates for 40 °C, 60 °C, and 80 °C are accurate to within ± 5 °C. Proceeding with crack localization using the estimated temperature, it was observed that when a generic and fixed prior is used to determine the probable crack location, the average crack localization error is approximately 9 mm. On the other hand, when the developed integrated dynamic prior approach is employed, the crack length was predicted with an error of less than 1 mm for most of the presented cases at various temperatures, demonstrating the benefit of incorporating the dynamic prior within the localization framework. Using the dynamic prior significantly reduced the computational time while increasing accuracy, as the search domain is smaller and closer to the actual crack location.

3 CHARACTERIZATION AND PREDICTION OF FATIGUE CRACK PROPAGATION UNDER COMPLEX BIAXIAL LOADING

3.1 Introduction

Metallic aerospace components are generally subjected to complex multiaxial loading, which may be a combination of biaxial proportional, non-proportional, in-phase, and out-of-phase loading conditions (Anderson & Garrett, 1980; Hopper & Miller, 1977; Mall & Perel, 2015). Although extensive studies have been conducted to understand their fatigue characteristics under uniaxial (constant and variable amplitude) loading, very few studies have reported the effects of multiaxial loading conditions on crack initiation and propagation (Gudlur, Boczek, Radovic, & Muliana, 2014; Haque & Saif, 2002; Oh, 1995; Stanzl-Tschegg, 2006; Xue, El Kadiri, Horstemeyer, Jordon, & Weiland, 2007). The time to failure depends on a multitude of variables, many of which are stochastic in nature. Variables include "usage" history, defect geometry and location, material used, and applied load characteristics, among many others. While recent studies have shown the effects of property variability and defects at the microstructural levelon crack initiation, manifestations of microstructural characteristics in macroscale phenomena under complex loading have not been adequately explained.

In this research, extensive quasi-static and fatigue tests were conducted to investigate the crack initiation and propagation in Al7075-T651 cruciform specimens subjected to in-phase and out-of-phase (45°, 90°, 180°) loading conditions. First, microstructural characterization was performed to understand the morphology of material microstructure and intermetallic particles. Fractography was subsequently performed on

the tested specimens to understand the crack initiation and propagation behavior. The hybrid prognosis model developed in Chapter 2 was extended to predict the fatigue crack propagation under biaxial loading. The prognosis model in Chapter 2 used SIF as the primary driving force for crack growth. The relationship between SIF and the crack growth rate was modeled using a modified version of Paris's law (Paris & Erdogan, 1963), using non-constant coefficients to account for uncertainties in loading conditions and crack growth behavior. However, since SIF was used as the physics based parameter in this model, it is applicable under uniaxial loading conditions only. Under biaxial loading conditions, the crack tip undergoes mixed mode fracture; therefore, the energy release rate, G, is a more appropriate physical parameter. The relationship between G and crack growth rate, however, is highly nonlinear. Therefore, linear adaptive models cannot be used to model the relationship. The hybrid prognosis model developed in Chapter 2 was modified to use G as the physics based parameter. An automated procedure was developed to evaluate G for complex geometries for different crack length and loading conditions, by integrating Python, Abaqus v6.7 (Simulia, 2007) and MATLAB (MathWorks, 2012). The Gaussian process (GP) (Rasmussen & Williams, 2006), which is a machine learning technique, was used to model the nonlinear relationship between G and the crack growth rate. The developed model is highly adaptive and constantly calibrates the GP model parameters as new experimental data becomes available. Since two cracks were observed to propagate under biaxial out-of-phase loading conditions, the prognosis model was developed to predict both single crack propagation and multiple crack propagation under in-phase and out-of-phase loading conditions, respectively.

This chapter is organized as follows. In Section 3.2, the results of microstructural

characterization are presented. Section 3.3 provides the details of the biaxial experimental setup for quasi-static and fatigue tests. The prognosis model is introduced in Section 3.4. The results of biaxial fatigue testing, fractography, and validation of the prognosis model are discussed in Section 3.5.

3.2   Material Characterization

Knowledge about the material constituents is essential for understanding the microscale crack initiation and propagation. Microstructural characterization of Al7075-T651 was conducted using energy dispersive x-ray spectroscopy (EDS) and fractography. The second phase particles were identified using scanning electron microscopy (SEM), and their phases and elements were identified using EDS. Fractography was performed on the fracture surfaces of fatigued specimens to understand the crack growth behavior at the microscale.

3.2.1   Identification of Second Phase Particles

EDS is an elemental analysis technique that employs high energy electrons incident on the specimen and displaces the electrons in the K shell of the atoms, creating a vacancy. When an outer shell electron fills in the K shell, characteristic x-ray wavelengths are emitted, which are used to identify the elements in the specimen, along with their weight fractions and atomic fractions. EDS analysis was performed on the healthy Al7075-T651 sample to identify the second phase (intermetallic) particles and their composition. These intermetallic particles are brittle in nature and act as crack initiation sites (Payne, Welsh, Christ Jr., Nardiello, & Papazian, 2010). Therefore, it is necessary to identify the intermetallic particles to analyze the crack propagation.

79

3.2.2   Sample Preparation

To obtain accurate results using EDS, the samples have to be polished such that the intermetallic particles are visible under SEM. A detailed polishing procedure was developed for preparing the specimen surface. The procedure was performed on a Struers LaboPol 5 polisher, as described in Table 3.1. Diamond suspensions of different particle sizes were used to incrementally increase the surface finish, and colloidal silica (OP-S) suspension with a particle size of 0.04 μm was used for the final polish. A LaboForce attachment was used on the polisher to apply the designated force. The polished surface and the puck used for polishing are shown in Figure 3.1. The black edges seen on the puck are due to carbon tape attached during EDS to make the sample conductive.
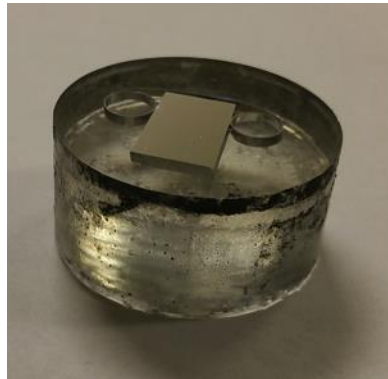
Figure 3.1 Polished Surface of Al7075-T651 Specimen, Along with the Puck.

Table 3.1 Polishing Procedure

Step	Surface	Abrasive type	Lubricant type	Speed (RPM)	Force (N)	Time (min)
1	SiC Foil #320	None	Water	300	30	4
2	SiC Foil #500	None	Water	300	30	3
3	SiC Foil #800	None	Water	300	30	3
4	Sic Foil #1200	None	Water	300	30	3
5	MD-Largo	DiaDuo-2 9μm	DiaDuo-2 9μm	300	30	4
6	MD-Dac	DiaDuo-2 6μm	DiaDuo-2 6μm	300	30	4
7	MD-Dac	DiaDuo-2 3μm	DiaDuo-2 3μm	300	30	4
8	MD-Nap	DiaDuo-2 1μm	DiaDuo-2 1μm	300	30	4
9	MD-Nap	OP-S 0.04 um	OP-S 0.04 um	300	30	3

3.2.3 Experimental Procedure

An XL30 field-emission gun environmental scanning electron microscope (ESEM–FEG) available at the Center for High Resolution Electron Microscopy (CHREM) laboratory, ASU, was used for performing EDS. The XL30 ESEM-FEG employs a stable, high-brightness, Schottky field emission source to provide exceptionally high quality observation of potentially problematic samples for conventional high vacuum SEMs. The XL30 has an energy dispersive x-ray analyzer from EDAX for elemental analysis, which has a particularly good geometry (takeoff

angle of 35°). The polished sample was mounted on a stub and fixed in the SEM chamber. A vacuum was created in the chamber, and a beam with voltage of 15kV was used with a spot size of 5. Energy dispersive spectrums were collected at different locations on the specimen surface and on the intermetallic particles.

3.2.4   Results and Discussion

The EDS analysis performed on the surface of the polished specimen is shown in Figure 3.2. The table in Figure 3.2 contains the percentage by weight (wt%) and percentage by number of atoms (at%) of each of the elements identified. Aluminum was the primary matrix element, but the analysis shows that there were other alloying elements, such as Mg, Ti, Cr, Mn, Fe, Cu, and Zn. Intermetallic particles were identified, and EDS was performed on the particles to determine their elemental composition. Two types of intermetallic particles were identified: Fe bearing and Si bearing. The composition of Fe bearing intermetallic particles, which primarily contain Al, Fe, and Cu, is shown in Figure 3.3.

Element	Wt%	At%
MgK	02.61	03.04
AlK	88.64	93.02
SiK	00.00	00.00
TiK	00.14	00.09
CrK	00.43	00.24
MnK	00.34	00.17
FeK	00.43	00.22
CuK	01.48	00.66
ZnK	05.92	02.57
Matrix	Correction	ZAF
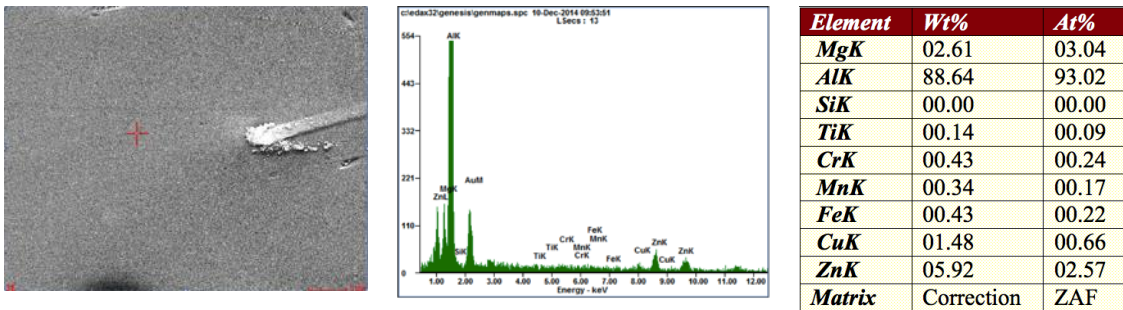
Figure 3.2 EDS Analysis Showing the Energy Spectrum and Elemental Compositions.

Element	Wt%	At%
MgK	01.06	01.35
AlK	74.80	85.91
SiK	00.00	00.00
TiK	00.19	00.12
CrK	00.41	00.24
MnK	00.42	00.24
FeK	13.72	07.61
CuK	04.92	02.40
ZnK	04.47	02.12
Matrix	Correction	ZAF
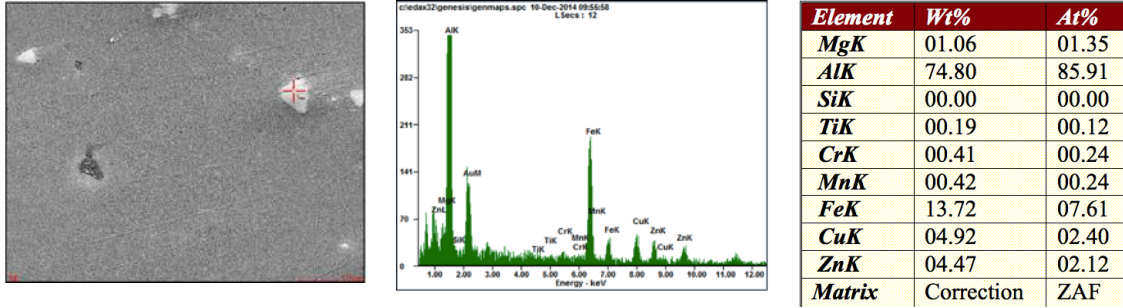
Figure 3.3 EDS Analysis Showing the Composition of Fe-rich Intermetallic Particles.

The composition of the Si bearing intermetallic particles, which primarily contain Mg and Si, is shown in Figure 3.4. The Fe bearing particles are brittle and hard, with their modulus greater than the matrix material, whereas the Si bearing particles are soft, with their modulus less than the matrix material (Payne et al., 2010). Micro cracks nucleate at the Fe rich intermetallic particles owing to the stress concentration at their boundaries (Xue et al., 2007). Area mapping, which shows the elemental distribution in the selected area of the surface of the specimen, was performed and the distributions are presented in Figure 3.5. The intermetallic particles (Fe and Si) are clearly identified in red and blue maps, respectively.

Element	Wt%	At%
MgK	02.64	03.12
AlK	58.50	62.36
SiK	29.39	30.10
TiK	00.48	00.29
CrK	00.67	00.37
MnK	00.33	00.17
FeK	00.60	00.31
CuK	01.64	00.74
ZnK	05.75	02.53
Matrix	Correction	ZAF
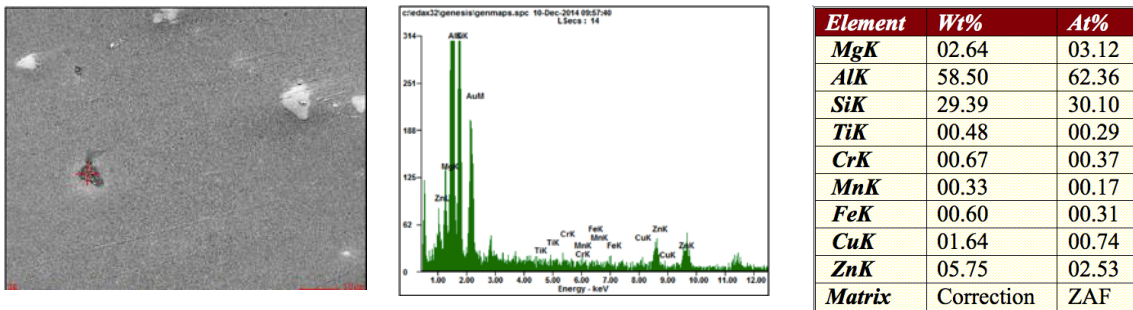
Figure 3.4 EDS Analysis Showing the Composition of Si-rich Intermetallic Particles.

SEM image	Al	Cr	Cu	Fe

Mg	Mn	Si	Ti	Zn
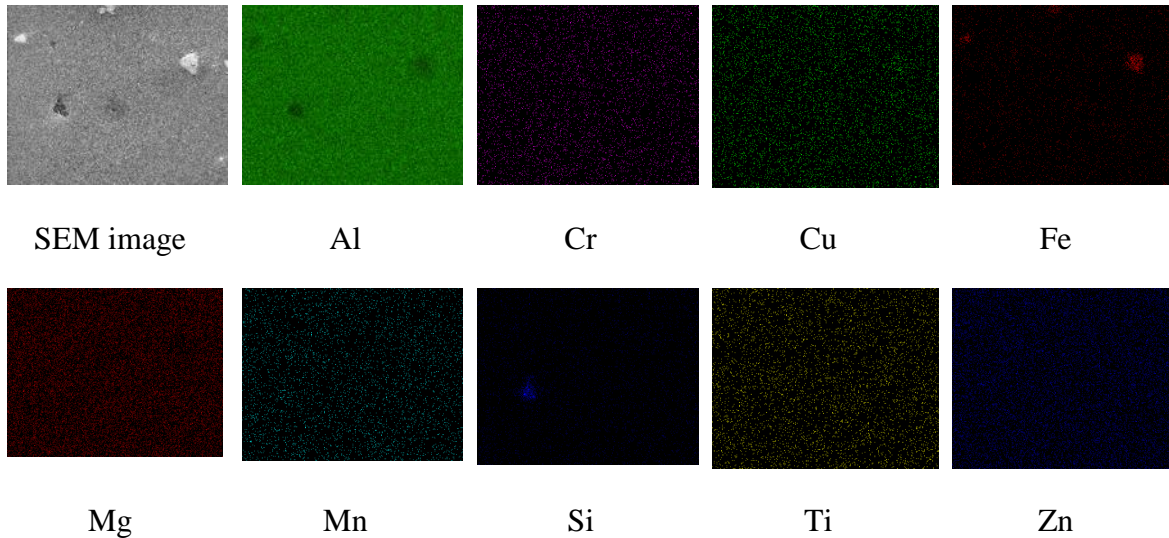
Figure 3.5 Elemental Distribution in a Specific Area on the Sample.

3.3   Biaxial Experimental Setup

Quasi-static   and   fatigue   experiments   were   conducted   using   the   MTS biaxial/torsion load frame with a static load capacity of 100 kN in both horizontal and vertical directions, as shown in

Figure 3.6. Quasi-static experiments allow the study of plastic deformation and monotonic fracture as damage modes, whereas the fatigue experiments emphasize crack nucleation and short crack propagation. Appropriate specimen design is essential to accurately capture the damage mechanisms associated with different loading conditions. Cruciform specimens as shown in Figure 3.7 were designed such that the central web area had uniform stress distribution for initial yielding. The specimens were machined from 6.35mm rolled Al7075-T651 sheets with a thickness of web area of 1.8mm. The length and width of the arms were 292mm and 48.35mm, respectively. A hole of diameter 6.35mm was cut at the center of the web area, and a notch of length 1.5mm and width 0.36mm was made at an angle of 45° (see Figure 3.7) to accelerate crack initiation.

Figure 3.6 Cruciform Specimen in Biaxial Test Frame.
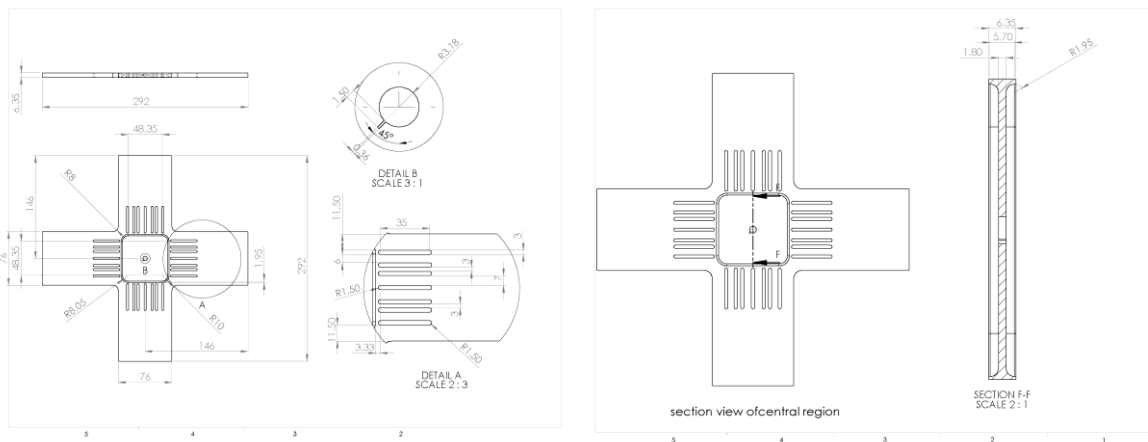
Figure 3.7 Cruciform Specimen with Dimensions.

An ARAMIS digital image correlation system (DIC) was used to capture the full strain field distribution in the gauge area where cracks initiate. Each specimen was painted to obtain the required speckle pattern, and the DIC was calibrated to make accurate measurements for each specimen. An additional camera was positioned on the rear side of the specimen to capture the crack initiation and growth. The camera was

programmed using LabVIEW to take images at a user defined time interval. A MATLAB

code was developed to convert the time stamp of the images into the number of cycles.

This enabled calculating the cycles for crack initiation, propagation, and final failure. The

crack length was measured using the DIC system, along with a high resolution optical

camera. The crack length as a function of cycles was calculated using image processing

software, ImageJ (Abràmoff, Magalhães, & Ram, 2004). Fatigue tests were conducted

under in-phase and out-of-phase loading conditions. It was observed that a single crack

propagated under in-phase loading and two cracks propagated under out-of-phase

loading. Detailed results from the fatigue tests are presented in Section 3.5.2.

Fractography was performed on the fatigued specimens to study the microstructural crack

growth features.

3.4 Prognosis Model

The crack growth rate at any instant of time is written as:

$$log \frac{da}{dN} = C_1\big(a_{N-1}, M_p, P_{N,N+1}, N\big) + C_2\big(a_{N-1}, M_p, P_{N,N+1}, N\big)log(\Delta K) \qquad (3.1)$$

where M_p is a material parameter, P is the load, (ΔK) is the SIF range, and N is the

number of cycles. The prognosis model described in Chapter 2 uses non-constant

coefficients C_1 and C_2, which are updated adaptively at each time step, based on the

previous crack length versus fatigue cycle data. In the case of biaxial loading, this

relationship is highly nonlinear, owing to the different possible loading scenarios such as

in-phase loading, out-of-phase loading, and different biaxiality ratios. Unlike uniaxial

loading, the crack in biaxial loading undergoes mixed mode fracture, and the use of

uniaxial SIF as a physics based parameter will lead to erroneous results. Therefore, in this study, G was used as the driving force for crack growth, and is written as:

$$G = \frac{K_1^2}{E} + \frac{K_2^2}{E}; \ \Delta G = G_{max} - G_{min},$$
(3.2)

where E is the Young's modulus, K_1 and K_2 are the mode-I and mode-II SIFs, respectively, and G_{max} and G_{min} are the energy release rate values corresponding to maximum and minimum amplitude of the cyclic loading. A machine learning model that adaptively learns and infers the relationship between the input and output parameters has been developed to accurately model the nonlinear relationship between G and the crack growth rate. Gaussian process regression (Rasmussen & Williams, 2006), which is a robust machine learning technique, is used to model the complex nonlinear relationship. The GP is a collection of random variables, any finite number of which have a joint Gaussian distribution. The predictions are made by projecting the input space to the output space by inferring their underlying nonlinear relationship. Once the algorithm is trained with the input and output parameters, it can predict the output parameter for new sets of input parameters.

Since cruciform specimens with highly complex geometry were used in this study, explicit equations for G cannot be derived; therefore, GP was used to model the complex nonlinear relationship between crack length and G. Furthermore, the crack propagation path under biaxial loading depends highly on the biaxiality ratio; therefore, the direction of crack propagation will significantly affect the G calculations. In this research, instead of using the crack length, the crack tip location, which provides

87

information about both the crack length and the propagation direction, was used to find

G. The center of the cruciform specimen was chosen to be the origin, and the G value

was calculated for different crack tip locations under different loading conditions by

performing a quasi-static finite element analysis. GP was then used to create the high-

dimensional mapping of G as a function of the crack tip locations. The developed

prognosis model is capable of predicting crack propagation under both in-phase and out-

of-phase biaxial loading conditions. Since the experimental data suggests the crack

propagated along a straight line, curved cracks were not considered in this study.

3.4.1 In-phase Loading

For in-phase loading, G was modeled as a function of the single crack tip location

and loads in x and y directions:

$$f\left(\boldsymbol{G}|\boldsymbol{T_{ip}}, \boldsymbol{K_{ip}}(\mathbf{x}_i, \mathbf{x}_j), \boldsymbol{\theta}\right) = \frac{1}{Z} exp\left(-\frac{(\boldsymbol{G} - \mu_G)^2}{2\sigma_G^2}\right); i, j = 1, \dots, M_r, \qquad (3.3)$$

where $\boldsymbol{G}$ is the vector of energy release rate evaluated at each point on the test grid

(obtained from finite element solutions), $\boldsymbol{K_{ip}}$ is the kernel matrix, M_r denotes the number

of rows in the grid, $\boldsymbol{T_{ip}}=\{\mathbf{x}_i,\boldsymbol{G}_i\}$ is the training matrix comprising four input parameters

(crack tip locations (x, y), loads in x and y directions) and one output parameter

(corresponding G values at the grid points), Z is a normalizing constant, and $\boldsymbol{\theta}$ is a vector

of hyper-parameters (HPs). The mean and variance of the distribution were obtained as

follows:

$$\mu_G = \mathbf{k}_{test}^T \mathbf{K}_{train}^{-1}(G)_{train}; \sigma_{\frac{da}{dN}}^2 = \kappa - \mathbf{k}_{test}^T \mathbf{K}_{train}^{-1}\mathbf{k}_{test}, \qquad (3.4)$$

where subscripts *train* and *test* are used to represent the training and the test data, respectively, which were obtained from finite element simulations and represented the test points where *G* had to be evaluated. The partitioned components of the kernel matrix, κ, $\mathbf{k}_{test}$, and $\mathbf{K}_{train}$, are given by:

$$\kappa = k(\mathbf{x}_{test},\ \mathbf{x}_{test}) \quad ; \quad \mathrm{k}_i = k(\mathbf{x}_{test},\ \mathbf{x}_i)_{i=train} ; \quad K_{i,j} = k(\mathbf{x}_i,\ \mathbf{x}_j)_{i,j=train,} \tag{3.5}$$

and *k* is the kernel function.

The accuracy of prediction in a prognosis model depends on the choice of kernel function and the HPs. Since the kernel function guides the behavior of the high-dimensional mapping, it is necessary to choose appropriate kernel function based on the data. Different kernel functions such as squared exponential, rational quadratic, and multilayer perceptron kernel functions have been used in the literature. A squared exponential kernel function shown in Equation 2.6 was used in the present study; this kernel function is suitable for modeling nonlinear smooth surfaces and was successfully used (Neerukatti, Fard, Kim, & Chattopadhyay, 2014) in high-dimensional mapping.

$$k(\mathbf{x}_i, \mathbf{x}_j) = \theta_1^2 exp\left(\frac{(\mathbf{x}_i - \mathbf{x}_j)^2}{\theta_2^2}\right), \tag{3.6}$$

The optimum values of the HPs are obtained by minimizing the negative log marginal likelihood (*L*) given by:

$$L = -\frac{1}{2}\log \det \boldsymbol{K}_{test} - \frac{1}{2}(\boldsymbol{G})_{train}^T \mathbf{K}_{train}^{-1}(\boldsymbol{G})_{train} - \frac{N_{train}}{2}log2\pi, \tag{3.7}$$

where N_{train} denotes the number of training input–output pairs. Once the optimal HPs are found, the value of G can be calculated for any experimentally determined crack length and loading condition. Next, the relationship between the crack growth rate and G has to be modeled to calculate the crack growth rate for G obtained using Equations 3.3–3.7. Then, the crack length at any given time instant ($N + \Delta N\ cycles$) can be predicted using the crack growth rate as:

$$a_{N+\Delta N} = a_N + \left(\frac{da}{dN}\right)_N * \Delta N, \tag{3.8}$$

The direction of crack propagation is assumed to be the same as the crack direction in the previous time step. To calculate the crack growth rate at the Nth cycle, a relationship has to be derived between the crack growth rate and G. Since the relationship between crack growth rate and G is exponential or highly nonlinear, depending on the type of loading, a linear relationship in the log–log scale cannot be used. In this chapter, GP was used to model the complex nonlinear relationship between crack growth rate and G. The advantage of using a GP model is that the parameters can be adaptively updated as more training data becomes available. Therefore, instead of using a single explicit equation with correction factors, the model adaptively changes with the data. This facilitates the application of this methodology to complex geometries and loading conditions.

The relationship between G and da/dN is modeled using GP as:

$$f\left(\frac{da}{dN}\Big|\boldsymbol{T}, \boldsymbol{K}_{N-\Delta N}(\mathbf{x}_i, \mathbf{x}_j), \boldsymbol{\theta}\right) = \frac{1}{Z} exp\left(-\frac{\left(\frac{da}{dN} - \mu_{\frac{da}{dN}}\right)^2}{2\sigma_{\frac{da}{dN}}^2}\right); \tag{3.9}$$

$$i, j = 1, \dots, N,$$

where $\boldsymbol{T}=\{\mathbf{x}_i, \left(\frac{da}{dN}\right)_{i=1}^{N-\Delta N}\}$ is the training data set, $\mathbf{x}_i$ and $\mathbf{x}_j$ are the rows of training matrix $\boldsymbol{T}$

(each row contains the values of G), $\mu_{\frac{da}{dN}}$ is the mean, and $\sigma_{\frac{da}{dN}}^2$ is the variance of the

distribution obtained as:

$$\mu_{\frac{da}{dN}} = \mathbf{k}_N^T \mathbf{K}_{N-\Delta N}^{-1} \left(\frac{da}{dN}\right)_{N-\Delta N}; \qquad \sigma_{\frac{da}{dN}}^2 = \kappa - \mathbf{k}_N^T \mathbf{K}_{N-\Delta N}^{-1} \mathbf{k}_N, \tag{3.10}$$

where κ, $\mathbf{k}_{N+\Delta N}$, and $\mathbf{K}_N$ are the partitioned components of Nth instances of kernel matrix

given by:

$$\kappa = k(\mathbf{x}_N, \mathbf{x}_N) \quad ; \quad \mathbf{k}_i = k(\mathbf{x}_N, \mathbf{x}_i)_{i=1,2,\dots,N-\Delta N} ; \quad K_{i,j} = k(\mathbf{x}_i, \mathbf{x}_j)_{i,j=1,2,\dots,N-\Delta N} \tag{3.11}$$

and the optimal HPs are derived through minimizing the negative log marginal likelihood

(L) given by:

$$L = -\frac{1}{2}\log \det \boldsymbol{K}_N - \frac{1}{2}\left(\frac{da}{dN}\right)_{1:N-\Delta N}^T \mathbf{K}_{N-\Delta N}^{-1}\left(\frac{da}{dN}\right)_{1:N-\Delta N}$$
$$-\frac{N-\Delta N}{2}\log 2\pi. \tag{3.12}$$

Once the crack growth rate is evaluated, both one-step ahead and multi-step ahead

predictions of the crack length are made. One-step ahead implies that the prediction of

crack length is made at the next time step where the measured crack length is available

(using Equation 2.9). In multi-step ahead, the crack length is predicted until a critical value is reached or the specimen fails. Multi-step ahead predictions are made as follows:

$$a_{N_2} = a_{N_1} + \sum_{i=1}^{n} \left(\frac{da}{dN}\right)_i * (\Delta N)_i, \tag{3.13}$$

where N_1 is the current number of cycles, N_2 is the number of cycles up to which the predictions are made, $n = \frac{N_2 - N_1}{m}$, m is the number of time steps, $(\Delta N)_i$ is the cycles in the ith time step, and $\left(\frac{da}{dN}\right)_i$ is the crack growth rate at the ith time step calculated using Equations 3.3 and 2.9. Since no prior knowledge is available about the behavior of the curve for multi-step ahead predictions, a cross-validation methodology is used to accurately calculate the crack growth rate. If the long-term predictions are to be made starting at i^{th} data point, the data up to the $(i-1)^{th}$ data point are used to train the model, and the crack length is predicted at the ith data point. Since the crack length at the ith data point is known, the model can be tuned to match this value. Using this method, the model can be adaptively updated for crack growth behavior under any loading conditions. The tuned model is then used to make crack length predictions.

3.4.2 Out-of-phase Loading

In the case of out-of-phase loading, it is necessary to account for the different energy release rates and crack length, owing to the two cracks that initiate and propagate simultaneously at an angle of approximately 90° to each other. To account for this in the prognosis model, a mapping for G is created as follows:

$$f\left(\boldsymbol{G_1}|\boldsymbol{T_{op}}, \boldsymbol{K_{op}}(\mathbf{x}_i, \mathbf{x}_j), \boldsymbol{\theta}\right) = \frac{1}{Z} exp\left(-\frac{\left(\boldsymbol{G_1} - \mu_{\boldsymbol{G_1}}\right)^2}{2\sigma_{\boldsymbol{G_1}}^2}\right); i, j$$

(3.14)

$$= 1, \dots, M_{op},$$

$$f\left(\boldsymbol{G_2}|\boldsymbol{T_{op}}, \boldsymbol{K_{op}}(\mathbf{x}_i, \mathbf{x}_j), \boldsymbol{\theta}\right) = \frac{1}{Z} exp\left(-\frac{\left(\boldsymbol{G_2} - \mu_{\boldsymbol{G_2}}\right)^2}{2\sigma_{\boldsymbol{G_2}}^2}\right); i, j$$

(3.15)

$$= 1, \dots, M_{op},$$

where $\boldsymbol{T_{op}}$ is the training set containing the six input parameters (crack tip locations (x, y) for two cracks, loads in x and y directions) and two output parameters (energy release rate for two cracks), $\boldsymbol{K_{op}}$ is the kernel matrix for squared exponential kernel function, and $\boldsymbol{G_1}$ and $\boldsymbol{G_2}$ are the vectors of energy release rates for both the cracks evaluated at the grid points. The mean and variance for G_1 and G_2 are calculated similar to Equations 2.4–2.5. The relationship between G and crack growth rate for both cracks is then modeled as:

$$f\left(\frac{da_1}{dN}|\boldsymbol{T}, \boldsymbol{K_{N-\Delta N}}(\mathbf{x}_i, \mathbf{x}_j), \boldsymbol{\theta}\right) = \frac{1}{Z} exp\left(-\frac{\left(\frac{da_1}{dN} - \mu_{\frac{da_1}{dN}}\right)^2}{2\sigma_{\frac{da_1}{dN}}^2}\right);$$

(3.16)

$$i, j = 1, \dots, N,$$

$$f\left(\frac{da_2}{dN}|\boldsymbol{T}, \boldsymbol{K_{N-\Delta N}}(\mathbf{x}_i, \mathbf{x}_j), \boldsymbol{\theta}\right) = \frac{1}{Z} exp\left(-\frac{\left(\frac{da_2}{dN} - \mu_{\frac{da_2}{dN}}\right)^2}{2\sigma_{\frac{da_2}{dN}}^2}\right);$$

(3.17)

$$i, j = 1, \dots, N,$$

where the mean and variance are calculated similar to Equations 3.10–3.11. Finally, one-step ahead and multi-step ahead predictions can be made as:

$$a_{1,N+\Delta N} = a_{1,N} + \left(\frac{da_1}{dN}\right)_N * \Delta N \; ; \; a_{2,N+\Delta N} = a_{2,N} + \left(\frac{da_2}{dN}\right)_N * \Delta N, \qquad (3.18)$$

where a_1 and a_2 are the lengths of the two cracks respectively.

3.5 Results and Discussion

In this section, the results of proportional and non-proportional quasi-static tests are presented first. The results of experimental crack propagation, fractography, and the prognosis model under in-phase and out-of-phase loading conditions are presented next.

3.5.1 Quasi-static Tests

Quasi-static tests were performed to obtain the loads necessary for low cycle and high cycle fatigue testing. The cruciform sample was loaded in tension up to the maximum capacity of the frame (100 kN) in both x and y directions, and the tests were conducted for different values of the biaxiality ratio, BR = 0.25, 0.5, 1, 2, 4, defined as the ratio of load between x and y axes. The results are summarized in

Table 3.2 and show very small differences in the maximum failure load. This can be attributed to the 45° notch angle. Since the notch is symmetric with respect to both x and y axis, the crack path remains perpendicular to the maximum loading direction, and fails when the critical load is reached. The major strain contour of the gauge area, obtained from DIC, immediately before failure is shown in Figure 3.8. Strain concentration is observed in the vicinity of the crack, resulting in specimen failure. The force-displacement curve for BR=1 up to failure is shown in Figure 3.9.

Table 3.2 Static Test Results

Test	Biaxiality ratio (X/Y)	Failure load (N) (X, Y)	Time to failure (s)
1	1	78971, 78965	1211
2	0.5	90108, 45157	1384
3	0.25	82019, 20548	1257
4	2	39718, 79161	1217
5	4	20150, 78818	1240
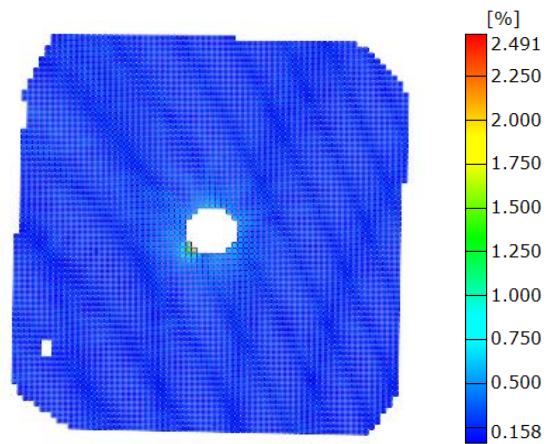
Figure 3.8 Major Strain Contour Before Failure.
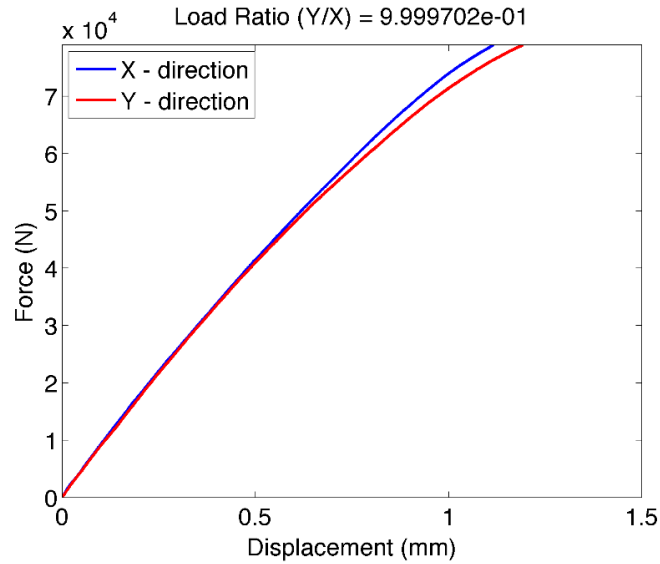
Figure 3.9 Force-displacement Curve for BR=1.

3.5.2 Fatigue Tests

Two cyclic load conditions with a maximum force of 15 kN and 30 kN for cases (i) and (ii), respectively, were selected based on the results of quasi-static tests; these loads corresponded to 25% and 50% of the yield stress. The load ratio for both cases was 0.1 ((i) **Load1**: 1.5 kN – 15 kN and (ii) **Load2**: 3 kN – 30 kN). When Load1 was applied along both the axes, the fatigue life exceeded 75000 cycles; when Load2 was applied, the fatigue life was considerably shorter, at approximately 11300 cycles. Here, the fatigue life is defined as the number of cycles till the complete fracture of the specimen. These two loading conditions were chosen to capture the behavior under very high and relatively low loads (low cycle and high cycle fatigue). In-phase is defined such that the cyclic loading along the *x* and *y* directions are synchronized and there is no phase difference between the sinusoidal loads. For out-of-phase tests, a phase difference of 45°, 90°, and 180° was introduced. Since the fatigue life under Load2 was significantly lower,

96

Load1 was used to perform all the experiments, since it enables better understanding of the crack growth features. Table 3.3 summarizes the details of the fatigue tests performed, along with the number of cycles for crack initiation and specimen failure.

Table 3.3 Biaxial Testing under Varying Load Conditions

Test	x load	y load	Frequency (Hz)	Phase difference (°)	Cycles to 1mm crack	Cycles to failure
1	Load2	Load2	10	0	2100	11300
2	Load1	Load1	10	0	6000	87087
3	Load1	Load1	15	0	6000	78578
4	Load1	Load2	10	0	1800	13971
5	Load2	Load1	10	0	1800	10851
6	Load1	Load1	10	45	4500	63000
7	Load1	Load1	10	45	5500	82000
8	Load1	Load1	10	45	6000	76800
9	Load1	Load1	10	90	22800	131800
10	Load1	Load1	10	90	16100	135700
11	Load1	Load1	10	90	17400	120600
12	Load1	Load1	10	180	18900	75000
13	Load1	Load1	10	180	18300	70000
14	Load1	Load1	10	180	11700	60000

Load1: 1.5–15kN; Load2: 3–30kN.

3.5.2.1　In-phase Loading

3.5.2.1.1　Experimental Crack Propagation Behavior

For in-phase loading, a single crack initiated and propagated perpendicular to the maximum load, as shown in Figure 3.10. A secondary crack was also observed to initiate and propagate in the opposite direction, owing to the stress concentrations at the opposite side of the hole created by the opening of the primary crack. The results in Figure 3.10a and Figure 3.10b indicate that the crack always propagated perpendicular to the maximum tangential stress. The fatigue life under these loading conditions was very similar at 10851 and 13971 cycles, respectively. Similarly, Figure 3.10c shows that the crack propagated at an angle of approximately 45° when the load was equal along horizontal and vertical directions. In all these cases, a secondary crack initiated and propagated in the opposite direction, owing to the stress concentrations created by the opening and closing of the primary crack.
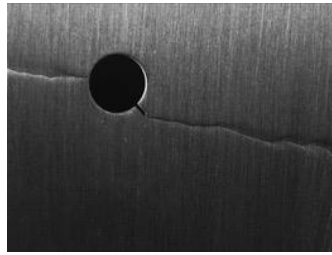
(a) Load x: 3-30 kN; Load y: 1.5-15 kN　(b) Load x: 1.5-15 kN; Load y: 3-30 kN　(c) Load x: 1.5-15 kN; Load y: 1.5-15 kN
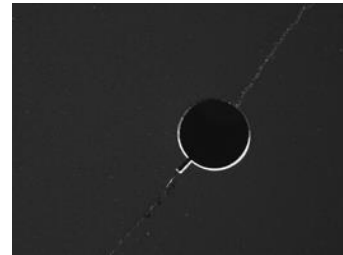
Figure 3.10 Crack Growth under Biaxial In-phase Loading.

3.5.2.1.2 Fractography

The fracture surface was studied for the crack shown in Figure 3.10c to understand the crack initiation and propagation behavior. The crack propagation is primarily driven by the stress intensity factor range (ΔK); the fracture surface comprises three different morphologies, with the operative mechanism dependent on ΔK. The fracture surface of stage I crack growth (low ΔK) regime is shown in Figure 3.11. The highly tortuous crack path due to the crack propagation along the intense slip bands, resulting in heterogeneous deformation and tortuous crack growth, is shown in Figure 3.11a. The features of crystallographic facets near the crack initiation site are shown in Figure 3.11b, and Figure 3.11c shows the cracked Fe rich intermetallic particle near the crack initiation, which indicates that the Fe rich particles served as the crack initiation sites because of their higher modulus with respect to the matrix.
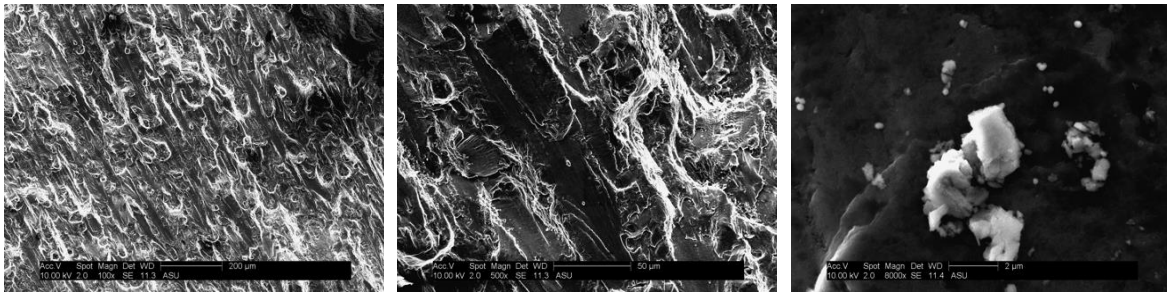
(a) Stage I morphology showing tortuous crack path

(b) Angular crystallographic facets near crack initiation

(c) Cracked Fe rich intermetallic particle near the crack initiation site

Figure 3.11 Fracture Surface in Stage I Crack Growth Regime.

Cleavage facets were observed in the transition between stage I and stage II crack growth regimes, as shown in Figure 3.12a. The cleavage facets merged in the direction of crack growth; this information can be used to identify the crack initiation and growth

events, and these facets transitioned into fatigue striations, as shown in Figure 3.12b. In the stage II crack growth regime, multiple slip systems were activated and the deformation was homogeneous. The fatigue striations (Figure 3.12b) were oriented perpendicular to the crack growth direction, and the spacing between the striations could be correlated with the crack growth rate. The distance between two striations is the crack growth per unit fatigue cycle. When the size of plastic zone exceeds the mean grain diameter, fatigue striations often extend over multiple grains. In the fast fracture regime (stage III), a dimpled structure, which is a characteristic of monotonic ductile fracture, was observed. As the crack length increased, the fracture surface showed higher density of dimples resembling static ductile fracture mode. Fading striations and appearance of dimples are shown in Figure 3.13a, which suggests a highly ductile fracture mode. The dimples nucleate at the inclusions, forming microvoids that grow and coalesce (Srivatsan, Sriram, Veeraraghavan, & Vasudevan, 1997). High density of dimples were observed toward the end of the stage III crack growth regime (Figure 3.13b) indicating static ductile fracture. From the crack propagation behavior observed from camera images and fractography results, it can be concluded that the crack driving force under in-phase biaxial fatigue loading was essentially mode-I in nature.
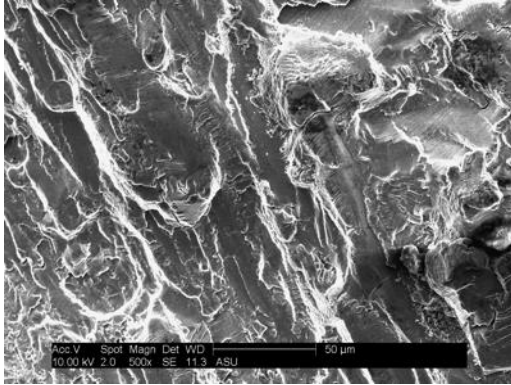
(a) Cleavage facets
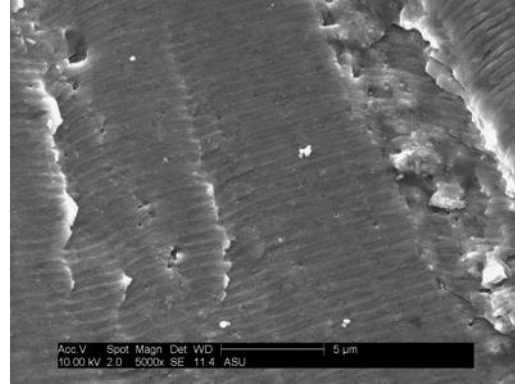
(b) Fatigue striations

Figure 3.12 Fracture Surface in Stage II Crack Growth Regime.
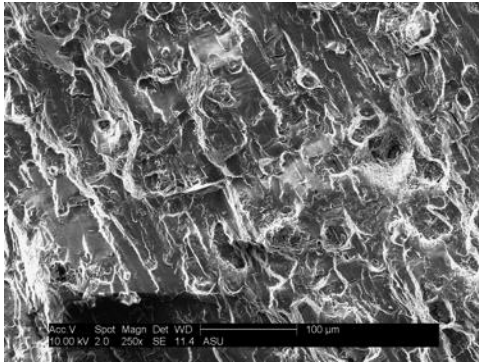
(a) Fading striations and
    appearance of dimples
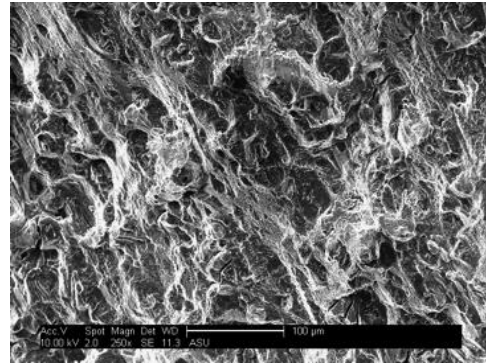
(b) High density of dimples
    resembling static ductile fracture

Figure 3.13 Fracture Surface in Stage III Crack Growth Regime.

3.5.2.1.3 Crack Length Prediction using Hybrid Prognosis

As described in Section 3.5.2.1.1, a single crack initiated and propagated under biaxial in-phase loading. Therefore, the first step in the proposed prognosis model was to create a mapping for G as a function of the crack tip location and the loading conditions. Analytical equations are available to calculate G for simple geometries, but since the

cruciform specimen used in this study had a complex geometry, J-integral (Rice, 1968) based approach was used in a finite element framework to calculate G.

A quasi-static finite-element simulation of the three-dimensional cruciform was performed to evaluate G using Abaqus/Standard. The direction of crack propagation was considered along the direction of the crack (i.e., normal to the crack front plane). The center of the cruciform was considered as the origin, and 39 different crack tip locations were modeled. The finite element model, along with the mesh, is shown in Figure 3.14. A fine mesh was created near the crack tip location to ensure accurate contour integral calculations. Since the model is generalized for varying biaxiality ratio, for each crack tip location, G was evaluated for different loads along x and y directions. The loads in each arm were varied from 7.5 kN to 15 kN with an increment of 2.5 kN in each direction.

(a) Finite element model   (b) Finite element mesh
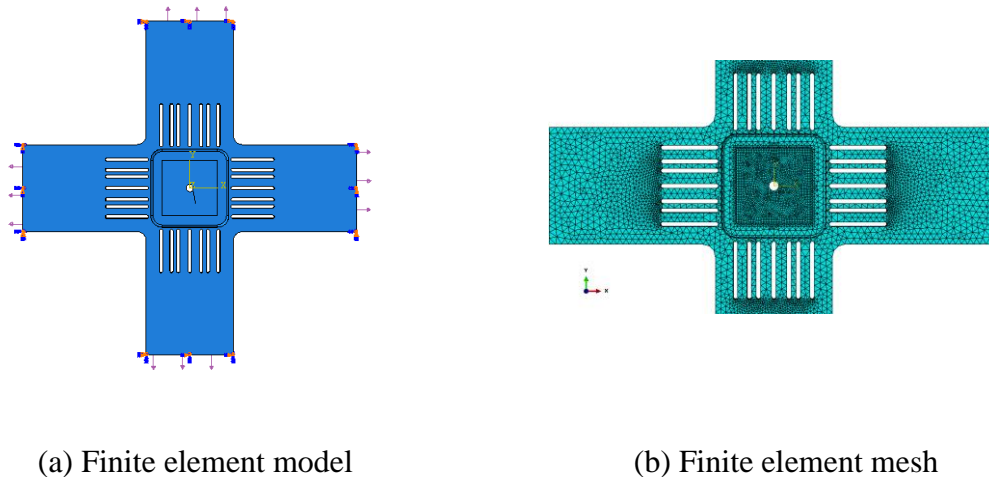
Figure 3.14 Finite Element Model and Mesh for Evaluating G.

A total of 216 simulations with different combinations of loads and crack tip locations were performed. The mapping was created on a grid between the minimum and

maximum values of the input parameters with a resolution of 0.01 units, using Equations 3.3–3.7. To check the accuracy of the mapping, cross-validation was performed using 160 random samples for training and 66 random samples for testing. The coefficient of determination of the mapping was 0.9904, which shows that the mapping was highly accurate. Since the input data was high-dimensional with four input parameters (x and y crack tip locations, x and y loads), it is difficult to visualize the surface created using the mapping. Therefore, for visualization of the mapping, G is presented for different combinations of loads and crack tip locations in Figure 3.15. It must be noted that the relationship is highly nonlinear; therefore, simple regression models cannot be used to accurately capture this relationship. After evaluating G, the crack growth rate was determined using Equation 2.9.
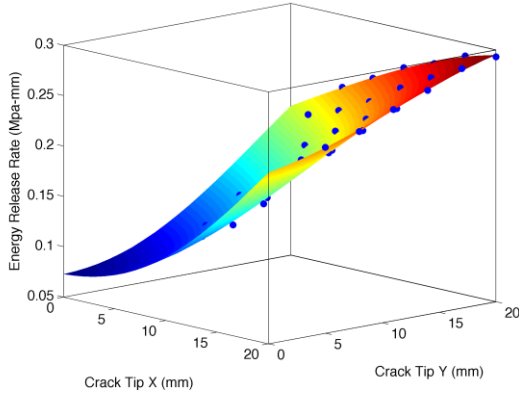
(a) G as a function of crack tip locations for a load of 7.5 kN in both X and Y directions
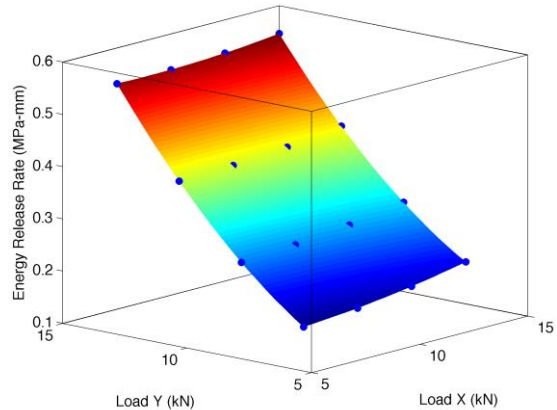
(b) G as a function of the loads for the crack tip location (11,-5) mm
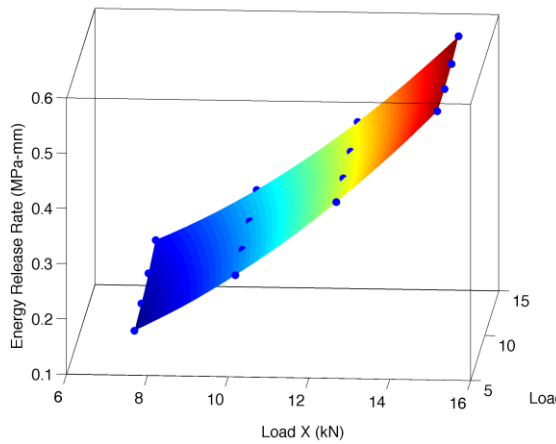
(c) *G* as a function of the loads for the crack tip location (5,-11) mm
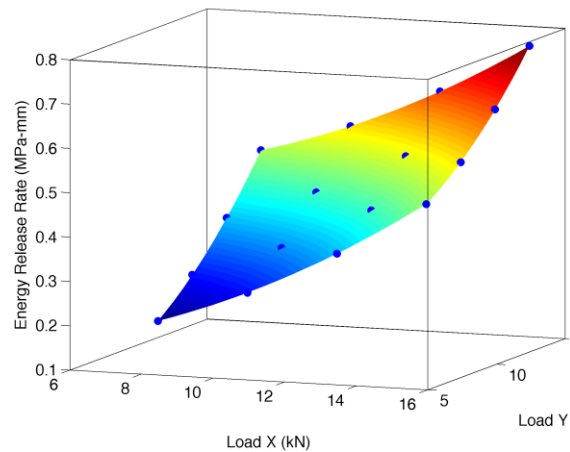
(d) *G* as a function of the loads for the crack tip location (11,-11) mm

Figure 3.15 Mapping for Energy Release Rate (*G*).

The one-step ahead predictions were made first using Equation 2.9 with the crack growth rate $\left(\frac{da}{dN}\right)_N$ calculated using Equations 3.3 and 2.9. The predictions made for two different in-phase loading conditions, (a) load in *y* direction greater than *x* direction, and (b) load in *x* direction greater than *y* direction, are shown in Figure 3.16. The predictions were made starting at the fifth data point, and the results show that the crack length predictions were highly accurate and within the 95% confidence interval for both cases. The gray band in the figure shows the 95% confidence interval.

Next, multi-step ahead predictions were made using the prognosis model (Equation 3.13). The crack growth rate $\left(\frac{da}{dN}\right)_i$ was calculated using Equations 3.3 and 2.9. The long-term predictions starting at the third data point are shown in Figure 3.17a. Since no prior knowledge was available about the behavior of the curve, the cross-validation methodology described in Section 3.4 was used to calculate the crack growth rate. The

104

variation HPs (θ) with every iteration are shown in Figure 3.17b. Since the prognosis model is adaptive, the crack length predicted at each time step was added to the training set, and the HPs were recalculated using the updated data.
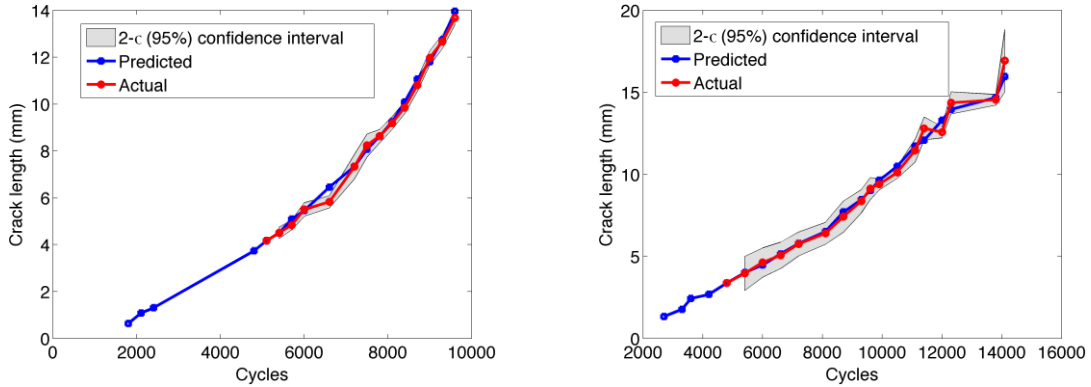
(a) Load X=1.5–15 kN; Load Y=3–30 kN   (b) Load X=3–30 kN; Load Y=1.5–15 kN

Figure 3.16 One-step Ahead Predictions for In-phase Loading.
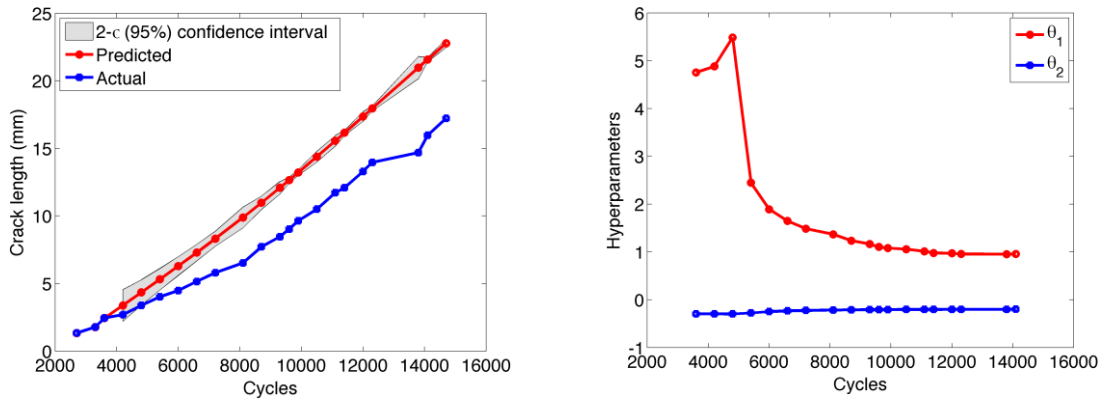
(a) Actual vs. predicted crack length   (b) Variation of HPs with cycles

Figure 3.17 Predictions of Crack Length Starting at Third Data Point for the Loads of 1.5–15 kN in x-direction and 3–30 kN in y-direction.

The results presented in Figure 3.17a show relatively large prediction errors,

arising from the very limited training data used (only three data points) and the absence of prior knowledge. The results of the prediction starting from the fifth and seventh data point, for loads 1.5–15 kN in the *x* direction and 3–30 kN in the *y* direction, are shown in Figure 3.18. The accuracy in prediction increased with training data, and the crack length predictions could be made within the 95% confidence interval when seven data points were used. The algorithm can be adapted to make accurate predictions with sparse data by using prior knowledge from a different set of experiments conducted under similar loading conditions.

(a) Predictions starting at fifth data point   (b) Predictions starting at seventh data point
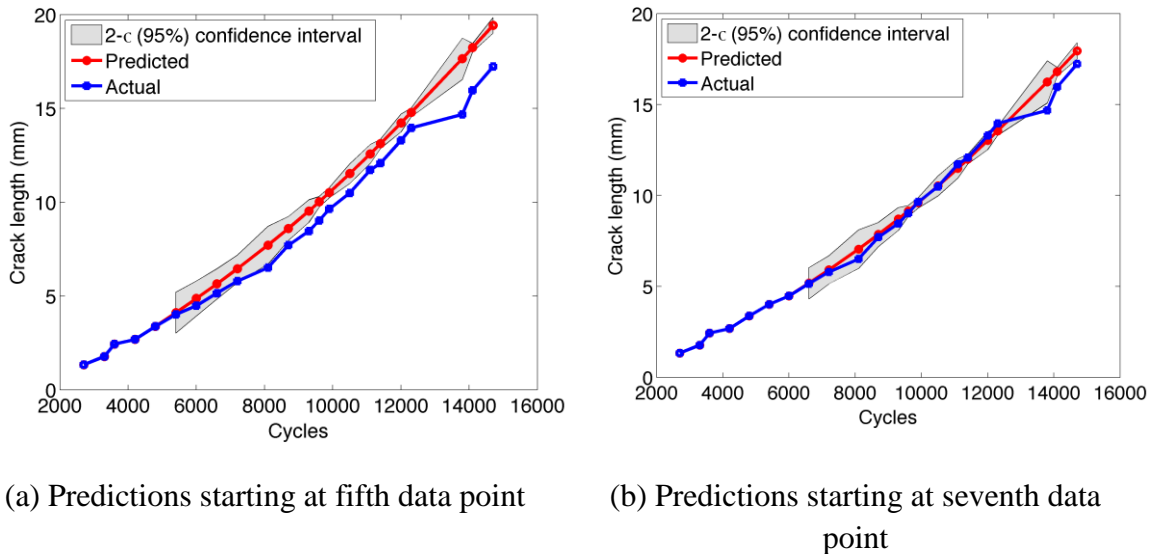
Figure 3.18 Long-term Predictions Starting at Fifth and Seventh data Points for the Loads of 1.5–15 kN in x-direction and 3–30 kN in y-direction.

The predictions made starting at the fifth and seventh data points for load range of 3–30kN in the *x* direction and 1.5–15kN in the *y* direction are shown in Figure 3.19. The results show that the crack length was predicted within the 95% confidence interval. It should also be noted that the number of cycles to failure was different for both the

specimens, and the prognosis model was able to adapt to the data and make accurate predictions.
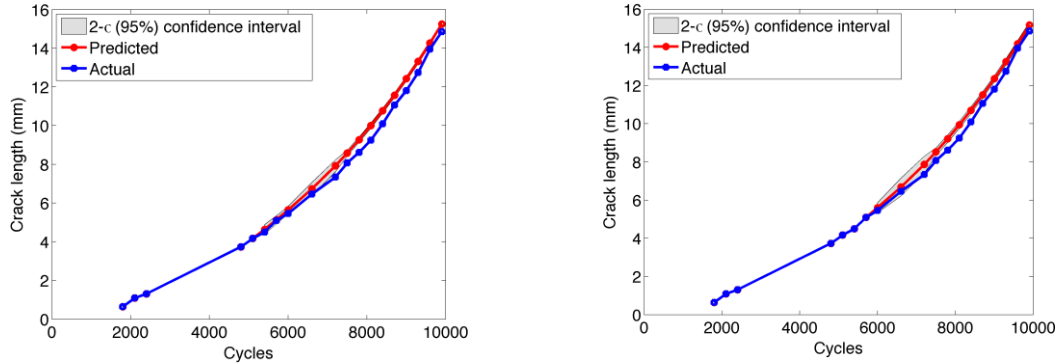
(a) Predictions starting at fifth data point

(b) Predictions starting at seventh data point

Figure 3.19 Predictions of Crack Length Starting at Fifth and Seventh Data Point for Loads of 3–30 kN in *x* direction and 1.5–15 kN in *y* direction.

3.5.2.2 Out-of-phase Loading

Three different phase differences—45°, 90°, and 180°—were studied to understand the effect of mixed mode fracture on the crack propagation behavior. Under out-of-phase loading, a mixed-mode stress state is expected, with the K_I/K_{II} ratio varying with the direction of the crack and the instantaneous ratio of the applied biaxial stresses. Since the notch was at 45° to the loading axis, the stress at the notch tip was purely mode-I ($K_{II} = 0$) when in-phase loading with BR=1 was applied. The introduction of a phase difference gives rise to stress components that contributes to K_{II} in addition to K_I, which results in a mixed-mode stress state (Buchholz, Chergui, & Richard, 2004), and the influence of K_{II} increases as phase difference increases from 0° to 180°. During the out-of-phase cyclic loading, SIF became purely mode-I at the instant when the load in *x* and *y*

107

directions reached the same magnitude. Subsequently, as the difference between the loads increased, K_{II} increased accordingly. The crack paths under different phase differences in loading are shown in Figure 3.20, and the crack formation mechanism is discussed in detail in Sections 3.5.2.3–3.5.2.5.

(a) Phase difference = 45°   (b) Phase difference = 90°   (c) Phase difference = 180°

Figure 3.20 Crack Growth under Biaxial Out-of-phase Loading.

3.5.2.3   Phase Difference of 45°

3.5.2.3.1 Experimental Crack Propagation Behavior

A single crack was observed to initiate and propagate (Figure 3.20a) under a phase difference of 45°, and the fatigue life was similar to the specimens under in-phase loading (approximately 80000 cycles). The plots of crack length and crack growth rate as a function of the number of cycles are shown in Figure 3.21. No significant change in the expected crack growth was observed with the crack growth rates in the order of 10^{-3} mm/cycle. This indicates the absence of a contribution from K_{II} on the crack growth behavior, since the instantaneous difference between the loads in x and y directions was insignificant for the 45° case. This behavior was further verified by analyzing the fracture surface of the crack.

(a) Crack length   (b) Crack growth rate
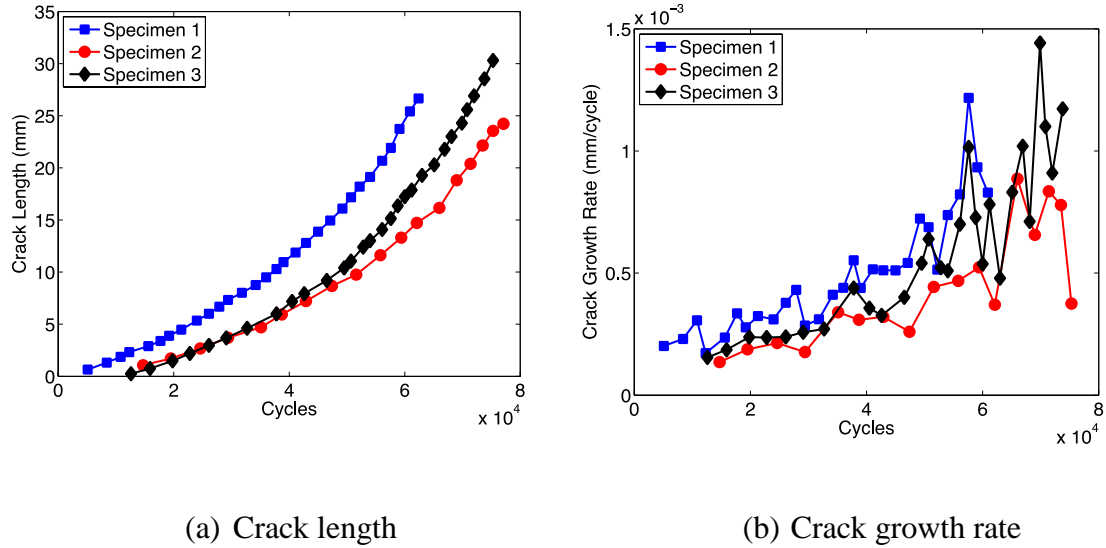
Figure 3.21 Fatigue Crack Growth under 45° Phase Difference.

3.5.2.3.2 Fractography

Fractography was performed to study the crack growth mechanism, and the results are shown in Figure 3.22. The near threshold regime (Stage I) crack growth behavior shown in Figure 3.22a indicates that pronounced intermetallic particle shearing was a dominant feature in the region of crack initiation. Transgranular cracking and faceted, crystallographic fracture mode were also observed in the crack initiation region (Figure 3.22b), but these features were not as common as intermetallic particle fracture. Since the influence of K_{II} was not as high compared to the 90° and 180° phase difference cases and mode-I remained the dominant form of fracture, a lower fatigue life to crack initiation was observed; this was also reflected in the fracture features that lacked angular facets and unevenness. As the crack growth approached stage II, slip steps with superimposed fatigue striations, which indicate the influence of K_{II}, became more prominent (Figure 3.22c). Merati, Hellier, and Zarabi (2012) reported the formation of

similar fracture features consisting of slip steps superimposed by striations under mixed mode fatigue fracture. Clear striations along with intermetallic particle fracture and an uneven fracture surface could be observed, which can be attributed to the mixed mode crack growth (Figure 3.22d). In the stage III or fast fracture regime, striations and slip steps started to diminish, and the formation of dimples, which are indicative of a static type mode-I dominated tensile failure mode, was observed (Figure 3.22e).
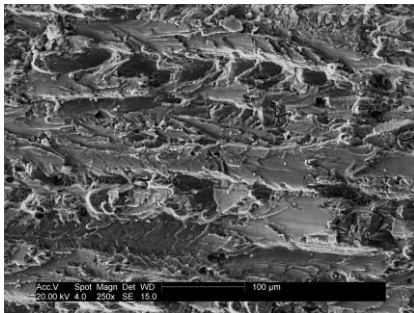
(a) Stage I crack growth; highly torturous crack path, ridges and series of fracture at intermetallic particles
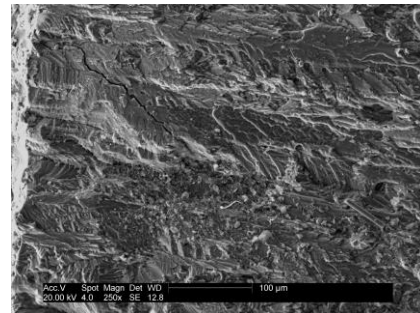
(b) Transgranular cracking and faceted fracture surface
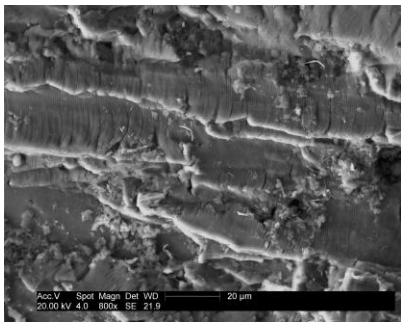
(c) Clear striations superimposed on series of slip steps
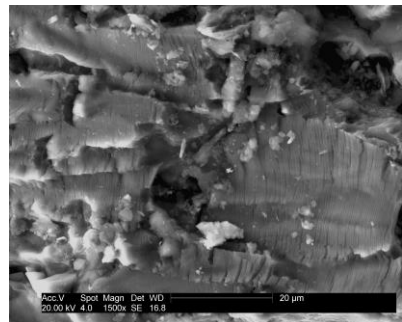
(d) Fatigue striations and sheared intermetallic particles on uneven fracture surface
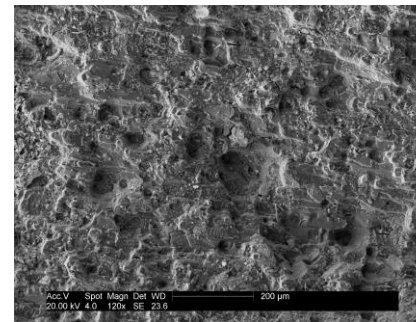
(e) Dimpled fracture surface due to necking around intermetallic particles

Figure 3.22 Crack Growth Behavior for 45° Out-of-phase Loading.

3.5.2.3.3 Crack Length Prediction using Hybrid Prognosis

Since a single crack propagates under a phase difference of 45°, the prognosis methodology used in Section 3.5.2.1.3 was used. Although there was no change in the algorithm, the machine learning component of the algorithm learned the crack growth rate behavior to make accurate predictions. The results of one-step and multi-step ahead predictions starting at the fifth data point are shown in Figure 3.23. The results indicate that the algorithm was capable of making multi-step ahead predictions with high accuracy.

(a) One-step ahead prediction   (b) Multi-step ahead prediction
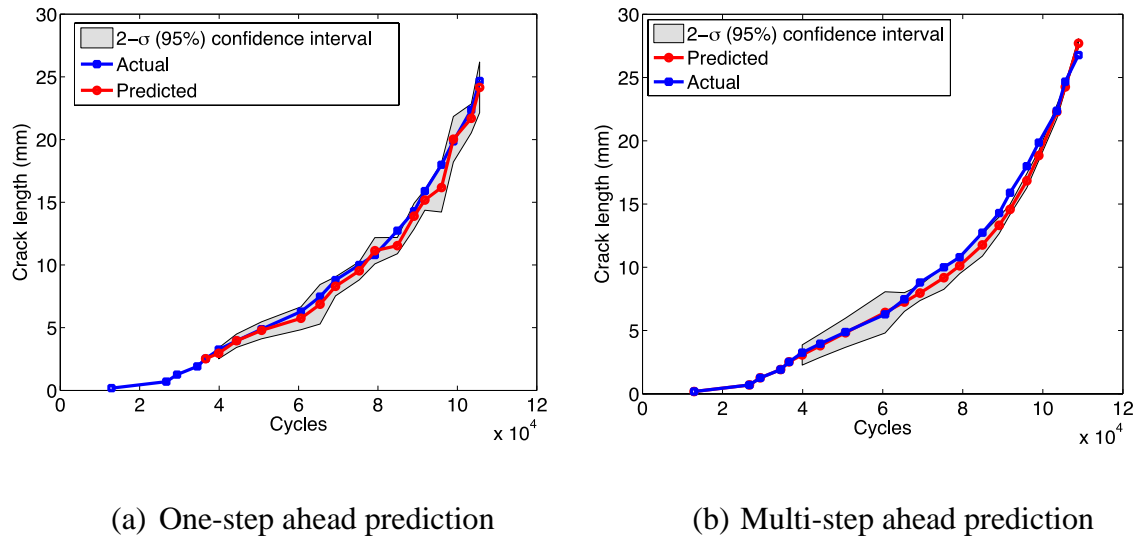
Figure 3.23 Crack Length Prediction under 45° Phase Difference.

3.5.2.4 Phase Difference of 90°

3.5.2.4.1 Experimental Crack Propagation Behavior

When the phase difference was 90°, a single crack initiated and propagated; however, the crack path was not smooth, and blunting of the crack tip along with crack arrest was observed, owing to increased crack closure, as shown in Figure 3.20b. The

111

major crack tended to split into two cracks but only one primary crack propagated, the direction of which was governed by the local microstructure and the mixed mode stress state at the crack tip. Because of the significant influence of K_{II}, the crack flanks slid against each other, which caused increased crack closure in addition to the plasticity induced crack closure from K_{II}. This influence of K_{II} over a part of each fatigue cycle resulted in repeated blunting and deflection of the crack tip, which in turn significantly increased the fatigue life. The plots of crack length and crack growth rate, shown in Figure 3.24, indicate that the crack growth rate was significantly lower (10^{-4}mm/cycle) compared to 45° phase difference. A similar crack retardation phenomenon was observed by Sonsino (2001), when a phase difference of 90° was applied under axial-torsion loading. He concluded that the crack retardation was caused by the small increase of local deformations (plastic ratcheting) when compared to in-phase loading, and that the modified effective equivalent strain hypothesis delivered the closest assessment to the experimental results. Dahlin and Olsson (2006) showed that the presence of mode-II overload cycles decreased the mode-I crack growth rate significantly in compact tension specimens. The mode-I crack growth rate recovered only after the crack length exceeded the plastic zone generated by mode-II loading. Additionally, they observed that the retardation was primarily caused by the tangential displacement of crack-surface irregularities, which induced a surface mismatch between the upper and lower crack faces.
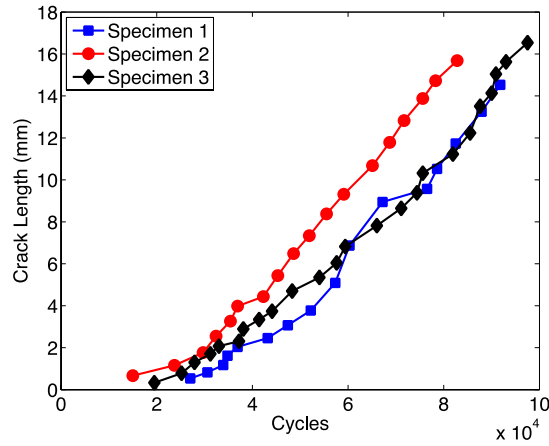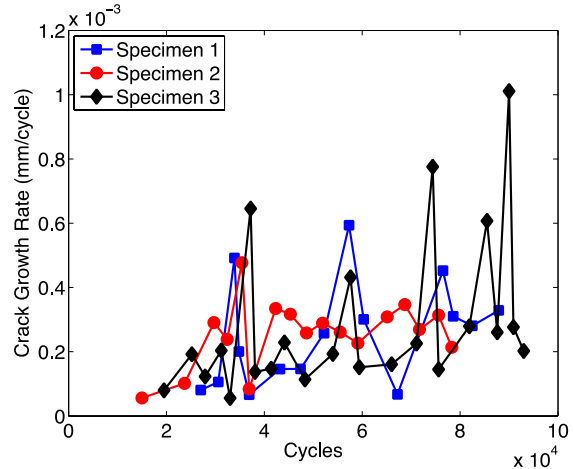
(a) Crack length   (b) Crack growth rate

Figure 3.24 Fatigue Crack Growth under 90° Phase Difference.

3.5.2.4.2 Fractography

The fracture surfaces were analyzed to study the crack retardation behavior, and the microstructural features in the stage II crack growth regime are shown in Figure 3.25. It can be observed from Figure 3.25a that the crack propagation in this regime was dominated by crystallographic fracture, with sharp and angular facets and a highly tortuous crack path. This type of fracture surface can be attributed to the consistently competing mode-I and mode-II crack driving forces. The stage II crack growth regime (Figure 3.25b) exhibited a unique type of crack growth behavior, with negligible fatigue striations as well as abrasion marks and wear debris on the fracture surface. These distinctive fracture features in Stage II regime can be attributed to the significantly higher K_{II} that arose from the 90° phase difference. Since the crack path remained close to the 45° plane of the specimen, the mode-II effects were more prominent. This sliding of crack faces under the influence of mode-II stresses annihilated the striations that led to

the formation of abrasion marks. The fracture feature near the surface of the specimen due to deflection of the crack tip is shown in Figure 3.25c, and the splitting of the crack tip is shown in Figure 3.25d. This was also observed in the camera image of the crack path (shown in Figure 3.20b), where the crack tip tried to split and change direction at many instances, resulting in secondary microcracks and blunting of the primary crack tip. The significantly high fatigue life to failure can also be attributed to the blunting and deflection of the primary crack tip, since the change in direction of the crack path resulted in slower crack growth rates owing to the mitigation of K_I of the primary crack.
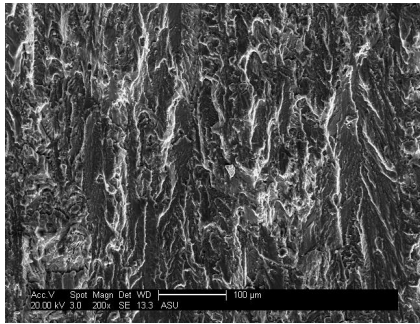
(a) Faint striations
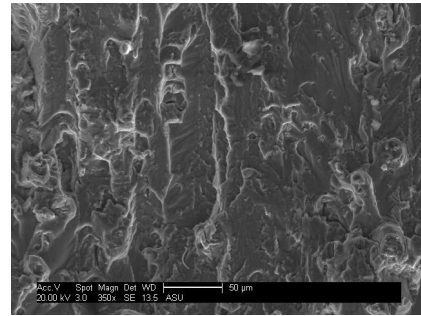
(b) Stage II crack growth
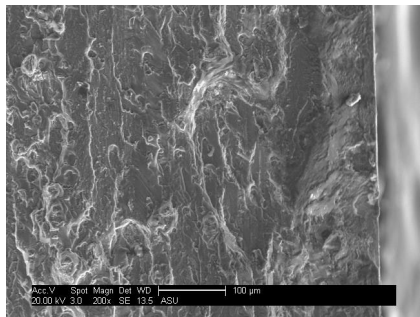
(c) Crack deflection
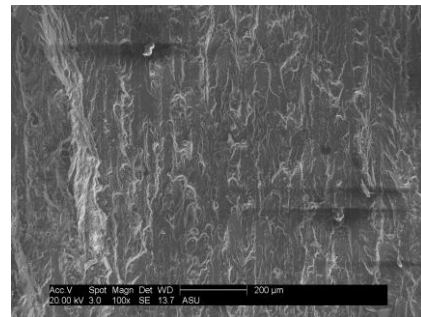
(d) Crack tip splitting due to phase difference

Figure 3.25 Crack Growth Behavior for 90° Out-of-phase Loading.

114

3.5.2.4.3 Crack Length Prediction using Hybrid Prognosis

Since a significant amount of crack retardation was observed under a phase difference of 90°, it is necessary to account for this behavior in the prognosis model. During the initial stages, the crack grew slowly and the growth rate increased after a certain crack length (approximately 10mm). Therefore, this crack retardation data must be included in the prognosis model. The one-step and multi-step ahead predictions starting at the fifth data point are shown in Figure 3.26. Since the training data did not consist of the crack retardation behavior, the error in prediction was large. However, when the predictions started at the 13th data point, the crack length was predicted with high accuracy (Figure 3.27), since the training data consisted of both slow and fast crack growth rates. The experimental data from specimens tested under similar loading conditions can be used to improve the prediction accuracy starting at the fifth data point.

(a) One-step ahead prediction   (b) Multi-step ahead prediction
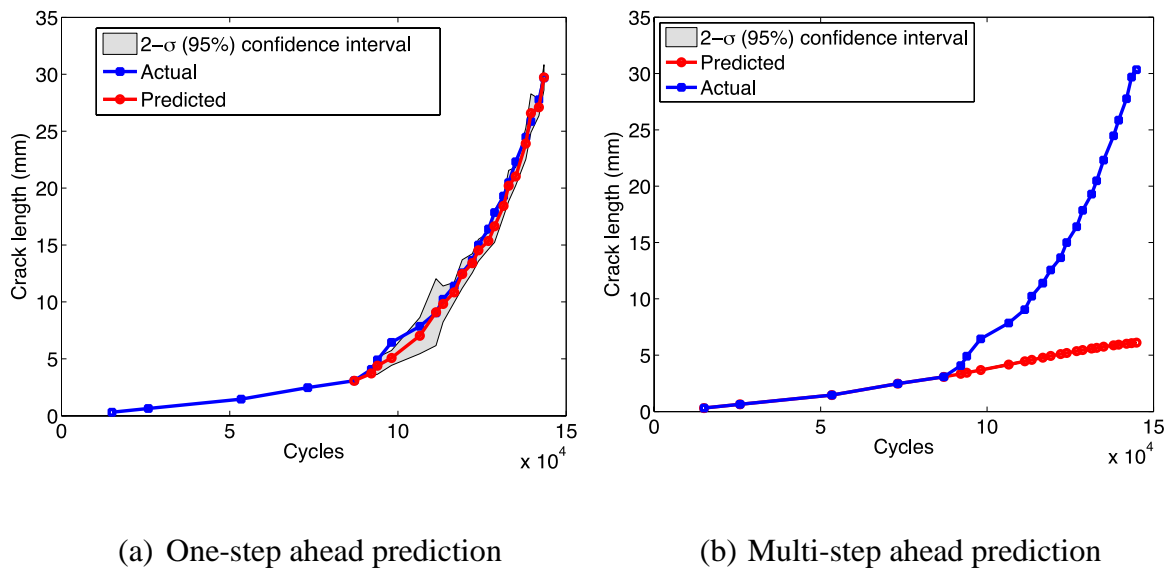
Figure 3.26 Crack Length Prediction Starting at the Fifth Data Point.
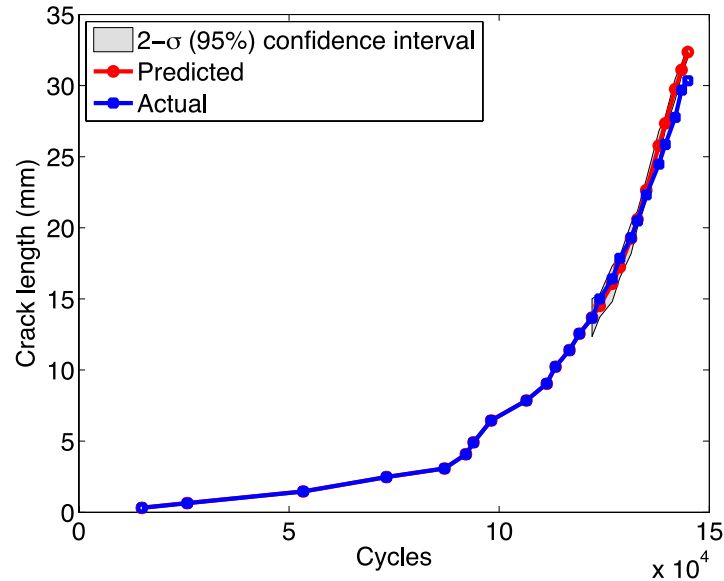
Figure 3.27 Multi-step Ahead Predictions Starting at the 13th Data Point.

3.5.2.5 Phase Difference of 180°

3.5.2.5.1 Experimental Crack Propagation Behavior

For a phase difference of 180°, two cracks initiated and propagated at an angle of approximately 90° to each other, as shown in Figure 3.20c. In addition to the two primary cracks, two secondary cracks formed in opposite directions, similar to the in-phase loading case. The cycles to failure and crack length data (Figure 3.28) shows that the cruciform sample failed faster with 180° phase difference (average = 71064 cycles) than with 90° phase difference (average = 129330) owing to multiple crack propagation; the two cracks resulted in a larger surface area for crack propagation. It was also observed that both cracks propagated at the same rate (10^{-3}mm/cycle) after initiation. The secondary cracks initiated earlier compared to in-phase and 45° and 90° out-of-phase

116

cases. This was due to the very high stress concentrations caused by the opening and closing of the two cracks.
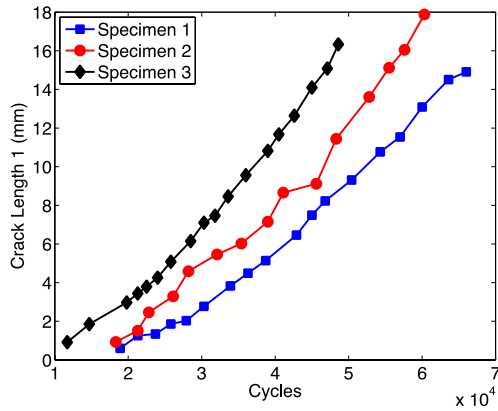
(a) Crack 1
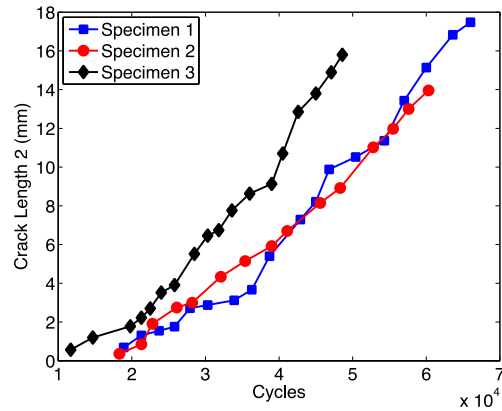
(a) Crack 2
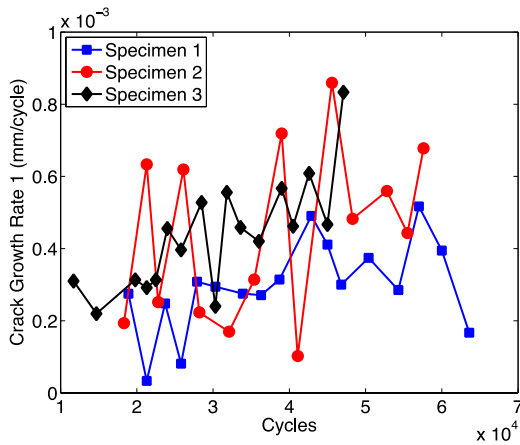
(c) Crack growth rate for crack 1
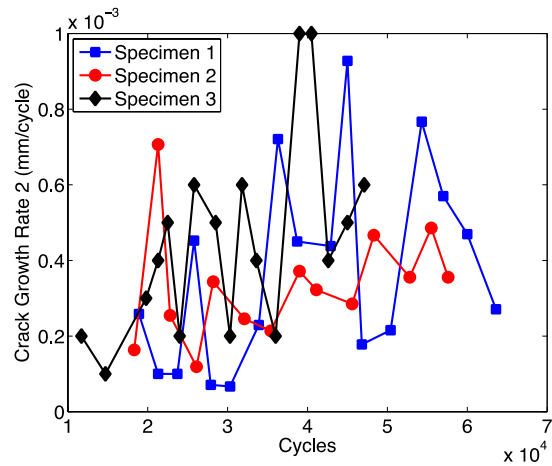
(d) Crack growth rate for crack 2

Figure 3.28 Fatigue Crack Growth under 180° Phase Difference.

When 180° out-of-phase loading was applied at the notch tip, along the 45° plane of the specimen, K_{II} became more dominant over a significant portion of each loading cycle. Therefore, the primary crack split into two cracks immediately after initiation. The two cracks then propagated symmetric to the 45° plane, with an angle of approximately 90° between them. This splitting of the crack into two cracks was recently observed by

Mall and Perel (2015) for in-plane biaxial fatigue tests with 180° phase difference. The orientation of the cracks in this case can be explained using the maximum hoop stress theory (Erdogan & Sih, 1963), which states that the crack tends to propagate in the direction that results in maximum hoop stress at the crack tip, leading to minimization of the K_{II} component of the crack driving force. Erdogan and Sih (1963) derived an equation (Equation 2.20) for angle θ that defines the direction of crack propagation. Hence, two cracks with the same inclination to the initial crack are possible, owing to the symmetric stress state about the initial crack direction.

$$\theta = 2\arctan\left(\frac{1 - \sqrt{1 + 8\left(\frac{K_{II}}{K_I}\right)^2}}{4\frac{K_{II}}{K_I}}\right) \qquad (3.19)$$

3.5.2.5.2 Fractography

The fracture surfaces were studied for both the cracks. Since they were found to have similar features, the fracture surfaces are presented for one of the cracks. In the stage II regime, fatigue striations were observed along multiple slip planes. Unlike in-phase loading, where the deformation behavior in stage II was homogeneous, uneven striations were observed. The morphology of the crack growth with highly angular facets and fatigue striations is shown in Figure 3.29a. Because of the phase difference, the crack experienced mixed mode fracture and exhibited slip steps as well as fatigue striations (Merati et al., 2012), as shown in Figure 3.29b. The superimposition of fatigue striations and slip steps indicated highly mixed mode fracture at the crack tip. Unlike in-phase loading where the striations were relatively uniform, for out-of-phase loading, the

striations were uneven along different crystallographic orientations with slip steps, where narrow and fine striations were observed to be superimposed on one another (Figure 3.29c). It was observed that the stage II crack growth regime lasted much longer than in the case of in-phase loading. The stage III crack growth regime lasted for a relatively short period of time, since most of the crack propagation occurred under stage II.
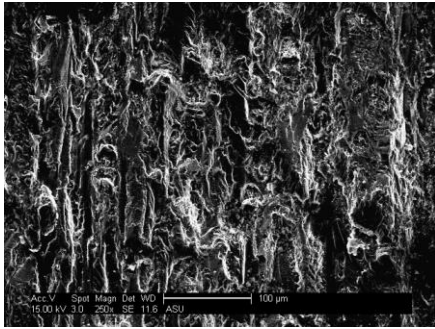
(a) Morphology of stage II crack growth regime, showing highly angular facets and fatigue striations
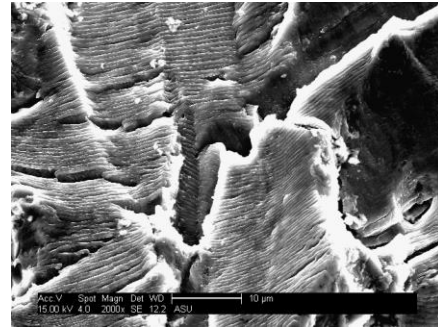
(b) Fatigue striations and slip steps superimposed on one another
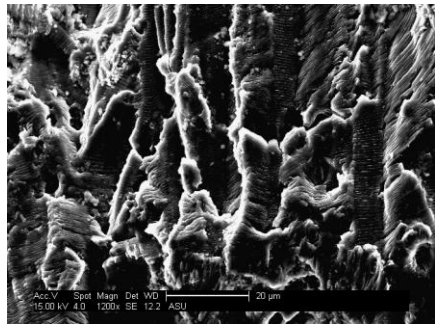
(c) Highly angular fatigue striations
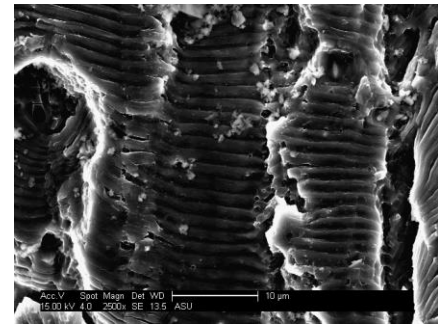
(d) Large striation spacing toward end of stage II

Figure 3.29 Stage II Crack Growth Regime for Crack 1.

3.5.2.5.3 Crack Length Prediction using Hybrid Prognosis

As discussed in Section 3.5.2.5.1, two cracks initiated and propagated simultaneously at an angle of approximately 90° to each other. The energy release rate

119

was expected to be different at each crack tip and to change with the length of each crack; therefore, the finite element model to evaluate G was modified to account for the simultaneous crack propagation. A total of 400 simulations were performed, using six variables: loads in x and y directions and crack tip locations (x, y) for both the cracks. An automated methodology was developed for conducting the large number of FE simulations. Python scripting was used for the finite element simulation, and a combination of MATLAB and Abaqus/Standard was used to generate the python scripts for varying loads and crack tip locations. Using this automated methodology, 400 simulations were conducted in 264 minutes.

The finite element model, the finite element mesh, and the stress contour are shown in Figure 3.30. The red lines in Figure 3.30a show the region in which the crack tip locations were modeled. The horizontal crack is labeled "crack 1" and the vertical crack is labeled "crack 2" in this dissertation. The finite element mesh and the stress contour for crack lengths of 11mm and loads of 15 kN along x and y directions are shown in Figure 3.30b and Figure 3.30c. The stress contour shows that, in addition to the stresses near the crack tip, the stresses at the opposite end of the central hole are high; this is verified by the experimental results showing secondary crack initiations at this location.

(a) FE model   (b) FE mesh   (c) Stress contour
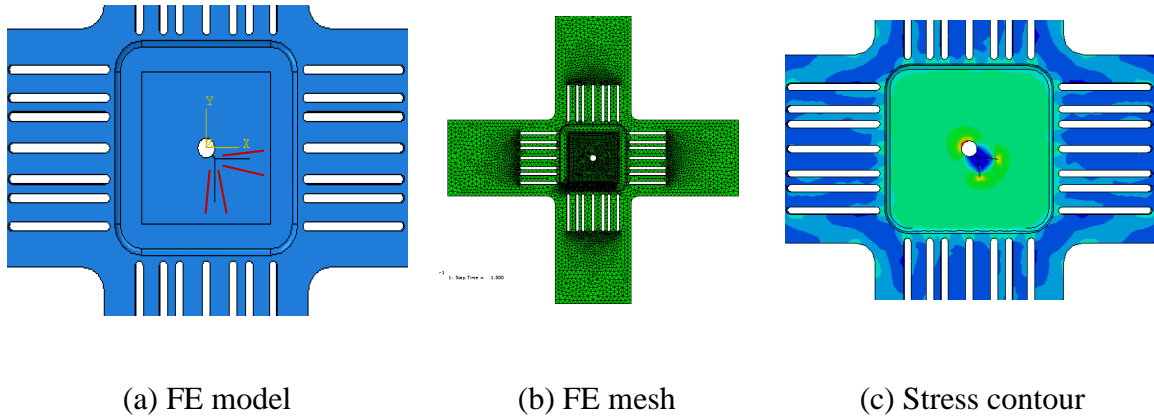
Figure 3.30 Finite Element Model with Two Cracks.

Once the G values were obtained, GP was used to create a multivariate high-dimensional mapping with six input parameters and two output parameters, using Equations 3.14–3.15. The input parameters were the crack tip locations (x, y) for both the cracks and the loads in x and y directions. The output parameters were the G values for both the cracks (G_1 and G_2) evaluated on the grid between the minimum and maximum values of the input parameters with a resolution of 0.01 units. Cross-validation was performed using 350 random samples for training and 50 samples for testing. The coefficient of determination was 0.9716 for G_1 and 0.9974 for G_2, which indicates that the mapping was highly accurate. Since the input data was high-dimensional, the mapping was once again visualized using a series of projections in 3D. Figure 3.31 shows the contour of the mapping as a function of the two crack lengths for a given load of 7.5 kN in both x and y directions. As the length of crack 1 increased, the value of G_1 increased, while the value of G_2 remained almost the same. This is because G_1 was calculated based on the stresses near the tip of crack 1. As the length of crack 2 increased, the value of G_2 increased, while G_1 remained almost constant.

(a) G_1 (b) G_2
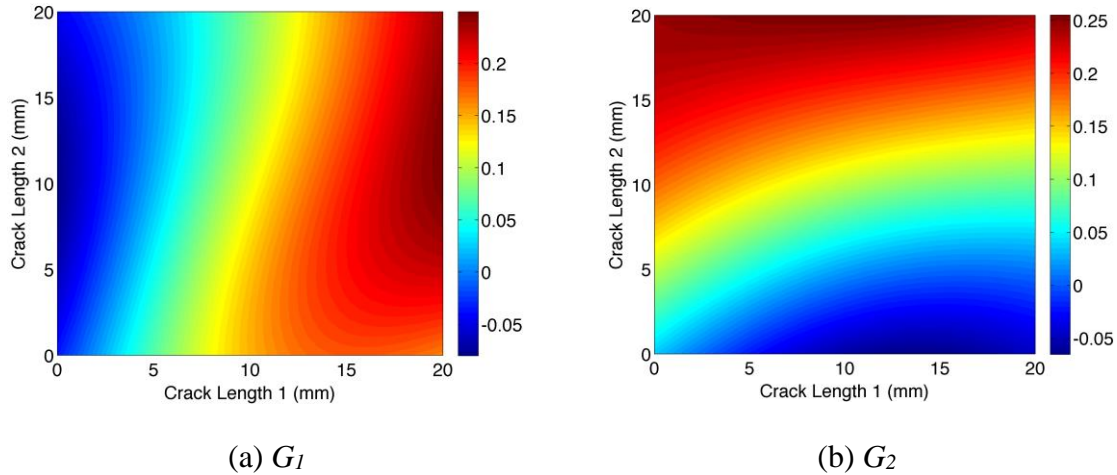
Figure 3.31 G Mapping under Constant Load of 7.5kN in x and y Directions.

     The mapping contour for crack lengths of 17mm and 5mm as a function of the loads in x and y directions is shown in Figure 3.32. As the load in x direction increased, the value of G_1 remained the same because the load was parallel to the crack. As the load in y direction increased, the value of G_1 increased, since the load was perpendicular to the crack. In the case of crack 2, the load in y direction did not change the value of G_2. However, as the load in the x direction increased, the behavior was not linear, since the crack length was much smaller compared to crack 1. The mapping for crack lengths of 5mm and 17mm respectively with varying loads, which exhibit similar behavior, is shown in Figure 3.33.

(a) G_1 (b) G_2
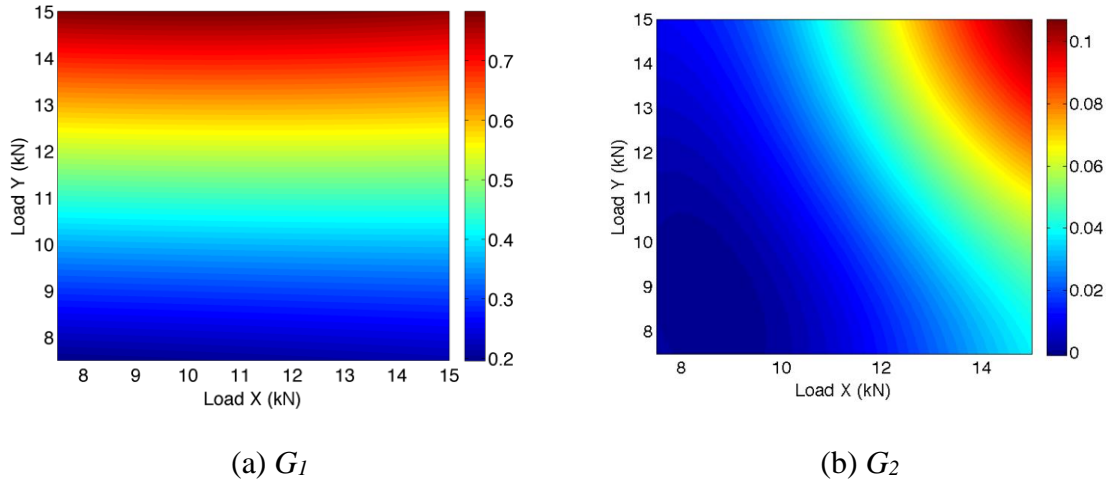
Figure 3.32 G Mapping for Crack Lengths of 17mm and 5mm.

(a) G_1 (b) G_2
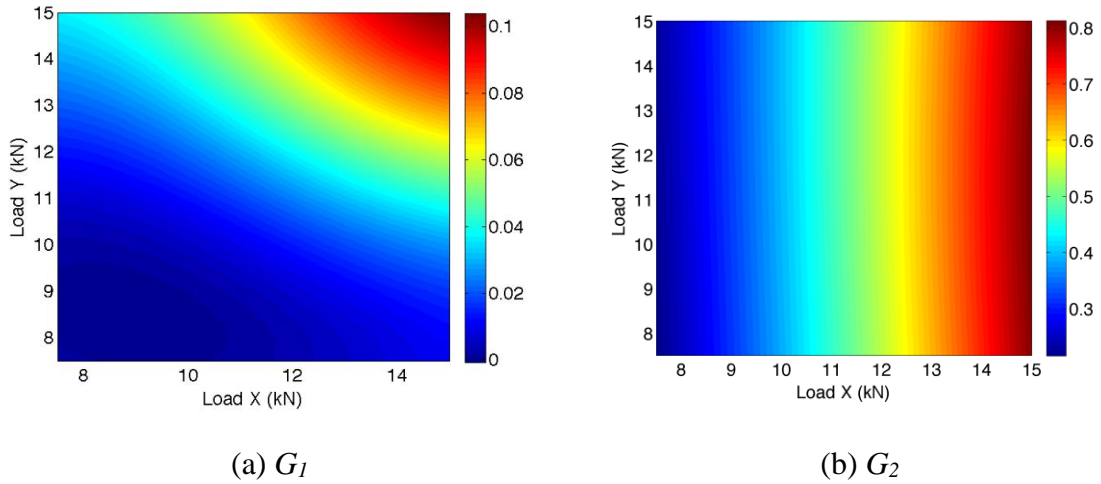
Figure 3.33 G Mapping for Crack Lengths of 5mm and 17mm.

Once the mapping for G was created for different combinations of crack lengths and loads, G was evaluated for any given loading condition and crack length from experiments, using Equations 3.14–3.15. One-step ahead predictions were made for the loads of 1.5–15 kN in both x and y directions with a phase difference of 180°; the results of the predictions are shown in Figure 3.34. The results indicate that the algorithm was

123

able to accurately predict the length of both cracks simultaneously within the 95% confidence interval. Next, multi-step ahead predictions were made for both the cracks, using Equations 3.16–3.18. The results of multi-step ahead predictions for loads of 1.5-15 kN in *x* and *y* directions with a phase difference of 180° starting at the fifth data point are shown in Figure 3.35. The results indicate that the algorithm was able to accurately predict the simultaneous propagation of two cracks.

(a) Crack 1   (b) Crack 2
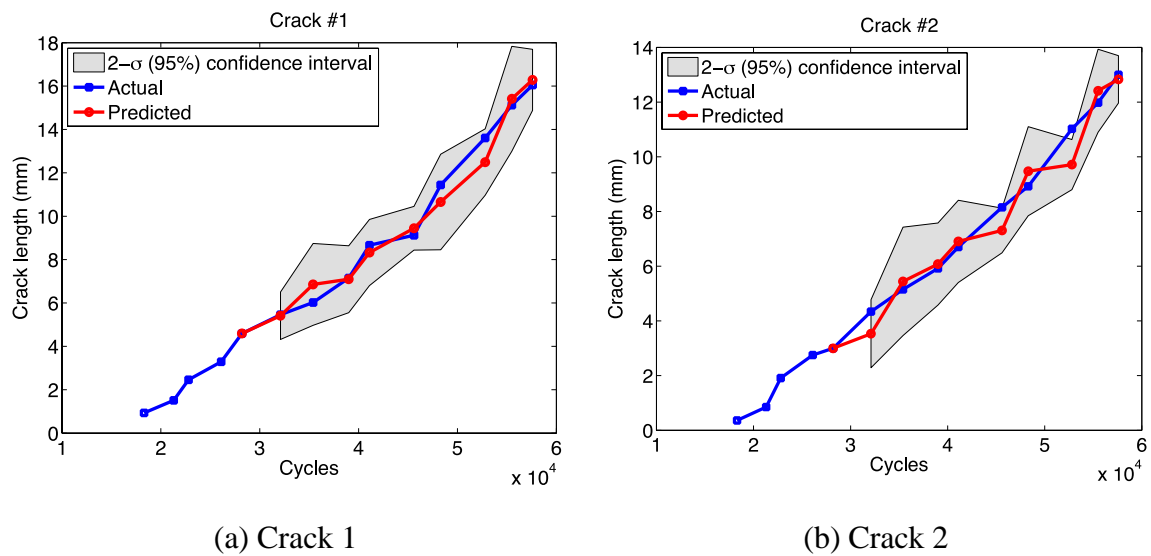
Figure 3.34 One-step Ahead Predictions for Loads of 1.5–15 kN and Phase Difference of

180°.

(a) Crack 1	(b) Crack 2
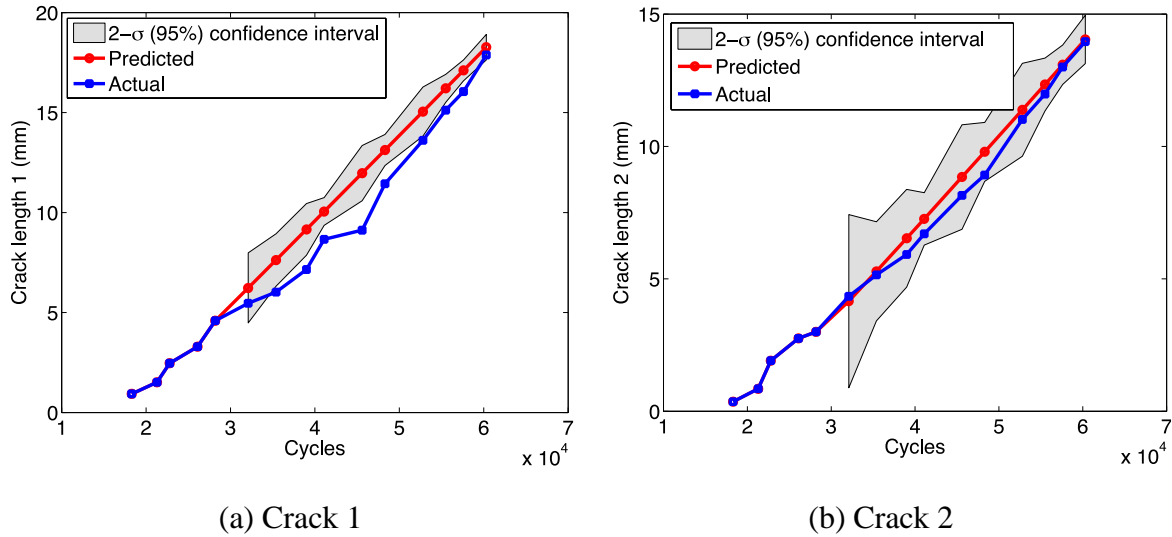
Figure 3.35 Crack Length Prediction for Loads of 1.5–15kN and Phase Difference of

180°.

3.6   Summary

Extensive biaxial quasi-static and fatigue tests were performed to study the crack initiation and propagation behavior under non-proportional, in-phase, and out-of-phase loading conditions. It was observed that a single crack that initiated and propagated under in-phase loading split into two cracks under out-of-phase loading with a phase difference of 180°. For a phase difference of 90°, significant crack retardation was observed owing to mode-II induced plasticity and plastic ratcheting of the crack tip because of the presence of mode-II loading. For a phase difference of 45°, no significant change in fatigue life was observed, since the contribution of mode-II induced plasticity was very low. A comprehensive microstructural characterization was performed to study the crack initiation and propagation behavior. SEM was used to identify the second phase intermetallic particles, and EDS was performed to identify their constituent elements.

125

Two types of intermetallic particles were identified: (i) Fe bearing (hard) and (ii) Si bearing (soft). Fractography was performed on the fracture surface, revealing that the cracks initiated near the hard Fe bearing particles. Nucleation dimples were observed around the hard Fe bearing particles in the stage I crack growth regime. Fatigue striations superimposed on slip steps were observed in the stage II crack growth regime, indicating a highly mixed mode fracture. The stage III crack growth regime showed a large density of dimples resembling static ductile fracture. The fracture surface morphology was highly complex for out-of-phase loading (180°). Although both the cracks showed similar fractographic features, they were highly angular and complex and showed significant mixed mode fracture features. For the 45° out-of-phase loading condition, intermetallic particle fracture and consistent slip steps superimposed with striations were observed throughout the fracture surface, whereas the 90° out-of-phase specimen showed almost negligible striations and signs of crack deflection, which resulted in reduced crack growth rates. A hybrid prognosis model that combines physics based modeling with machine learning was developed to predict the crack propagation under biaxial in-phase and out-of-phase loading conditions. The energy release rate was used as the primary driving force for crack growth. To account for the variability in the crack growth under varying load conditions, high-dimensional mapping was created for the energy release rate as a function of loads and crack tip locations. Gaussian process was used to model the complex nonlinear relationship between energy release rate and crack growth rate. The developed prognosis model is able to accurately make one-step ahead and multi-step ahead predictions of crack propagation under in-phase and out-of-phase loading conditions within 95% confidence intervals for most of the presented cases. The cross-

validation methodology significantly improves the prediction accuracy, even with sparse training data.

4   TEMPORAL SCOUR DEPTH PREDICTION NEAR BRIDGE PIERS

4.1   Introduction

Bridge scour is a highly stochastic process and therefore, a reliable prognostics framework is essential for real-time scour monitoring. This chapter presents a fully probabilistic machine learning-based methodology. First, a Gaussian process (GP) based prognosis model (Gibbs, 1998; MacKay, 2003; Rasmussen and Williams, 2006), which is a probabilistic data-driven approach with Bayesian uncertainty in predicting the time-dependent scour, is presented. Then, an adaptive integrated approach consisting of a GP prognosis model (Neerukatti et al., 2015) coupled with a particle filtering approach (Doucet et al., 2001) in order to take into account the uncertainties in measured and predicted values is presented. The particle filter is a sequential Monte Carlo method, which is a sophisticated model estimation technique and is used to estimate Bayesian models in which the latent variables are connected in a Markov chain, and where the state space of the latent variables is continuous. Particle filters combine the observed measurement and the prediction to give an optimal estimate of the true state of the system (scour depth). This integrated approach is capable of making temporal local scour depth predictions using measurement information. Particle filter methodology is employed to update the true scour depth at each time step based on the measured and predicted scour depth. The measurement model for the particle filter updating scheme is obtained through RFID sensors, which measure the scour depth at a given instant of time. The state space model is the Gaussian process-based prognosis model, which is capable of making predictions for the future.

To validate the proposed methodology, two case scenarios were considered. (i) Case 1: scour depth measurements for the next time instant are available, and (ii) Case 2: scour depth measurements for several time steps are not available. For example, if a system measures the scour depth once every day, the prediction is case 1. If the scour measurements are unavailable for a period of time (for instance, 2 days or more), the prediction is case 2. The time period for these predictions may vary based on different situations. It should be noted that the proposed methodology focuses on predicting the time-dependent scour depth through continuous monitoring, and the emphasis is not placed on scour prediction for design purposes.

4.2   Time-dependent Scour Prediction

Traditionally, bridge scour inspection is performed by Department of Transportation (DOT) engineers either periodically or before and after a major flood (Mueller and Wagner, 2005). The disadvantage of periodical inspection is that the process of sediment refilling the scour hole cannot be captured, which leads to inaccuracy in the measurement of scour depth. This is the primary reason for using the highly conservative HEC-18 equation in bridge design. Continuous scour monitoring provides much more reliable data based on which accurate prediction models can be developed. In addition, the scour phenomenon is highly stochastic in nature and therefore, there is a need to consistently monitor the scour depth and make predictions based on how it evolves over a given period of time. Traditionally, empirical equations are used to predict scour depth. These equations tend to be very conservative in scour prediction (Pal et al.,

129

2011), and, therefore, a reliable decision support system cannot be developed using these estimates. One of the major drawbacks of using these empirical equations is that they do not predict time-dependent scour as they are designed to forecast the maximum possible scour (design value) for a given set of flow conditions. Some soft computing technique-based models (Azamathulla et al., 2008; S. M. Bateni et al., 2007; Firat and Gungor, 2009) for scour prediction do not consider "time" as a parameter in their model, which can result in erroneous results. The disadvantage of using the above-mentioned methods is illustrated using a simple example. For instance, the velocity and flow depth near a bridge pier at a time t_1 are V_1 and h_1, respectively. The scour depth (d_s) predicted using these methods would be d_{s1}. At time t_2, it is assumed that the velocity and flow depth increased to V_2 and h_2, which are greater than V_1 and h_1, respectively. The predicted scour depth would now be d_{s2}, which is greater than d_{s1}. If the velocity and flow depth return to the initial conditions V_1 and h_1, the scour depth using these models would be d_{s1} so it is clear that the scour depth must be greater than or equal to d_{s2}, unless sediments shift to fill the scour hole. Therefore, a model which accounts for the variability of scour depth with respect to time is necessary.

Another important aspect in predicting scour depth is accounting for the uncertainties in both measured and predicted values. This is often the case in field applications, where the scour depth is measured using sensors. Therefore, it is necessary to account for this measurement variability, and combine both measured and predicted values at each time step. In the present work particle filtering will be used for combining these values.

4.3   Radio Frequency IDentification (RFID) Sensing

RFID is a wireless automated identification technology that utilizes radio frequency (RF) waves to transfer information between a reader and a transponder (short for transmitter and responder) via an antenna (Lauth and Papanicolaou, 2008; Papanicolaou et al., 2010). An important feature of RFID technology is that a unique identification number can be assigned to each transponder, allowing different transponders within the system to be identified (Papanicolaou et al., 2010). The system is capable of detecting the orientation of the transponders along with their distance from the antenna based on the signal strength obtained. The main components of the RFID system shown in Figure 4.1 are (i) the antenna, which generates an electromagnetic field, (ii) the reader, which reads the signals, and (iii) the transponders, which reflect the signal from the antenna. RF waves are transferred from a reader through an antenna to the transponders. The transponders are passive in nature and reflect the received RF waves, which are transmitted back to the antenna. The level of degradation in the returned signal is related to the distance between the transponder and antenna.
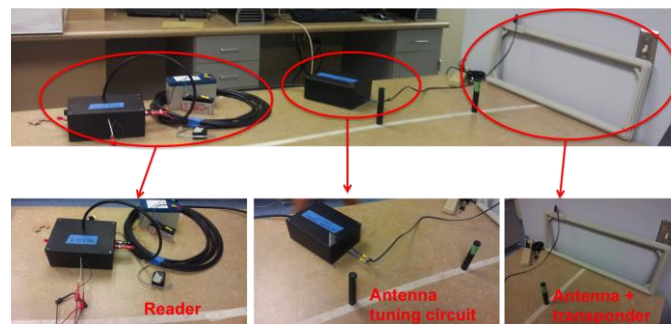
Figure 4.1 RFID System with Components (Texas Instruments Inc.).

The antenna sends waves to each transponder at specific intervals of time and checks the degradation level of the returned signal. The information from all the transponders can be

analyzed to evaluate the scour depth. The maximum signal strength is obtained when the transponder's axis is perpendicular to the antenna. As the axis becomes parallel to the antenna's axis the signal strength decreases. This phenomenon can be used to measure the angle of the transponders with respect to the antenna's axis (Papanicolaou et al., 2010). As the scour occurs, and the exposed transponder starts to rotate, the intensity of the returned signal reduces implying scour hole formation. By analyzing the signal from all the transponders and finding the number of transponders whose axes are parallel to the antenna's axis, the scour hole depth can be estimated considering the change in the level of the signals from the transponders. The advantage of using RFID technology is its capability of transferring scour data online to a central base station, where the prognostic algorithms are used to make predictions.

4.3.1 Field Test

Preliminary field tests were conducted by the University of Iowa at Clear Creek Bridge near Camp Cardinal. Four transponders were buried underwater at different depths and the signal strength decay data was collected. The results indicated that the signal decay was approximately 50% for a distance of 2.75m, and the overall antenna detection range was 5m (Papanicolaou et al., 2010). Further, the robustness of the RFID system for scour detection was examined by installing a prototype of the system (Figure 4.2) at the N Bush Highway Bridge in Arizona. In this field test, the signal strength degradation data was collected. Since there was no scour at the bridge at the time of the field test, the signal strength data was collected from transponders placed at different depths in the riverbed. Figure 4.3 shows the typical RFID sensor data. Data level 1 shows the charging of the transponder. Data level 2 shows the intensity of the returned signal.

132

As the returned signal strength from the transponder decreases, the magnitude of data at level 2 reduces. Data level 3 shows the transponder's synchronization stage.

Figure 4.2 Installing the RFID System Near the Bridge Pier.
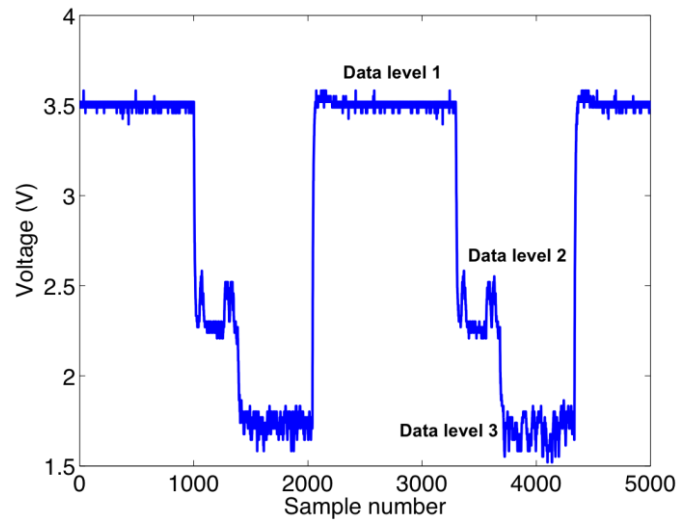
Figure 4.3 Typical RFID Signal.

A smaller antenna (71cm x 27cm) with a detection distance of 1.2m was initially used for the field-testing. Attaining the signal degradation data for different depths in the soil and the water means the scour depth can be estimated. Data was collected from the

transponders while they were buried at different depths in the water and the soil. Figure 4.4 shows the voltage level obtained when the transponder is buried in different media (water, and soil). The curve corresponding to the legend "Water (the large antenna)" reflects the experiments conducted at the University of Iowa. The y-axis in Figure 4.4 shows the percentage decay in the original voltage (when the transponder is 0cm from the antenna). It should be noted that for this particular field test, the variation in voltage was the important factor, rather than the overall detection distance. The signal strength decay in different media was the main goal for the installation of this prototype antenna.
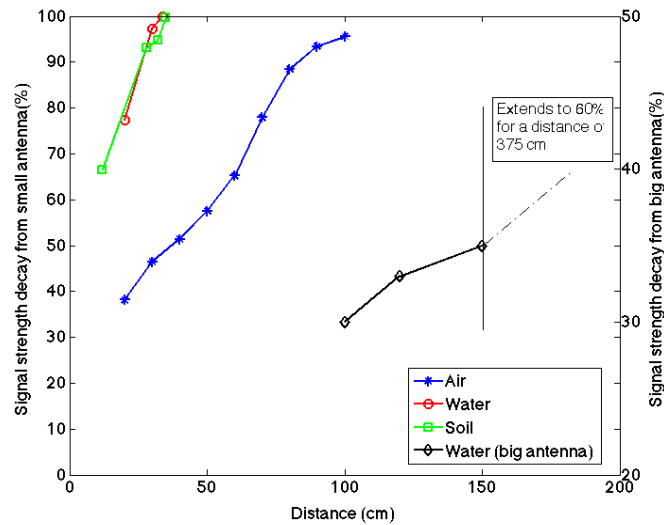
Figure 4.4 Signal Strength Decay in Different Media.

A larger antenna (diameter 1.1m), developed at the adaptive intelligent materials and systems center at Arizona State University, and with a detection range of 9m was built and installed at the New River Bridge in Arizona, as shown in Figure 4.5. Increasing the dimensions of the antenna generates a larger electromagnetic field which increases the sensing distance. Along with the RFID system, a pressure transducer was used to

measure the approach flow depth. The velocity of the flow can be computed from the flow depth by using the Manning equation (Manning et al., 1890). The scour depth collected from the RFID, flow depth, and velocity of the flow at a given instant of time are the input parameters for predicting scour using the proposed prognosis model, which is explained in the next section.
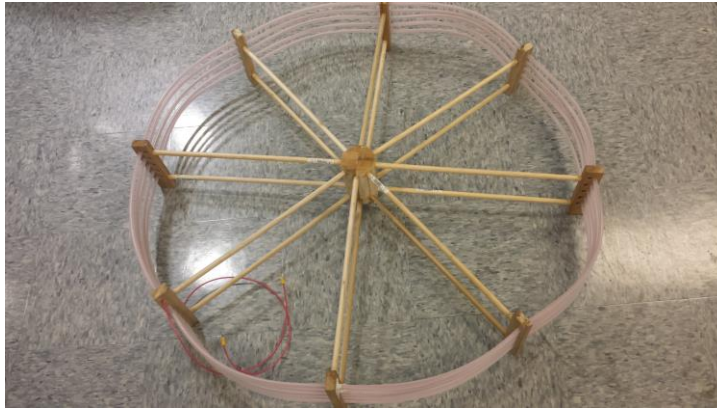
Figure 4.5 Large Size Antenna (diameter 1.1m).

4.4   Parameter Selection and Datasets

The scour depth (d_s) depends on various parameters such as the flow velocity (V), the flow depth (h), the skew (S_k), the pier diameter (D_p), the median particle size (d_{50}), and the gradation (σ) (Mueller and Wagner, 2005). The median particle size (d_{50}) is the diameter at which 50% of the soil particles are smaller than d_{50}, and the gradation is given as d_{84}/d_{50}. The relationship between the scour depth and these parameters can be written as:

$$d_s(t) = f_1(h, V, S_k, D_p, d_{50}, \sigma, t) \tag{4.1}$$

where t is the time. The mechanism of scour evolution changes with the different characteristics of the input parameters. The parameters such as D_p, S_k, d_{50}, and σ are assumed to remain the same in the streambed near the bridge pier. Due to the difficulty in measuring any change in d_{50} during the scouring process, the parameter d_{50} is used as an index to select the proper training data. The gradation (σ) is a function of particle size and will change very little during the lifespan of a bridge structure in a particular streambed. Since the variation of skew with the flow rate could not be explicitly modeled using the Hydraulic Engineering Center's River Analysis System (HEC-RAS) (Brunner, 2001), it is assumed to be constant in this study. Considering these assumptions, the model can be simplified to study the evolution of scour depth for a bridge. The simplified relationship for temporal evolution of scour can be written as:

$$d_s(t) = f_2(h, V, t) \qquad (4.2)$$

Two datasets were used to validate the GP prognosis model:

(i) A laboratory dataset (Melville and Chiew, 1999) that contained 84 data points from experiments conducted in four different flumes. The characteristics of the dataset are shown in Table 4.1. The minimum value of the parameter is x_{min}, the maximum x_{max}, the mean x_{mean}, the standard deviation x_{std}, the variation coefficient C_{vx}, and the skewness coefficient S_x.

(ii) The field dataset available in the bridge scour management system (Mueller and Wagner, 2005) containing 493 pier scour measurements. This dataset has pier scour

136

measurements at 79 different test sites in 17 states in the US. The characteristics of this dataset are shown in Table 4.2.

Table 4.1 Characteristics of the Laboratory Dataset

Variables	x_{min}	x_{max}	x_{mean}	x_{std}	C_{vx}	S_x
D_p (mm)	16	200	85.0075	48.2872	0.568	0.7229
d_{50} (mm)	0.8	7.8	1.9261	1.7819	0.9252	1.9797
h (mm)	20	600	269.7262	210.4478	0.7802	0.7385
V (m/s)	0.165	1.208	0.4251	0.2698	0.6346	1.3352
t (min)	200	15000	3909.3	3096.9	0.7922	1.9316
d_s (mm)	4	318	122.75	88.744	0.723	0.5961

Table 4.2 Characteristics of the Field Dataset

Variables	x_{min}	x_{max}	x_{mean}	x_{std}	C_{vx}	S_x
D_p (mm)	0.9	5.5	1.9152	1.4753	0.7703	1.0905
d_{50} (mm)	0.48	0.74	0.6642	0.0978	0.1473	-1.2947
h (mm)	4.3	15.4	7.0848	3.1021	0.4378	1.3501
V (m/s)	0	2.3	0.8894	0.4766	0.5358	0.5407
t (min)	1	127	33.5	40.5945	1.2118	1.2238
d_s (mm)	0.2	4.6	1.2985	1.3474	1.0377	1.4195

4.5 The Gaussian Process Prognosis Model

A GP model, which includes Bayesian uncertainty, is used for the prediction of the time-dependent scour depth. The GP is a collection of random variables, any finite number of which have consistent Gaussian distributions. It can be considered as a generalization of a multivariate Gaussian distribution to an infinite number of variables. A GP model is used for predicting the time-dependent scour depth. The GP makes predictions by projecting the input space to the output space, through inferring their underlying non-linear relationship (Rasmussen and Williams, 2006). Once the algorithm is trained with the input and output parameters, it can predict the output parameter for unknown or new sets of input parameters. The input space contains the variables flow depth, velocity, and time, and the output space consists of the scour depth. The posterior distribution over the predicted scour depth at time "t", $(d_s)_t$ can be written as:

$$f((d_s)_t|D, \mathbf{K}_{t-1}, \boldsymbol{\theta}) = \frac{1}{Z} exp\left(-\frac{((d_s)_t - \mu_{(d_s)_t})^2}{2\sigma^2_{(d_s)_t}}\right), \tag{4.3}$$

where Z is a normalizing constant, $D = \{\mathbf{x}_i, (d_s)_i\}_{i=1}^{t-1}$ is the training set, K_{t-1} is the kernel matrix, $\boldsymbol{\theta}$ is the set of hyper-parameters (HPs), $\mu_{(d_s)_t}$ is the mean, and $\sigma^2_{(d_s)_t}$ is the variance of the distribution obtained as,

$$\mu_{(\dot{d}_s)_t} = \mathbf{k}_t^T \mathbf{K}_{t-1}^{-1}(d_s)_{t-1}; \sigma^2_{(\dot{d}_s)_t} = \kappa - \mathbf{k}_t^T \mathbf{K}_{t-1}^{-1} \mathbf{k}_t, \tag{4.4}$$

where $(d_s)_{t-1}$ is the (t-1x1) training output vector which consists of the scour rate, and κ, $\mathbf{k}_t$, K_{t-1} are the partitioned components of the t-th instances of the kernel matrix $\mathbf{K}_t$ given by,

$$\kappa = k(\mathbf{x}_t, \mathbf{x}_t);\ K_{i,j} = k(\mathbf{x}_i, \mathbf{x}_j)_{i,j=1,2,\ldots,t\text{-}1};\ \mathbf{k_i} = k(\mathbf{x}_t, \mathbf{x}_i)_{i=1,2,\ldots,t\text{-}1}, \tag{4.5}$$

where $\mathbf{x}_i$ contains the flow depth (h), the velocity (V) and the time (t) at the ith time instant. The kernel function transforms the non-linear parameters to a high dimensional space where they are linearly separable. Although the assumption of Gaussian distribution is made on each variable, the results show that it is a good assumption for this application. It is necessary to verify the effect of using different kernel functions to select the best kernel function for this application. Squared Exponential (SE) and Rational Quadratic (RQ) kernel functions are considered in this study.

The SE kernel is expressed as (Rasmussen and Williams, 2006):

$$k_{se}(\mathbf{x}_i, \mathbf{x}_j) = \theta_1^2 \exp\left(\frac{||\mathbf{x}_i - \mathbf{x}_j||^2}{\theta_2^2}\right), \tag{4.6}$$

where θ_1 and θ_2 are the HPs which govern the accuracy of the predicted values. The RQ kernel has three hyper-parameters and is expressed as (Rasmussen and Williams, 2006):

$$k_{rq}(\mathbf{x}_i, \mathbf{x}_j) = \theta_3^2 \left(1 + \frac{||\mathbf{x}_i - \mathbf{x}_j||}{2\theta_4\theta_5}\right)^{-\theta_4}, \tag{4.7}$$

where θ_3, θ_4 and θ_5 are the HPs. To accurately predict the posterior distribution, the HPs should be optimized to give an accurate hypothesis for the training data. This is accomplished by initializing the HPs to a reasonable value, and finding their optimal values by minimizing the negative log marginal likelihood (L) given by (Rasmussen and Williams, 2006):

$$L = -\frac{1}{2}\log|\boldsymbol{K}_{t-1}| - \frac{1}{2}(\boldsymbol{d_s})_{t-1}^{T}\boldsymbol{K}_{t-1}(\boldsymbol{d_s})_{t-1} - \frac{t-1}{2}log2\pi, \qquad (4.8)$$

The number of parameters in the optimization space influences the initial values of the HPs. If there are two HPs, the initial value does not affect the optimization routine. The following analysis shows that when there are five HPs, they should be initialized between 0.1 and 1. A reasonable value for the HPs in scour problems is recommended to be 0.1 and the data should be normalized. The kernel function is evaluated using the initialized HPs and their optimal values are found by using the conjugate gradient descent optimization algorithm (Hestenes and Stiefel, 1952) by considering "L" as the objective function to be minimized. The training set is updated progressively with time (as new data is available) to (i) improve the accuracy of prediction, and (ii) ensure that the model will be able to capture global and local variations in the parameters. Table 6 shows the details of the kernel functions used, the initialized HPs, the optimal HPs, and the optimal function (L) value. When the SE kernel function is used and the HPs are initialized to (0.1, 0.1), the optimal function value is found to be -43.46. Even if the HPs are initialized to (1,1) and (10,10), the same optimal value for the objective function occurs. With two HPs, the optimization space is 3-dimensional, and the gradient descent algorithm can easily find the optimal descent direction.

The laboratory dataset was chosen to illustrate the effect of different kernel functions on the optimization of HPs. When the sum of both SE and RQ kernel functions is used and all the HPs are initialized to a value of 0.1, an objective function value of -43.46 is achieved, which is almost equal to the value achieved using an SE kernel function. When all the HPs are initialized to a value of 1, the objective function value is -

43.51, which is close to -43.46. But when the HPs are initialized to a value of 10, due to the higher dimensionality, the gradient descent finds a local optima and does not proceed further. Here the optimum function value obtained is +0.0556.

Table 4.3 Initialized HPs and their Optimum Values with Different Kernel Functions

Kernel Function	Initialized HPs (θ)	Optimum HPs (θ_{opt})	Optimum function (L) value
SE	(0.1,0.1)	(-2.09, -2.53)	-43.4612
SE	(1,1)	(-2.09, -2.53)	-43.4612
SE	(10,10)	(-2.09, -2.53)	-43.4612
SE + RQ	(0.1,0.1,0.1,0.1,0.1)	(-0.87, -4.61, -2.05, -2.51, 2.00)	-43.4625
SE + RQ	(1,1,1,1,1)	(-2.04, -2.48, -3.81, -6.34, 0.44)	-43.5141
SE + RQ	(10,10,10,10,10)	(10.02, 9.93, 10.02, 9.98, 10.02)	0.0556

Figure 4.6 shows the number of iterations performed to achieve the optimum value for the scenarios discussed earlier. When the HPs are initialized to (0.1, 0.1) and (1,1) using the SE kernel function, the convergence is obtained in 28 and 29 iterations, respectively. However, when the HPs are initialized to (10, 10) the convergence is obtained after 38 iterations. When the HPs are initialized to (1, 1, 1, 1, 1) using the sum of the SE and RQ kernel functions, the convergence is obtained in 28 iterations. The SE kernel function was found to be successful and was used in the further analysis. It should be noted that the HPs are not constant for a particular scour dataset, and they depend on the outcome of the

141

optimization process. The HPs should be initialized to the value mentioned above, and consequently, the algorithm based on the training sets will automatically calculate the optimum HP values.
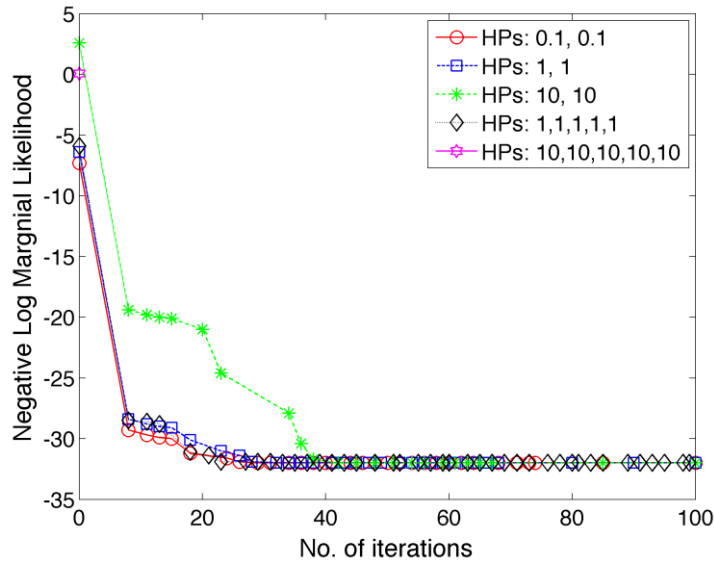
Figure 4.6 HP Optimization with Different Kernel Functions.

4.5.1 Results of Gaussian Process Prognosis Model

4.5.1.1 Laboratory Dataset

The training data was chosen so that the evolution of the scour as a function of time could be predicted. The data was normalized before the analysis to ensure that all the parameters were equally weighted. As the total data was normalized, the HPs in Equation 4.6 were initialized to $\theta_1 = 0.1$, $\theta_2 = 0.1$, and the SE kernel function was used. In all of the following results, the predictions were made at each time step until the next time step at which the measurement was available. Three different cases were selected to show the adaptability and robustness of the developed algorithm. In the first case, the

data from an abrupt change in the scour depth was included. The second case demonstrates the improvement in accuracy of the algorithm with increasing training data. The third case demonstrates the predictive capability of the algorithm under equilibrium scour conditions. Instead of using a fixed set of training and testing data, the training data is dynamically updated with the current measurement after every iteration which enables the usage of more data points for training. This process improves the prediction accuracy because current measurement is always considered before making predictions. Figure 4.7 shows the predicted normalized scour depth and the associated error in prediction as a function of time. The algorithm is able to predict the scour depth accurately within an error of less than 5% for almost the entire scour evolution regime. The error of 8% at the final point of prediction is the result of the limited training dataset. The information about the change after a continuously steady scour depth was not available in the training dataset. However, as more data becomes available regarding the change, the algorithm predicts the scour depth accurately. Figure 4.8 (case 2) shows this phenomenon, where the model is updated dynamically to achieve accurate results. The first prediction is based on three training data points leading to a lower confidence level; however, as the training set is updated by iteration, the error reduces significantly. These results show the algorithm's ability to adapt as it receives more training data.

143
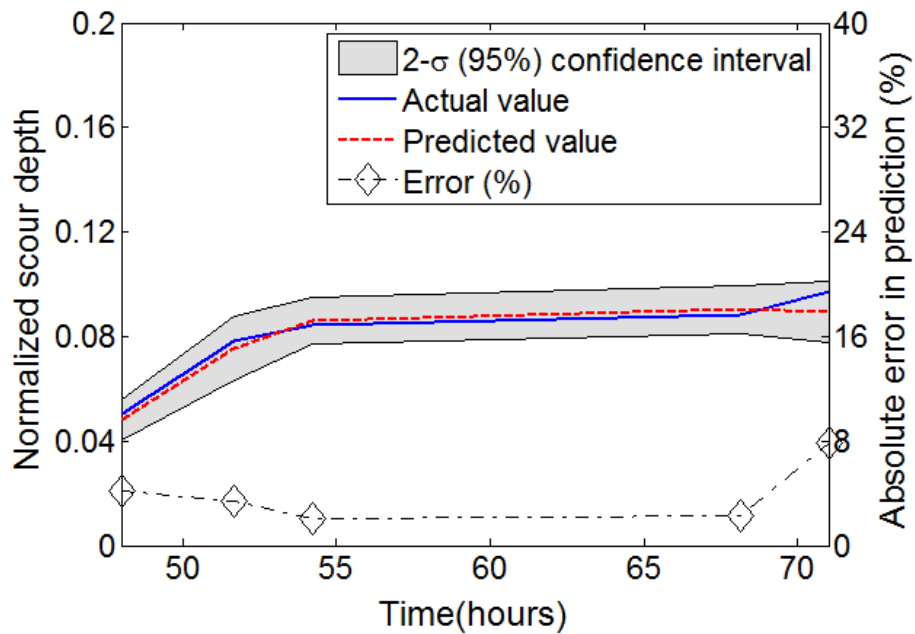
Figure 4.7 Prediction under Insufficient Data about Abrupt Change in Scour Depth (Case 1).

Figure 4.9 (case 3) shows the plot of the predicted scour depth with time in a different flume (Melville et al. 1999). This data was chosen to show the equilibrium scour depth. In this case, the equilibrium scour depth is achieved after 91 hours. Once it is achieved, the scour remains almost constant and does not change with the input parameters. Figure 4.9 shows the capability of the algorithm of capturing this phenomenon. During the equilibrium phase, the error in prediction is less than 2%.
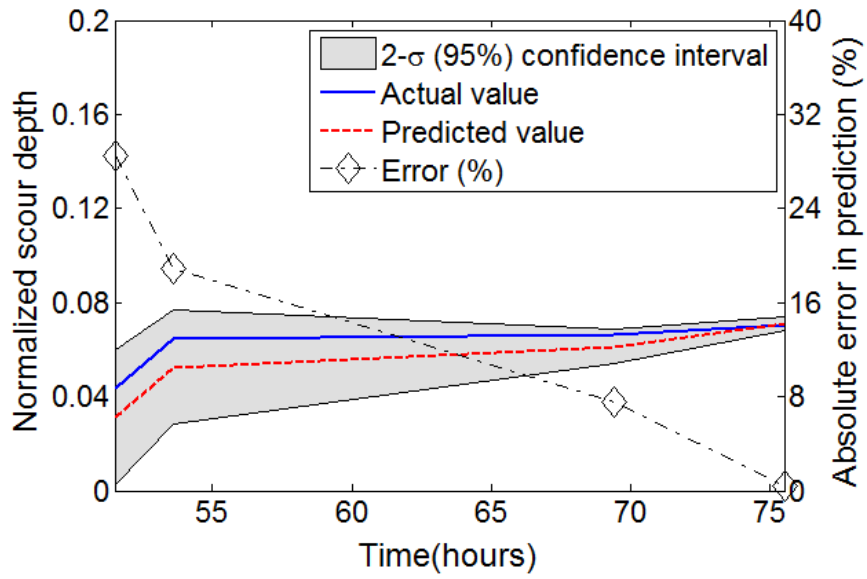
Figure 4.8 Prediction with Increasing Training Data (Case 2).
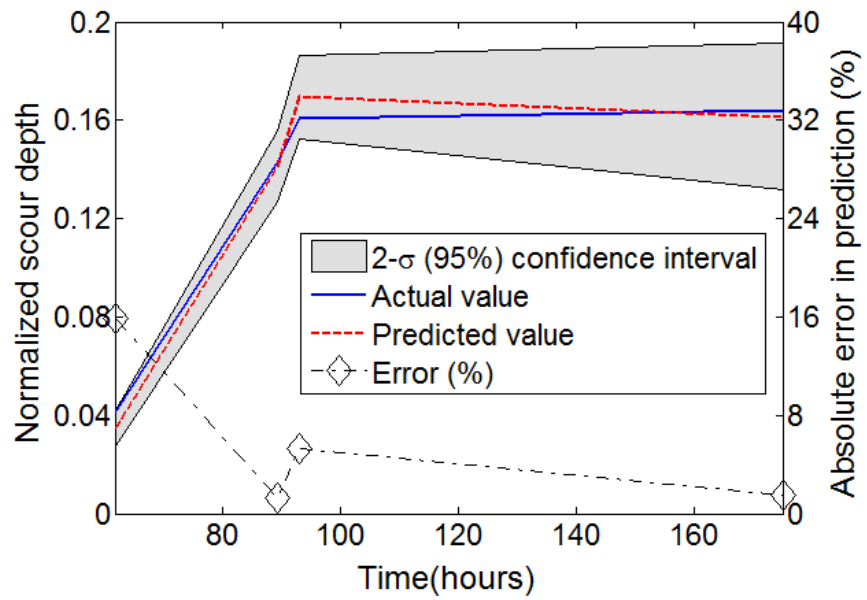
Figure 4.9 Prediction under Equilibrium Scour Conditions (Case 3).

The above three cases show the adaptability and robustness of the GP algorithm under different conditions. Figure 4.10 shows the plot of the actual versus predicted scour for the complete dataset. Out of the 84 points in the dataset, the 27 points that were chosen from different flumes under different flow conditions were used for prediction. The results show that almost 50% of the points are predicted to have an error of less than 5% even with limited training data points, unlike other deterministic regression methods (Pal et al., 2011).
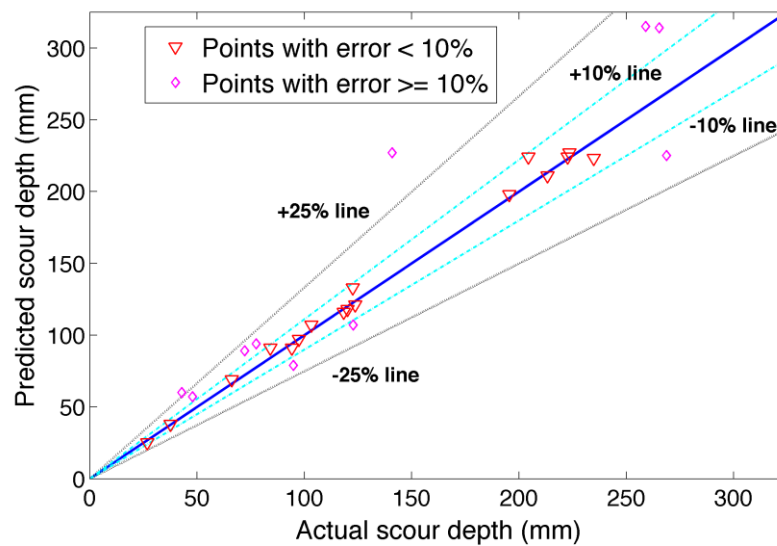
Figure 4.10 Actual Scour vs. Predicted Scour for Laboratory Dataset.

In this dataset, 92.5% of the points are predicted with an error of less than or equal to 25%. Points which had an error between 10% and 25% are the points that had the least amount of training data (≤ 4 training data points). A coefficient of determination of 0.9821 was achieved for the training set and a value of 0.9016 was achieved for the test data.

4.5.1.2 Field Dataset

Out of the 493 pier scour measurements available in the bridge scour data management system (Mueller and Wagner, 2005), 66 data points were carefully chosen for further analysis. These were selected based on the availability of continuous time scour data. Out of the 79 test sites, only 9 sites had frequent continuous time scour data, which could be used for the analysis. Those bridges, whose data was collected approximately every month, were used for the analysis. The 66 data points were collected in different locations under different flow conditions to ensure variability in the parameters. Of the 66 data points, 30 points were used to test the algorithm.

Figure 4.11 shows the prediction of time-dependent scour for a bridge in Montana (Mueller et al. 2005). The pier at which the scour measurements were made is a square pier. The bed material was non-cohesive and the effect of debris was insignificant. The GP algorithm is able to predict the scour depth with an error of less than 10%. The algorithm was then examined for a bridge with round piers located in Virginia. The bed-material and the debris effect were unknown for this location. The time-dependent scour data was available for a period of 120 days. Figure 4.12 shows the prediction of the scour over time. The scour depth is predicted within an error of less than 15% for most of the time regime. The next dataset was chosen so that it shows a continuous increase and decrease of scour depth with time. The third bridge is located in Virginia and the bed material and debris effects were unknown. Figure 4.13 shows the prediction under these conditions. The algorithm is able to capture the trend of increasing and decreasing scour depth with an error of less than 25% for the majority of the time regime.

147
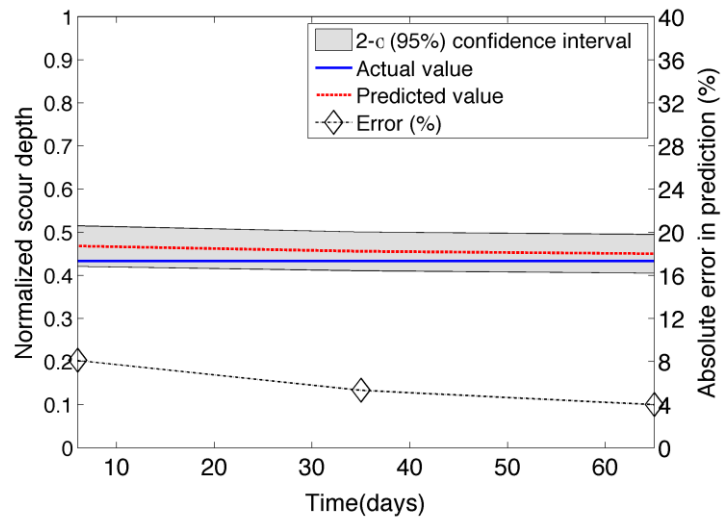
Figure 4.11 Scour Depth Prediction with Non-cohesive Soil and Insignificant Debris .
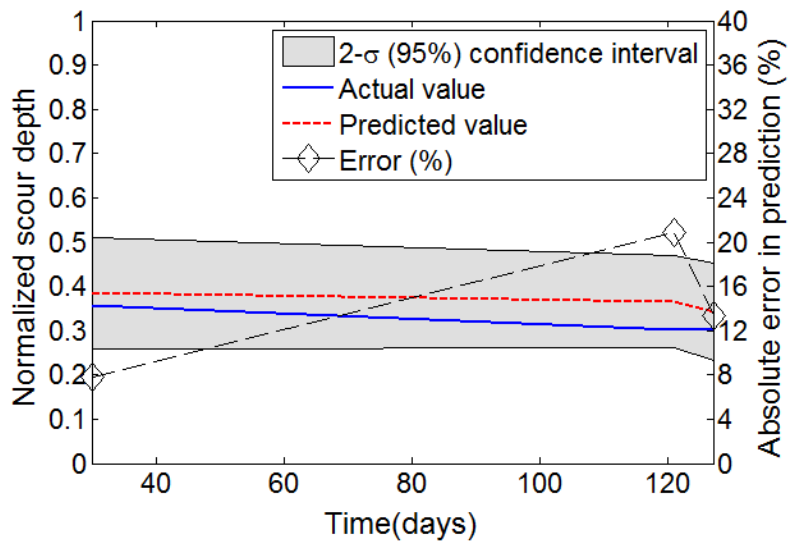
Figure 4.12 Scour Depth Prediction with Unknown Soil Type.

148
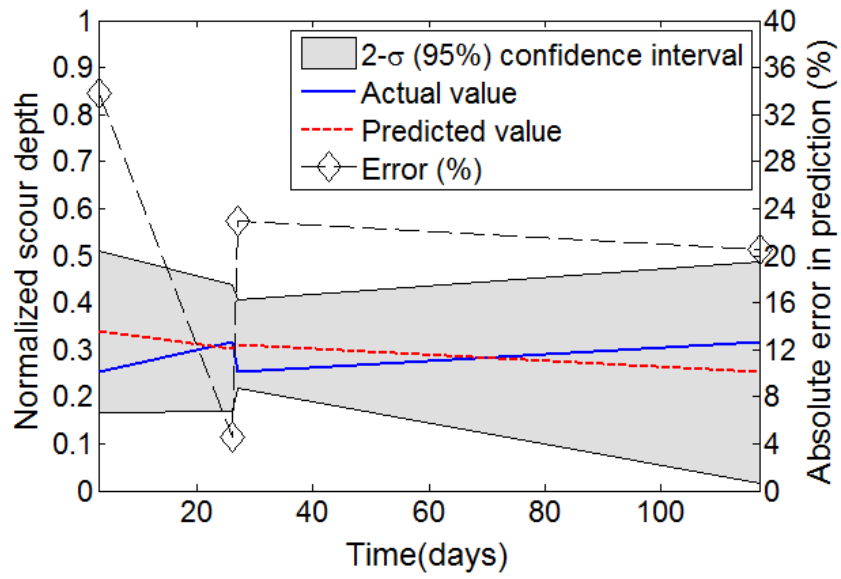
Figure 4.13 Continually Varying Scour Depth Prediction.
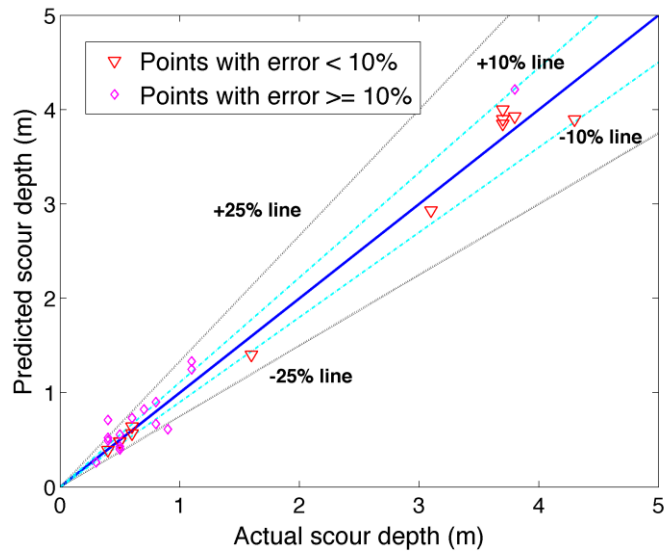
Figure 4.14 Actual Scour vs. Predicted Scour for Field Dataset.

Figure 4.14 shows the plot of actual scour depth versus the predicted scour depth for the complete dataset. All the predicted scour depths, except two, lie in-between the $\pm$25% lines. In all the above cases, the predictions were made with a very limited training dataset. The algorithm is able to predict the scour depth with an error of less than 25% for most of the cases. The results show that the developed prognosis model is capable of predicting the scour depth accurately in both laboratory and field conditions. In this model, measurement uncertainty has not been considered and the measured scour depth is assumed to be the true scour depth, which may not always be true due to the practical inaccuracies in scour depth measurement. In the next section, an adaptive integrated method which combines the GP prognosis model with the particle filtering approach to consider both the measurement and prediction uncertainties for accurate scour depth predictions under real field conditions is developed.

4.6   Adaptive Integrated Prognosis Model

In this section, an integrated approach consisting of the GP prognosis model and the particle filtering approach is developed. Two datasets were used to validate the proposed integrated approach:

i)   A laboratory dataset (Hong et al. 2012) consisting of 417 data points from experiments conducted under different flow conditions.

ii)   A synthetic dataset, which was generated based on HEC-RAS (HEC-RAS 2002) simulations and data from literature (Briaud et al. 1999). The details on how this dataset was generated are presented in the next section.

4.6.1 Synthetic Data Generation

The primary reason for using synthetic data for validation of the proposed model is that there is no continuous field data available in the literature. One of the comprehensive databases for scour data in field conditions is available in the bridge scour database report (Mueller and Wagner, 2005). The time interval between two successive data points in this report varies from one month to twelve months. Therefore, there is no information about the flow conditions during the time steps. The scour depth is also measured only after an event, and thus the flow conditions that caused the scour are not known. As the present method is focused on the time-dependent prediction of scour depth, a synthetic dataset, which has continuous flow conditions is crucial.

The parameters required for the simulation are V, h, t, $d_s(t)$ and $\dot{d}_s(t)$. The particle filtering approach uses the scour rate $\dot{d}_s(t)$ to propagate and update the scour depth. More details on the particle filtering approach will be discussed in section 4.6.2.2. Two Hassayampa Bridges at I-10 in Arizona were selected to perform the simulations. The decision to choose these bridges was made due to the fact that according to the local DOT records, they were among the very few bridges that flood in Arizona. The time-dependent scour was not explicitly modeled using HEC-RAS; the software was only used to obtain the relationship between the velocities and flow depth. Unsteady multi-flow profile simulations were run on HEC-RAS software to capture the velocity for different flow depths along various cross sections of the river channel. The analysis was carried out for two bridges in the reach of the Hassayampa River. The velocity and flow depth were calculated both upstream and downstream of the pier, and their relationship was studied. The first bridge was the I-10 westbound bridge. The distance between the

upstream and downstream stations where *V* & *h* were calculated is 14.2m. The second bridge is the railroad bridge and the distance between the upstream and downstream stations is 5.6m. These two bridges are 50km apart. The relationship between *V* & *h* both upstream and downstream of the pier for both the bridges is shown in Figure 4.15. This figure shows that the relationship between *V* & *h* is almost linear. The result was used to generate synthetic data for *V* & *h*.
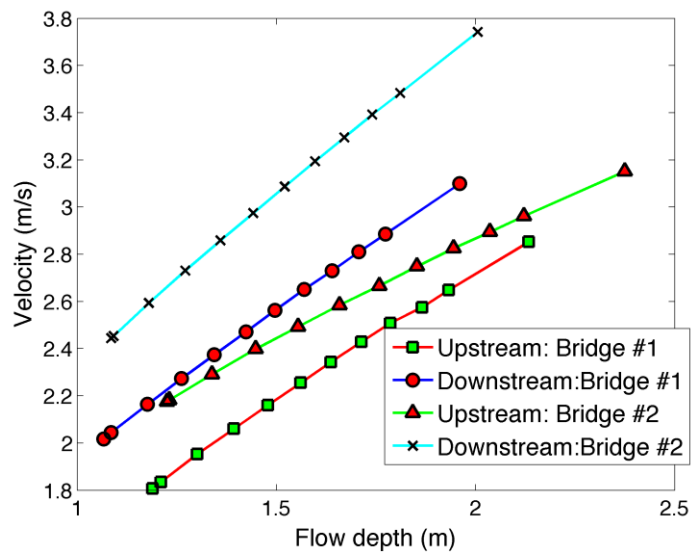
Figure 4.15 Velocity vs. Flow Depth.
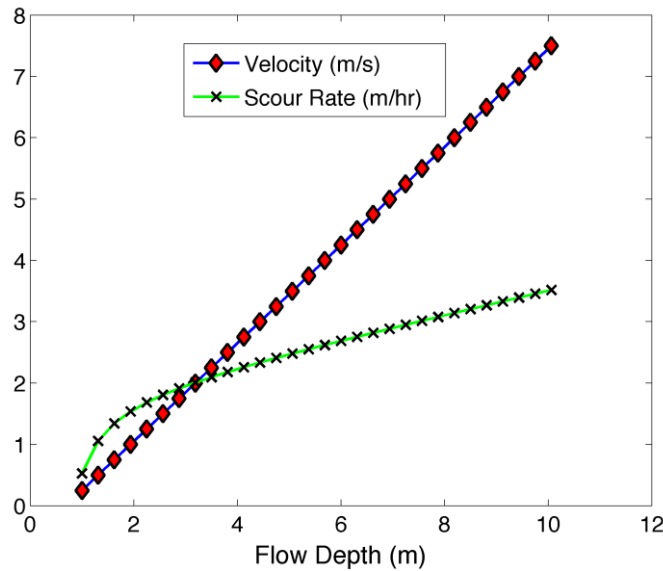
Figure 4.16 Velocity and Scour Rate vs. Flow Depth.

Figure 4.15 shows that the relationship between *V* & *h* is almost linear. This result was used to generate synthetic data for *V* & *h*. Next, the relationship between the scour rate and the flow depth was studied. Briaud et al. (Briaud et al., 1999) examined how the scour rate changes with the shear stress for different kinds of soil, and found that the curve is non-linear. This result, combined with the fact that the shear stress on the riverbed grows with increasing flow depth and velocity, was used to model the relationship between the scour rate and the flow depth as shown in Figure 4.16.

4.6.2 Integrated Approach

4.6.2.1 The Gaussian Process Prognosis Model

The integrated prognostic method proposed in this dissertation optimally combines the measurement model with the Gaussian process-based adaptive prognosis model in a sequential Bayesian framework. Specifically, particle filtering (Doucet et al.,

2001) is used to adaptively predict the scour depth by combining the likelihood function obtained from the measurement model with the predicted distribution from the prognosis model. In this framework, the measurement model is generalized and can be obtained through any of the existing methods such as using RFID sensors (Papanicolaou et al. 2010). The scour rate is assumed to be a random variable that follows Gaussian distribution. Instead of predicting the scour depth, the GP model predicts the scour depth rate for making predictions of the scour depth. Previous studies (Neerukatti et al., 2014a, 2013) showed that the scour depth can be accurately predicted by assuming a Gaussian distribution.

The posterior distribution over the predicted scour rate ($\dot{d}_s$) at time "t" can be written as:

$$f\left(\left(\dot{d}_s\right)_t \middle| \boldsymbol{D}, \mathbf{K_{t-1}}, \boldsymbol{\theta}\right) = \frac{1}{Z} exp\left(-\frac{((\dot{d}_s)_t - \mu_{(\dot{d}_s)_t})^2}{2\sigma^2_{(\dot{d}_s)_t}}\right), \tag{4.9}$$

where Z is a normalizing constant, $\boldsymbol{D} = \left\{\mathbf{x}_i, (\dot{d}_s)_i\right\}_{i=1}^{t-1}$ is the training set, K_{t-1} is the kernel matrix, $\boldsymbol{\theta}$ is the set of hyper-parameters (HPs), $\mu_{(\dot{d}_s)_t}$ is the mean, and $\sigma^2_{(\dot{d}_s)_t}$ is the variance of the distribution obtained as,

$$\mu_{(\dot{d}_s)_t} = \mathbf{k}_t^T \mathbf{K}_{t-1}^{-1}(\dot{\boldsymbol{d}}_s)_{t-1}; \sigma^2_{(\dot{d}_s)_t} = \kappa - \mathbf{k}_t^T \mathbf{K}_{t-1}^{-1}\mathbf{k}_t, \tag{4.10}$$

where $(\dot{\boldsymbol{d}}_s)_{t-1}$ is the (t-1x1) training output vector which consists of the scour rate, and κ, $\mathbf{k}_t$, $\mathbf{K}_{t-1}$ are the partitioned components of the t-th instances of the kernel matrix $\mathbf{K}_t$ given by,

$$\kappa = k(\mathbf{x}_t, \mathbf{x}_t); \; K_{i,j} = k(\mathbf{x}_i, \mathbf{x}_j)_{i,j=1,2,...,t-1}; \; \mathbf{k_i} = k(\mathbf{x}_t, \mathbf{x}_i)_{i=1,2,...,t-1}, \qquad (4.11)$$

where $\mathbf{x}_i$ contains the flow depth (h), velocity (V) and time (t) at the ith time instant. The kernel function transfers the non-linear parameter function to a high dimensional space where the data is easily separable. In this study, a squared exponential kernel function has been used, as it was found to predict scour depth accurately (Neerukatti et al., 2014a). To make accurate predictions for the posterior distribution, the HPs should be optimized to give an accurate hypothesis for the training data. This has been accomplished by initializing the HPs to a reasonable value, and finding their optimal values by minimizing the negative log marginal likelihood (L) given by:

$$L = -\frac{1}{2}\log|K_{t-1}| - \frac{1}{2}\big(\dot{d}_s\big)_{t-1}^{T} K_{t-1}\big(\dot{d}_s\big)_{t-1} - \frac{t-1}{2}\log 2\pi, \qquad (4.12)$$

A conjugate gradient descent optimization algorithm (Hestenes and Stiefel 1952) has been used in this study to minimize L.

4.6.2.2 Integrating the Gaussian Process with Particle Filters

The integrated prognostic method proposed in this dissertation optimally combines the measurement model (RFID signal data) with the Gaussian process-based adaptive prognosis model in a sequential Bayesian framework. Although the GP can be used to model spatio-temporal phenomena and make predictions, it does not take into account the measurement uncertainties. Large measurement uncertainties may lead to inaccurate predictions. Therefore, particle filtering (Doucet et al., 2001; Neerukatti et al., 2015; Zhou et al., 2009) was used to adaptively predict the scour depth by combining the likelihood function obtained from the measurement model with the predicted distribution

from the prognosis model. The particle filtering approach has been proven to be effective in stochastically combining complex prognosis models with measurement models (Neerukatti et al., 2015). The measurement model was obtained by adding Gaussian noise to the actual scour depth to simulate RFID sensor data. The scour rate was calculated using Equation 4.9, and the increment in scour depth and the scour depth at the next time step was calculated as:

$$\Delta(d_s)_t = (\dot{d}_s)_t * \Delta t + \epsilon_p; (d_s)_{t+\Delta t} = (d_s)_t + \Delta(d_s)_t, \tag{4.13}$$

where ϵ_p is the normally distributed process noise which arises due to the uncertainty in the prediction of the scour rate (Equation 4.9). Equations 4.9-4.13 define the Markovian state dynamics model used for predicting scour depth with particle filters. It should be noted that the scour rate in Equation 4.13 is calculated using Equation 4.9 which has the training set (D) and HPs. The measurement model for scour depth was generated by adding Gaussian noise to the actual scour depth as:

$$(\boldsymbol{d_s})_{measured} = (\boldsymbol{d_s})_{actual} + \boldsymbol{\varepsilon}, \tag{4.14}$$

where $\boldsymbol{\varepsilon}$ is the Gaussian white noise. The uncertainty in the measured scour depth arises from the uncertainty associated with the detection capabilities of the RFID system, which is assumed to be normally distributed. Given the probabilistic scour evolution and measurement models, the scour depth can be optimally estimated in a sequential Bayesian framework using stochastic filtering. The particle filter estimates the posterior distribution of the state variables in a sequential Bayesian framework by representing the distributions using particles ($d_s^{(k)}$) and weights ($w^{(k)}$) (Corbetta et al., 2014). The particle

filter is utilized to integrate information from the Gaussian process-based prognosis (state dynamics) model and the measurement model to adaptively estimate the scour depth. The sequential Bayesian framework for iteratively computing the posterior distribution on the scour depth $p((d_s)_t|(d_s)_{1:t,measured}$ can be written as (Zhou et al. 2009; Neerukatti et al. 2015):

$$p((d_s)_t|(d_s)_{1:t,measured} \propto p((d_s)_{t,measured}|(d_s)_t)$$

$$\text{x} \int p((d_s)_t|(d_s)_{t-1})p((d_s)_{t-1}|(d_s)_{1:t-1,measured})d((d_s)_{t-1}),$$

(4.15)

where p(.|.) is the conditional probability distribution. The particle filter representation of the posterior probability distribution is an approximation using particles $(d_s)_t^{(k)}$ and associated weights $w_t^{(k)}$, given by

$$p\left((d_s)_t\middle|(d_s)_{t,measured}\right) = \sum_{k=1}^{M} w_t^{(k)}\delta((d_s)_t - (d_s)_t^{(k)}),$$

(4.16)

where M is the number of particles and δ (.) is the Dirac delta function. At each time step particles are sampled from the importance distribution and the weights are updated using the measurement likelihood (bootstrap particle filter). Resampling is performed using Gaussian distribution to avoid the problem of degeneracy, which occurs when most of the weights are close to zero (Arulampalam et al., 2002). The weights of the resampled particles are then normalized so that they sum one. The scour depth $(d_s)_t$ given $(d_s)_{t,measured}$, is then computed as the expected value of the estimated posterior as:

$$\left(\widehat{d_s}\right)_t = E\left[(d_s)_t\middle|(d_s)_{t,measured}\right] \approx \sum_{k=1}^{M} w_t^{(k)}(d_s)_t^{(k)},$$

(4.17)

where $\left(\widehat{d_s}\right)_t$ is the estimated scour depth and E[.|.] is the expected value. The flowchart of the integrated approach along with the equations is shown in Figure 4.17.
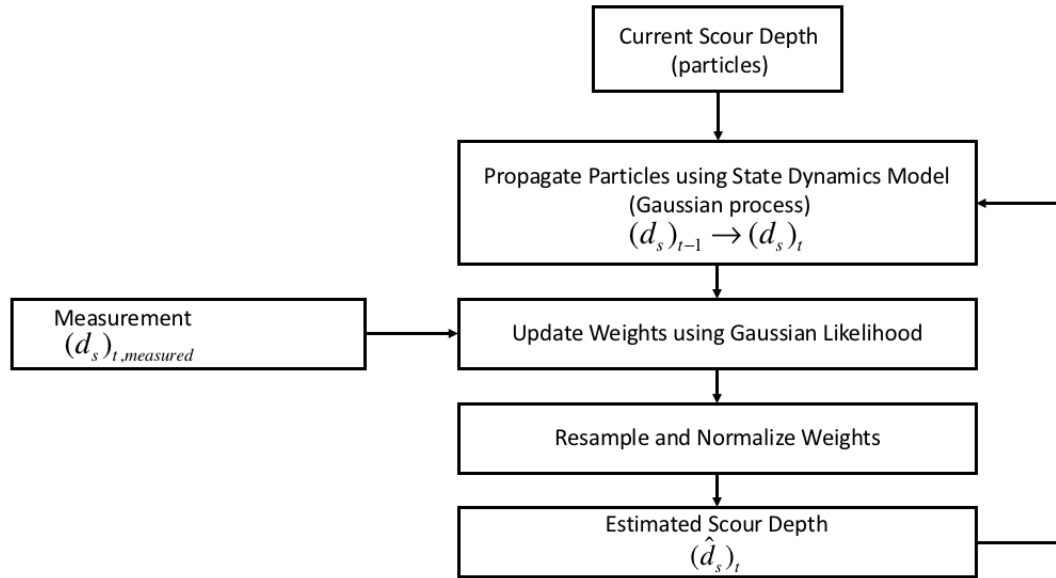
Figure 4.17 Flowchart of the Integrated Approach.

4.6.3   Results and Discussion

The particle filter uses both the predicted and measured scour depths to estimate the true scour depth at any given instant of time (Figure 4.17). Neither the measured value nor the predicted value is the true scour depth because there is an uncertainty associated with these values. The uncertainty in prediction arises from the inherent characteristics of the probabilistic data-driven model. The uncertainties in measurements occur from multiple sources such as the method used for the measurement, the field conditions etc. Cross-section measurements of the waterways are routinely taken during regular inspections and after storms. As the measurements are taken after storms, they may not take into account the refilling of sediment. In these cases, the true scour depth

158

will be greater than the measured scour depth. Another important fact is the variation of the scour depth at different locations around one pier. Therefore, it is difficult to accurately measure the scour depth using general inspection techniques. The uncertainty in measurements is a critical parameter in developing a robust prediction model. In the proposed approach, the measured and the predicted values are optimally combined using particle filters to estimate the true scour depth. This process is repeated at each time step to obtain accurate predictions of scour depth with time. Hence, it is necessary to investigate the effects of prediction and measurement uncertainties on the overall predictive capability of the algorithm. This analysis was carried out using the laboratory dataset (Hong et al. 2012).

4.6.3.1   Effect of Prediction Uncertainty

To analyze the effect of prediction uncertainty, a random error between 0-100% in the prediction of the scour rate (which corresponds to the process noise) was programmed into the algorithm and used at each time step. This error was simulated through a multiplicative term using a Gaussian white noise process at the beginning of the algorithm. The prediction of the scour depth using a 10% error in the scour rate is shown in Figure 4.18a. The line corresponding to the legend "Without Particle Filter" shows the prediction using the scour rate with error, and without applying the particle filter algorithm. This figure shows that the particle filter is able to update the predicted value close to the measurement, thus improving the accuracy. Further, the algorithm was analyzed with an error of 50% and 100% in the scour rate to demonstrate the robustness of the algorithm (Figure 4.18b and Figure 4.18c). The figures show that the estimation using the particle filter is very close to the actual scour depth, irrespective of the error in

the scour rate prediction. This is verified by the fact that the particle filter combines the measured value with the predicted value using the measured value as a reference.

(a) 10%

(b) 50%

(c) 100%
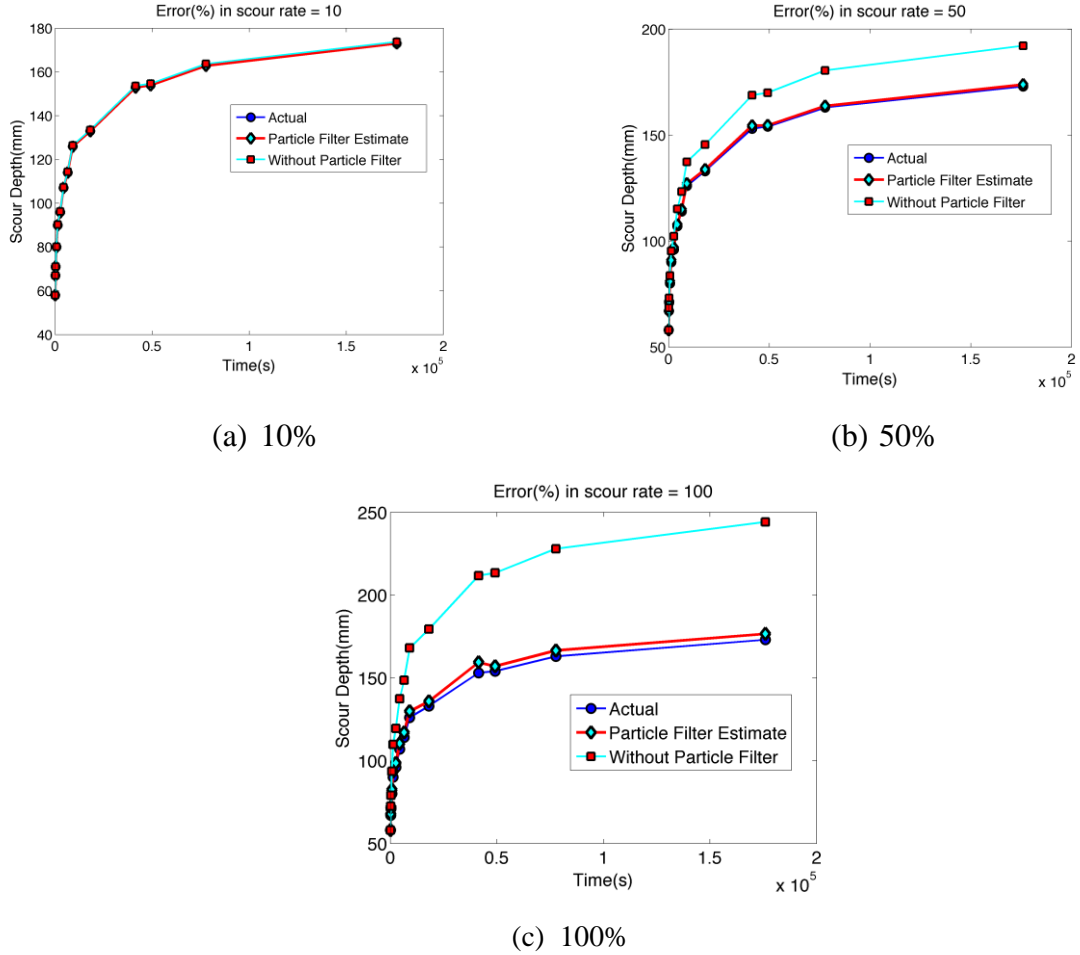
Figure 4.18 Scour Depth Prediction with Different Percentages of Error in the Scour Rate.

4.6.3.2 Effect of Measurement Uncertainty

To address the effect of measurement uncertainty, a random error with a variance between $100m^2$ -$1000m^2$ was programmed into the algorithm. The variability was chosen so that the absolute error in measured scour depth is between 15% and 35%. The variability in the measurement is: $Variability = \sqrt{Variance} * randn$, where $randn$ is a

pseudo-random number from the standard normal distribution. The measured scour depth at any time step is given in Equation 4.14 where ε indicates variability. The error in scour rate is fixed at 50% for the different variance in measurements (as this has little effect on the prediction). The prediction using a variance of 100m^2 is shown in Figure 4.19a. This figure shows the improvement in scour depth prediction using the particle filtering approach. The predictions using a variance of 600m^2 and 1000m^2 are shown in Figure 4.19b and Figure 4.19c, respectively. Figure 4.19 shows that the prediction accuracy decreases with an increase in the measurement uncertainty. This is due to the fact that the measured value is always taken as a reference in the updating step of the particle filter algorithm.
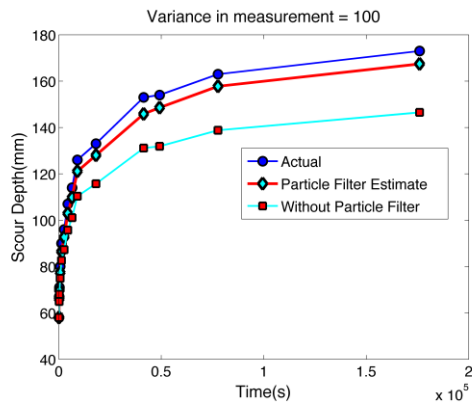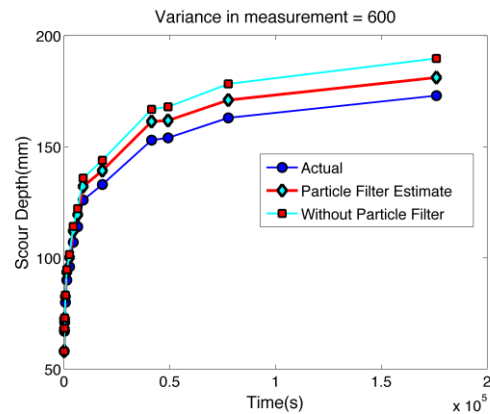
(a) 100m^2 (b) 600m^2
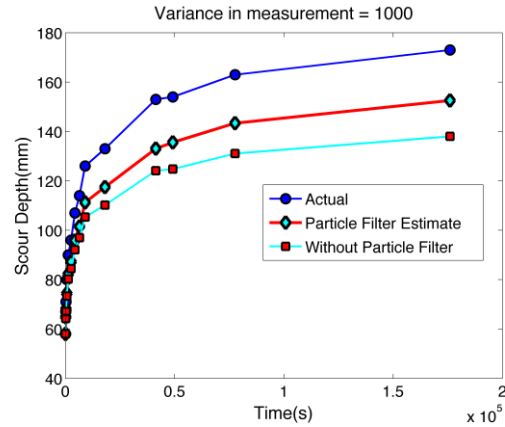
(c) $1000m^2$

Figure 4.19 Estimation of Scour Depth with Different Variances in Measurement.

4.6.3.3   One-step Ahead Prediction (Case 1)

The synthetic dataset generated was used to validate the proposed algorithm. At each time step, the predictions were made using a GP algorithm, and the predicted value is updated with the noisy measurement to estimate the actual scour depth. A dataset that had continuously varying flow conditions was created to simulate the field conditions. The disadvantage of using laboratory data is that it does not capture the variability in flow conditions at each time step. Generally, the experiments are performed using constant flow conditions for a single run. However, in field conditions, the flow conditions change constantly and therefore, it is necessary to accurately capture this phenomenon of variable flow profiles. The flow conditions for set 1 are shown in Figure 4.20. The dataset was created to incorporate both increasing and decreasing trends in all the flow parameters. A Gaussian random white noise with a mean noise to a scour depth ratio of 0.1 was added to the actual scour depth to generate the measured scour depth at each time step.
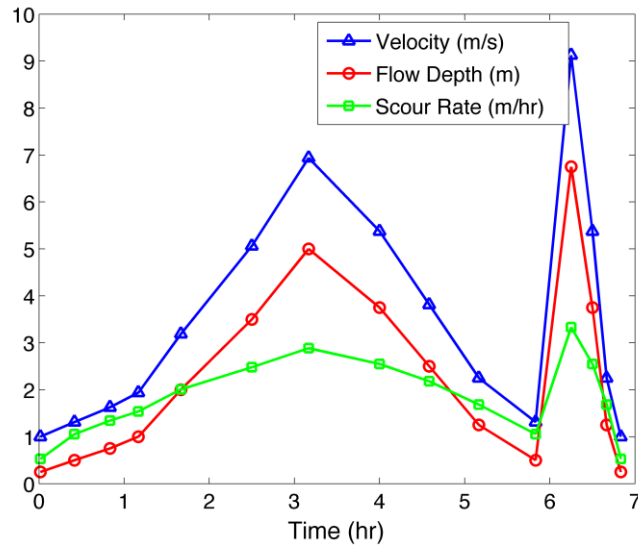
Figure 4.20 Flow Conditions Generated using Synthetic Dataset for Set 1.

Figure 4.21 and Figure 4.22 show the intermediate steps of the proposed approach. The initial distribution of particles is shown in Figure 4.21. The negative scour depth arises due to the selection of Gaussian distribution, and can be attributed to the refilling of the soil or accumulation of debris during floods. However, since the proposed algorithm uses the first few time steps for training and starts making predictions only after a few time steps, the scour depth represented as particles is always positive. At the next time step the particles are propagated based on the scour rate, which is shown in the first subplot of Figure 4.22. The second subplot shows the measured scour depth (circular marker) and the weighted estimates of each of the propagated particles around that measured scour depth. The third subplot shows the resampling of particles based on their weights and the new estimate of the scour depth (circular marker) using resampled particles and weights. The predictions at each time step using the proposed approach are shown in Figure 4.23. The gray band in this Figure is the 2-σ (95%) confidence interval

for the prediction. The results show the capability of the algorithm of predicting the scour depth under varying flow conditions with high accuracy.
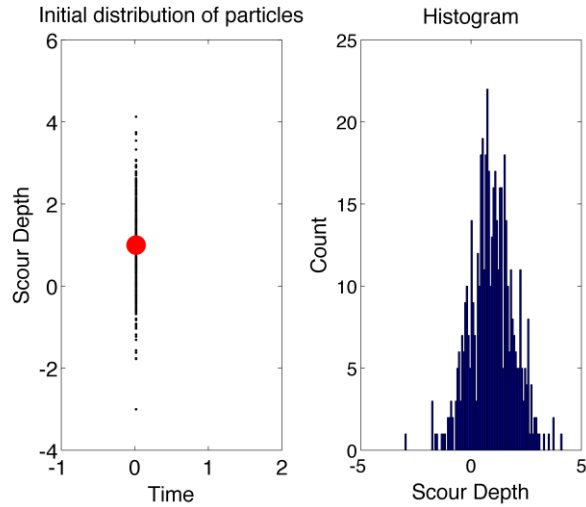
Figure 4.21 Initial Distribution and Histogram of Particles.

The algorithm was also tested using a different dataset (set 2) to verify its robustness. Figure 4.24 and Figure 4.25 show the variable flow conditions and predictions of the scour depth made using the integrated approach, respectively. The results show the capability of the algorithm to accurately predict the scour depth in the presence of both prediction and measurement uncertainties with an error of less than 5%. The error is calculated between the actual scour depth and mean of the predicted scour depth.
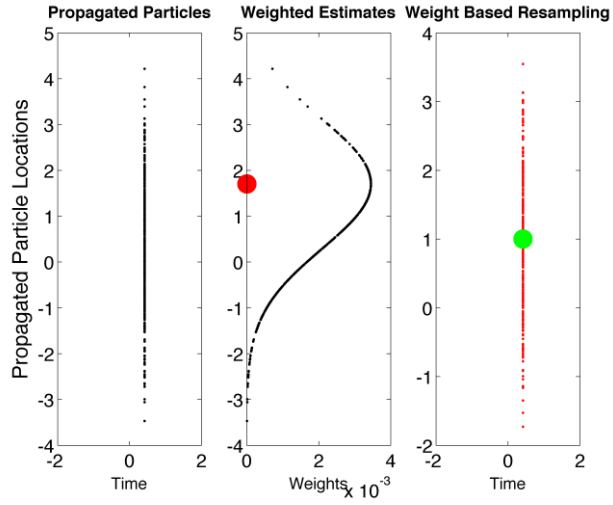
Figure 4.22 Weighted Estimates of the Particles.
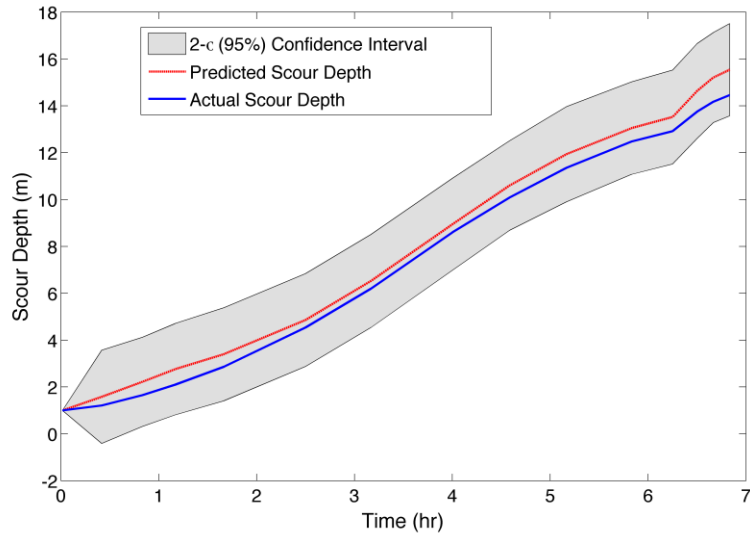
Figure 4.23 Prediction of Scour Depth using Particle Filtering Approach for Flow Conditions in Set 1.
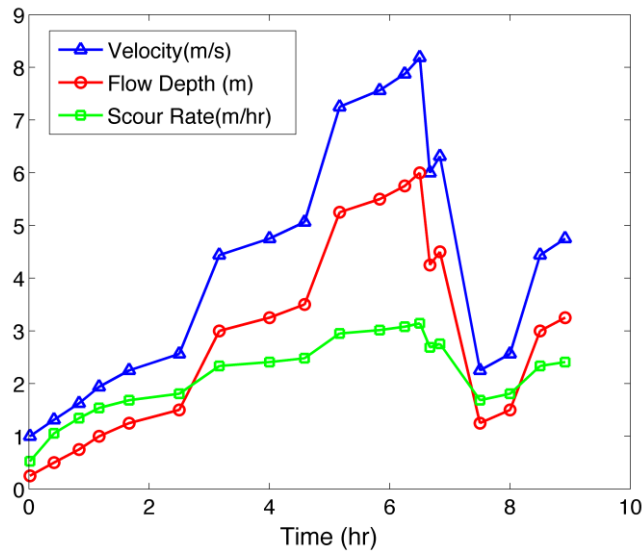
Figure 4.24 Flow Conditions Generated using Synthetic Dataset for Set 2.
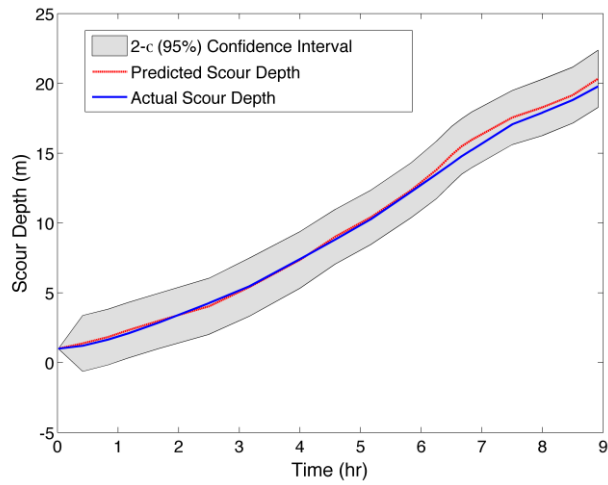
Figure 4.25 Prediction using Particle Filtering Approach for Flow Conditions in Set 2.

4.6.3.4 Multi-step Ahead Prediction (Case 2)

In the previous section, continuous predictions were made and updated using the measured values at each time step. In this section, the algorithm will be used to make scour depth predictions when measured values at some time steps are not available (case 2). It was assumed that there is no measurement of scour depth (damage state) within time T_2-T_1 (T_1 and T_2 are the arbitrary start and end of scour depth prediction) while the velocity and flow depth change significantly over the same period of time. Up to $t <= T_1$ particle filtering will be used to continuously update scour depth. However, for $T_1 < t < T_2$ the predictions of future scour depth were made as:

$$(d_s)_{T_2} = (d_s)_{T_1} + \sum_{i=1}^{n} (\dot{d}_s)_i * (\Delta t)_i + \epsilon_p, \tag{4.18}$$

where $n = \frac{T_2 - T_1}{m}$, m is the number of time steps selected by the user based on the flow conditions, $(\Delta t)_i$ is the ith time step, and $(\dot{d}_s)_i$ is the scour rate at the ith time step. The scour rate $(\dot{d}_s)_i$ is calculated from the GP model using Equation 4.9. The accuracy and confidence of the multi-step ahead predictions usually decrease with an increase in the prediction time. To improve the prediction accuracy, the scour rate predicted at the ith time step (using Equation 4.9) is added to the training set to predict the scour rate at the $(i+1)^{th}$ time step. As the prediction time increases, the training dataset increases which leads to more accurate and confident scour estimates. Figure 4.26a shows the prediction of scour depth from when the scour depth measurements are not available (T_1 = 1.8hrs and T_2 = 6.8hrs). Since only five data points were used for training the algorithm, the error in prediction of the scour depth at T_2 = 6.8hrs is relatively large. Figure 4.26b and

167

Figure 4.26c show that the error in prediction reduces significantly when more training data is used. These results show the capability of the algorithm to predict the temporal evolution of scour with an error of less than 5% with respect to the actual scour depth even when scour measurements for a period of time are not available, given enough training data.
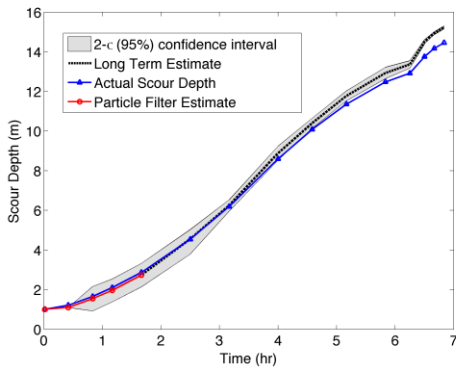
(a) $T_1 = 1.8$hrs and $T_2 = 6.8$hrs
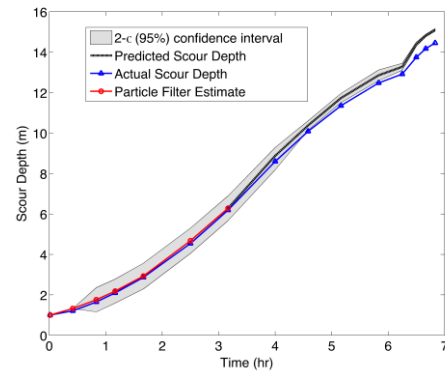
(b) $T_1 = 3$hrs and $T_2 = 6.8$hrs
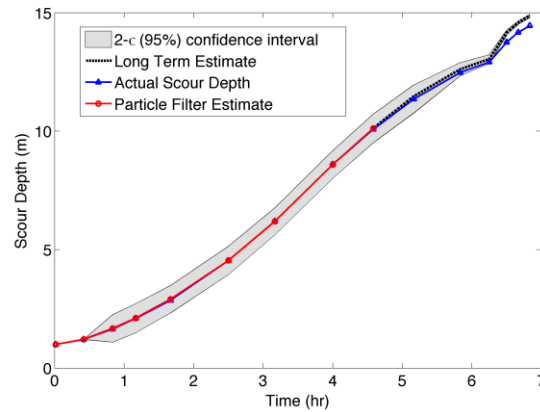
(c) $T_1 = 4.8$hrs and $T_2 = 6.8$hrs

Figure 4.26 Prediction of the Scour Depth for a Time Period when Measurements Are Not Available.

4.6.3.5 Prediction using Corrupt Training Data

In field conditions, it is often not possible to have the correct scour data to make time-dependent scour predictions. Correct scour data in this context means data such as flow depth and velocity obtained by the sensors during the scouring process. If the sensors measure the scour depths at different instances in time during scour events, those data can be used as training data to make predictions using Equation 4.9. If predictions are to be made at a bridge where previous scour data is not available, some kind of training data must be used to kick-start the algorithm. The data may come from a different bridge, with similar soil and hydrology conditions; however, in this dissertation HEC-RAS modeling (Brunner, 2001) has been used. Though both these approaches give training data that can be used to make predictions, the data has inherent inaccuracies, which translate into errors in scour depth predictions (hereinafter called "corrupt scour data"). In Section 4.6.3.3, the PF was used to continually update the measured and predicted scour depth at each time step. However, while making long-term predictions, the measurement is not available and the predictions rely solely on the state update. Therefore, using corrupt scour data will lead to erroneous results in the prediction of scour depth over long periods of time. In this section, a methodology is proposed to make accurate predictions in the presence of corrupt scour data. A new synthetic dataset was generated based on the results of Section 4.6.1 to simulate the corrupt scour data. The generated synthetic data is shown in Figure 4.27. The data was generated so that there are peaks and troughs resembling random field conditions. Both constant error and random error were added to generate the corrupt scour training data.
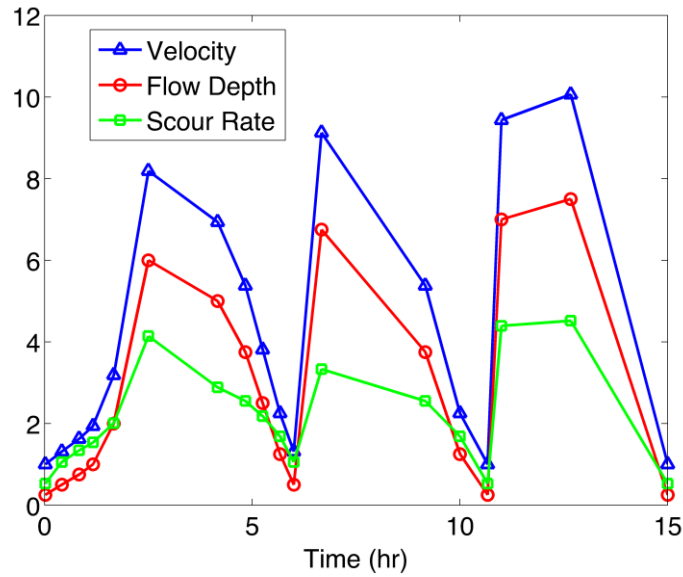
Figure 4.27 Prediction using Particle Filtering Approach for Flow Conditions in Set 2.

As shown in Section 4.2, flow depth, velocity, time, and scour depth are the parameters for the prognosis algorithm. Adding a constant error to the actual scour rate, as shown in Equation 4.19, generates the corrupt scour rate at each time instant.

$$(\dot{d}_s)_{corrupt} = (\dot{d}_s)_{actual} \pm E * \frac{(\dot{d}_s)_{actual}}{100}, \tag{4.19}$$

where E is the error (%). The scour rate $(\dot{d}_s)_i$ used in Equation 4.18 is obtained using Equation 4.9, which uses the actual scour data as the training set (D). To make predictions using corrupt scour data, a modified version of Equation 4.18 was used. If Equation 4.18 is used without correcting for the error in the scour rate, , the predicted scour depth will be significantly over-predicted or under-predicted based on whether the error is positive or negative. To correct the error in scour rate, the actual scour rate at every time instant needs to be known. However, the actual scour rate is not known in

170

field conditions since the measured scour depth values are only available. The error was calculated based on the updated scour depth values using particle filters at each time instant. The updated scour depth using particle filters at each time step is designated as $(d_s)_{t,PF}$, where PF indicates the particle filter. Similar to Section 4.6.3.4, it is assumed that the scour depth measurements are only available until time T_1. Particle filtering will be used until time $(t) < T_1$. The scour rate at time (t) was calculated as:

$$\left(\dot{d}_s\right)_{t,calc} = \frac{(d_s)_{t+\Delta t, PF} - (d_s)_{t, PF}}{\Delta t}, \qquad (4.20)$$

Once the scour rate is calculated, the error in the scour rate used for training can be calculated as:

$$E_t = \frac{\left(\dot{d}_s\right)_{t,pred} - \left(\dot{d}_s\right)_{t,calc}}{\left(\dot{d}_s\right)_{t,pred}} * 100, \qquad (4.21)$$

where $\left(\dot{d}_s\right)_{t,pred}$ is the scour rate predicted using the GP model, and the posterior is given by,

$$f\left(\left(\dot{d}_s\right)_{t,pred} \middle| \boldsymbol{D_1}, \mathbf{K_{t-1}}, \boldsymbol{\theta}\right) = \frac{1}{Z} exp\left(-\frac{\left((\dot{d}_s)_{t,pred} - \mu_{(\dot{d}_s)t,pred}\right)^2}{2\sigma^2_{(\dot{d}_s)t,pred}}\right), \qquad (4.22)$$

where, $\boldsymbol{D_1}$ is the training set that has the corrupt scour data. As the error at each time step $(\boldsymbol{E})$ is known, the average value of this error $(E_{t,avg})$ will be taken and used to correct the scour rate while making predictions. The corrected scour rate at each time step is,

$$\left(\dot{d}_s\right)_{t,corrected} = \left(\dot{d}_s\right)_{t,calc} - \frac{E_{t,avg} * \left(\dot{d}_s\right)_{t,calc}}{100}, \qquad (4.23)$$

171

The predictions are now made using the corrected scour rate as,

$$(d_s)_{T_2} = (d_s)_{T_1} + \sum_{i=1}^{n} (\dot{d}_s)_{i,corrected} * (\Delta t)_i + \epsilon_p, \qquad (4.24)$$

where $n = \frac{T_2 - T_1}{m}$, m is the arbitrary number of time steps, $(\Delta t)_i$ is the ith time step, and $(\dot{d}_s)_i$ is the scour rate at i^{th} time step.

4.6.3.5.1 Using Constant Error

A constant error was added to the actual scour data to generate corrupt training data. The plot of the actual and corrupt scour rate versus the flow depth for an error (E) of $\pm 50\%$ is shown in Figure 4.28a and Figure 4.28b. A particle filter was used to update the measured and predicted values for 7 measurements (approximately 4.2 hours in this example). Predictions were made using Equations 4.20-4.24. Figure 4.29a and Figure 4.29b show the predictions made using the training data in Figure 4.28a and Figure 4.28b respectively. The legend "Non-adaptive prediction" shows the predictions made using Equation 4.18 without correcting the error. The legend "Adaptive prediction" shows the predictions made using Equation 4.14, which uses the corrected scour rate. In Figure 4.29a, as the values of the training data are greater than the actual data, the "non-adaptive prediction" predicts a significantly larger scour depth than the actual. The "adaptive prediction" reduces the amount of over-prediction by correcting the error. Likewise, the same correction was implemented by the algorithm for the under-prediction case as shown in Figure 4.29b.
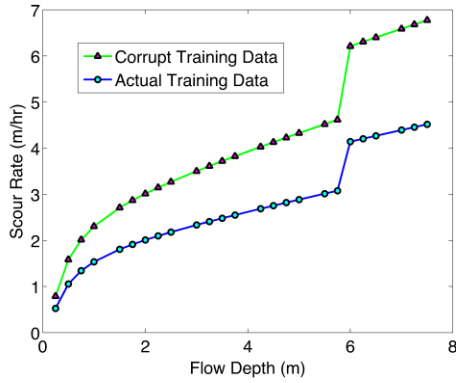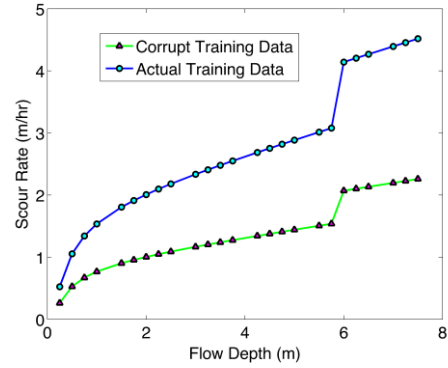
(a) +50% error   (b) -50% error

Figure 4.28 Corrupt Training Scour Data.
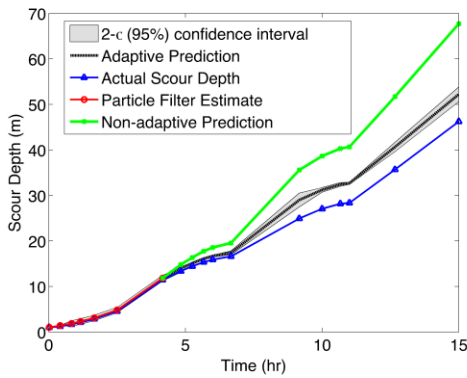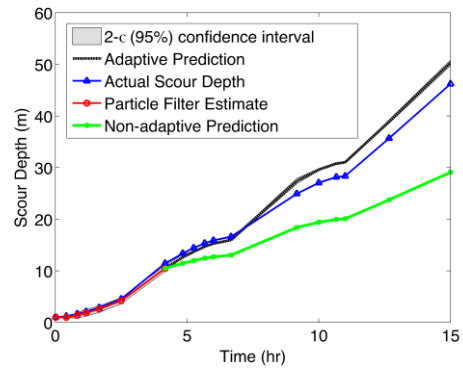
(a) +50% error   (b) -50% error

Figure 4.29 Predictions Made using Corrupt Training Data with Constant Error.

4.6.3.5.2 Using Random Error

In this section, the prediction results using a random error at each time step are presented. The corrupt scour data is generated by adding a random error with an arbitrary magnitude (e.g. between 0 and $\pm75\%$) to the actual scour data as shown in Figure 4.30a and Figure 4.30b. A pseudo random number is chosen between 0 and 75 from the scaled standard normal distribution and the multiplicative error with this magnitude is added at

173

each time step. There is no specific trend in the corrupt training data. Similar to the results of section 4.6.3.5.1, a particle filter is used to update measurements and predictions using Equation 4.14. The results of the over and under predictions are shown in Figure 4.31a and Figure 4.31b. It should be noted that in all the above cases, the amount of over-prediction after the correction using the particle filtering approach is between 10 and 25%, which is an acceptable range in field applications.

(a) between 0 and +75%   (b) between 0 and -75%
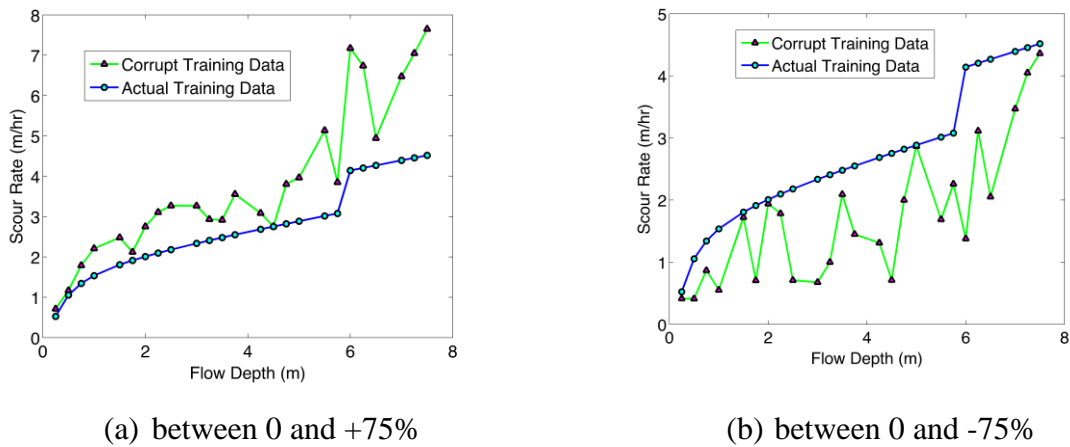
Figure 4.30 Corrupt Training Scour Data with Random Error.

(a) between 0 and +75%   (b) between 0 and -75%
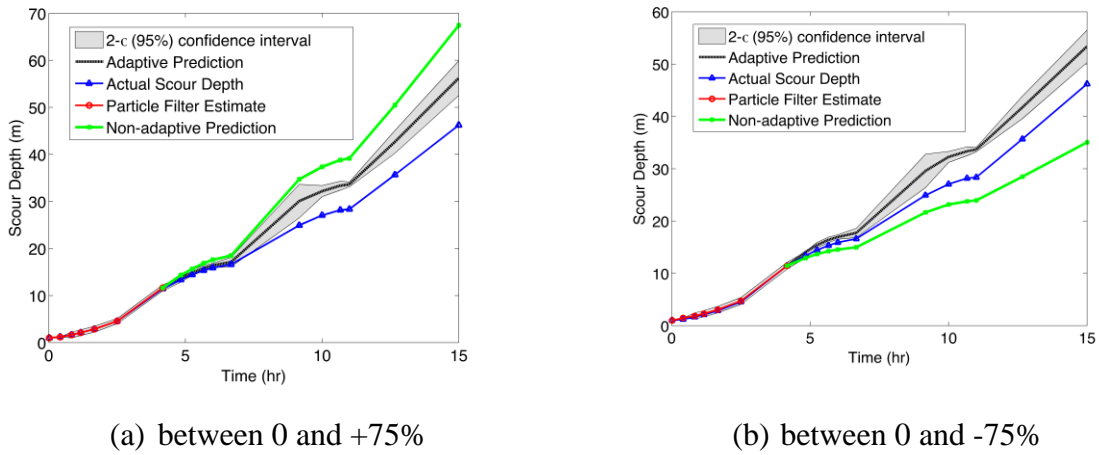
Figure 4.31 Predictions Made using Corrupt Training Data with Random Error.

174

4.7   Summary

The applicability of a probabilistic Gaussian process-based algorithm for accurate and efficient prediction of time-dependent scour has been investigated. The effect of hyper-parameter initialization on the convergence of the algorithm was examined. Three different scenarios were demonstrated to test the robustness of the algorithm. In the first case, the data containing a sudden increase in scour was considered. The algorithm was able to predict this phenomenon with an error of 8%. In the second case, the adaptability of the algorithm with increasing training data is shown. The error in the prediction decreases asymptotically as more training data becomes available. In the third case, the data was chosen so that the scour reached an equilibrium value where it does not change with the varying input conditions. The GP algorithm captured this phenomenon and predicted a constant scour depth during this period. Out of the 84 data points available, 27 data points were used to test the algorithm. A coefficient determination of 0.9821 was achieved for the training data and a value of 0.9016 was achieved for the testing set. The algorithm was tested with the field dataset. This dataset contained continually increasing and decreasing scour depth data. Out of the 66 available data points, 30 were used for testing the algorithm. A coefficient of determination of 0.9018 was achieved for the testing data and a value of 0.9715 was achieved for the training dataset. The developed GP algorithm improved the accuracy of scour prediction considerably.

To consider the measurement uncertainty associated with scour prediction, an integrated Gaussian process-based prognosis model with a particle filtering approach has been developed. The effect of measurement and prediction uncertainties on the overall predictive capability of the algorithm was studied using laboratory data. The integrated

approach was further validated with a synthetic dataset, which simulates real conditions. The synthetic dataset was created to increase the scour data and was based on the results from HEC-RAS simulations along with data available in the literature. Scour evolution predictions were made under two different case scenarios (one-step ahead and multi-step ahead) and the results show that the algorithm is capable of predicting the scour depth with an error of less than 5% for a period of 9 hours, given the accurate training data. The algorithm was validated to make predictions using arbitrary corrupt scour data. The results show that the algorithm is able to make reasonable predictions even with corrupt training data. Having more continuous measurements can be used as the training data and improve the accuracy of the prognosis model.

5 CONTRIBUTIONS AND FUTURE WORK

5.1 Contributions

The primary objective of the research presented in this dissertation was to develop an SHM framework capable of detecting damage and predicting RUL in aerospace and civil infrastructures. Six major tasks were completed towards the goal of developing a generalized SHM framework: (i) a hybrid prognosis model that integrates physics based models with machine learning algorithms to predict RUL under uniaxial loading was developed, and it accounts for loading uncertainties, such as overloads and underloads; (ii) an integrated framework that combines a localization model with the hybrid prognosis model in a sequential Bayesian framework was developed to significantly improve the crack location estimation accuracy while accounting for uncertainties in sensor data and temperature; (iii) extensive material characterization and fatigue testing was performed to study the crack propagation behavior under biaxial in-plane loads under different biaxiality ratios and phase differences; (iv) the hybrid prognosis model developed for uniaxial loading was extended to predict single and multiple crack propagation under biaxial in-phase and out-of-phase loading; (v) a Gaussian process-based prognosis model was developed to predict temporal scour near bridge piers under laboratory and field conditions; and (vi) an integrated framework was developed that combines the prognosis model with the data from RFID sensors to sequentially estimate the scour depth in presence of uncertainties in flow conditions and sensor data. This research represents substantial progress toward the development of a generalized SHM framework applicable to aerospace and civil infrastructures.

5.2 Future Work

While the research presented in this dissertation serves to improve the accuracy in damage detection and RUL prediction, further developments and advancements are necessary to maximize its applicability and effectiveness. Future work topics are essential to achieve a generalized SHM framework.

- The cross validation methodology described in Chapter 2 and Chapter 3 to improve the accuracy of predictions is performed manually by selecting values of the crack growth rate and SIF from previous experimental data or Paris' law coefficients. Trial and error is then performed to minimize the cross validation error. This procedure can be automated by incorporating an optimization subroutine into the code. The objective function would be the cross validation error with the constraints on the parameters based on experimental data or Paris' law coefficients. This will add flexibility to choose the number of data points to be used for cross validation, which will help increase the accuracy under random loading (overloads/underloads).

- The sequential Bayesian framework described in Chapter 2 and Chapter 4 uses the measured damage state as the reference to resample the particles at each step. A sequential importance sampling procedure that can automatically resample the particles based on either measurement or predicted damage states, whichever has the least uncertainty, will be useful when the measurement model has large uncertainties.

- Crack propagation under biaxial loading is a highly complex phenomenon due to the non-proportionality and phase difference of the loads. In addition, the

178

presence of overloads/underloads will further complicate the crack propagation behavior. To accurately understand the behavior, custom load spectrums, which have overload/underload excursions at specific intervals of time, can be developed to understand the local crack growth features. Electron backscatter diffraction (EBSD) can be performed to analyze the effect of grain orientations on the crack initiation and growth direction.

- For the prediction of scour near bridge piers, the measurements were generated by adding a random noise term to the actual scour depth, since no real-time scour measurement sensors are available. Although RFID sensing was described in Chapter 4, there are no algorithms to accurately predict scour depth based on the sensor data. A machine learning based model can be developed to analyze the data from distributed RFID sensors to predict and visualize the width and depth of the scour hole.

REFERENCES

Abed, L., Gasser, M., 1993. Model study of local scour downstream bridge piers, in: Hydraulic Engineering. ASCE, pp. 1738–1743.

Abràmoff, M.D., Magalhães, P.J., Ram, S.J., 2004. Image processing with ImageJ. Biophotonics Int. 11, 36–42.

Anderson, P.R.G., Garrett, G.G., 1980. Fatigue crack growth rate variations in biaxial stress fields. Int. J. Fract. 16, R111–R116. doi:10.1007/BF00013388

Arulampalam, M.S., Maskell, S., Gordon, N., Clapp, T., 2002. A tutorial on particle filters for online nonlinear/non-Gaussian Bayesian tracking. IEEE Trans. Signal Process. 50, 174–188. doi:10.1109/78.978374

Azamathulla, H.M., Deo, M.C., Deolalikar, P.B., 2008. Alternative neural networks to estimate the scour below spillways. Adv. Eng. Softw. 39, 689–698. doi:10.1016/j.advengsoft.2007.07.004

Bar-Shalom, Y., 1987. Tracking and data association. Academic Press Professional, Inc.

Bar-Shalom, Y., Daum, F., Huang, J., 2009. The probabilistic data association filter. 1 29, 82–100.

Bateni, S.M., Borghei, S.M., Jeng, D.-S., 2007. Neural network and neuro-fuzzy assessments for scour depth around bridge piers. Eng. Appl. Artif. Intell. 20, 401–414. doi:10.1016/j.engappai.2006.06.012

Bateni, S.M., Jeng, D.-S., Melville, B.W., 2007. Bayesian neural networks for prediction of equilibrium and time-dependent scour depth around bridge piers. Adv. Eng. Softw. 38, 102–111. doi:10.1016/j.advengsoft.2006.08.004

Berger, J., 1985. Statistical decision theory and Bayesian analysis.

Bertsekas, D.P., 1999. Nonlinear programming. Athena scientific Belmont.

Briaud, J.-L., Ting, F.C.K., Chen, H.C., Gudavalli, R., Perugu, S., Wei, G., 1999. SRICOS: Prediction of Scour Rate in Cohesive Soils at Bridge Piers. J. Geotech. Geoenvironmental Eng. 125, 237–246. doi:10.1061/(ASCE)1090-0241(1999)125:4(237)

Brunner, G., 2001. HEC-RAS, Hydraulic Reference Manual, Version 3.0. US Army Corps Eng. Davis CA.

Buchholz, F.-G., Chergui, A., Richard, H.A., 2004. Fracture analyses and experimental results of crack growth under general mixed mode loading conditions. Eng. Fract. Mech., Fracture and Damage Mechanics 71, 455–468. doi:10.1016/S0013-7944(03)00015-8

Carlson, R.L., Kardomateas, G.A., Bates, P.R., 1991. The effects of overloads in fatigue crack growth. Int. J. Fatigue 13, 453–460. doi:10.1016/0142-1123(91)90479-I

Chattopadhyay, A., Mohanty, S., 2011. Gaussian Process Damage Prognosis under Random and Flight Profile Fatigue Loading. Mach. Learn. Knowl. Discov. Eng. Syst. Health Manag. 181–202.

Chattopadhyay, A., Peralta, P., Papandreou-Suppappola, A., Kovvali, N., 2009. A multidisciplinary approach to structural health monitoring and damage prognosis of aerospace hotspots. Aeronaut. J. 113, 799–810.

Coelho, C.K., Das, S., Chattopadhyay, A., Papandreou-Suppappola, A., Peralta, P., 2007. Detection of fatigue cracks and torque loss in bolted joints. pp. 653204-653204–12. doi:10.1117/12.715984

Corbetta, M., Sbarufatti, C., Manes, A., Giglio, M., 2014. On Dynamic State-Space models for fatigue-induced structural degradation. Int. J. Fatigue 61, 202–219. doi:10.1016/j.ijfatigue.2013.11.008

Dahlin, P., Olsson, M., 2006. Mode I fatigue crack growth reduction mechanisms after a single Mode II load cycle. Eng. Fract. Mech. 73, 1833–1848. doi:10.1016/j.engfracmech.2006.02.015

Doucet, A., Freitas, N. de, Gordon, N., 2001. An Introduction to Sequential Monte Carlo Methods, in: Doucet, A., Freitas, N. de, Gordon, N. (Eds.), Sequential Monte Carlo Methods in Practice, Statistics for Engineering and Information Science. Springer New York, pp. 3–14.

Downing, S.D., Socie, D.F., 1982. Simple rainflow counting algorithms. Int. J. Fatigue 4, 31–40. doi:10.1016/0142-1123(82)90018-4

Erdogan, F., Sih, G.C., 1963. On the Crack Extension in Plates Under Plane Loading and Transverse Shear. J. Basic Eng. 85, 519–525. doi:10.1115/1.3656897

Ettema, R., Melville, B.W., Barkdoll, B., 1998. Scale Effect in Pier-Scour Experiments. J. Hydraul. Eng. 124, 639–642. doi:10.1061/(ASCE)0733-9429(1998)124:6(639)

Farrar, C.R., Worden, K., 2007. An introduction to structural health monitoring. Philos. Trans. R. Soc. Lond. Math. Phys. Eng. Sci. 365, 303–315.

Firat, M., Gungor, M., 2009. Generalized Regression Neural Networks and Feed Forward Neural Networks for prediction of scour depth around bridge piers. Adv. Eng. Softw. 40, 731–737. doi:10.1016/j.advengsoft.2008.12.001

Froehlich, D.C., 1989. Local scour at bridge abutments, in: Proceedings of the 1989 National Conference on Hydraulic Engineering. pp. 13–18.

Gibbs, M.N., 1998. Bayesian Gaussian processes for regression and classification. University of Cambridge.

Giurgiutiu, V., 2007. Structural health monitoring: with piezoelectric wafer active sensors. Academic Press.

Goel, A., Pal, M., 2009. Application of support vector machines in scour prediction on grade-control structures. Eng. Appl. Artif. Intell. 22, 216–223. doi:10.1016/j.engappai.2008.05.008

Gordon, N.J., Salmond, D.J., Smith, A.F., 1993. Novel approach to nonlinear/non-Gaussian Bayesian state estimation, in: Radar and Signal Processing, IEE Proceedings F. IET, pp. 107–113.

Grell, W.A., Laz, P.J., 2010. Probabilistic fatigue life prediction using AFGROW and accounting for material variability. Int. J. Fatigue 32, 1042–1049. doi:10.1016/j.ijfatigue.2009.12.001

Gudlur, P., Boczek, A., Radovic, M., Muliana, A., 2014. On characterizing the mechanical properties of aluminum–alumina composites. Mater. Sci. Eng. A 590, 352–359. doi:10.1016/j.msea.2013.10.053

Hallbäck, N., Nilsson, F., 1994. Mixed-mode I/II fracture behaviour of an aluminium alloy. J. Mech. Phys. Solids 42, 1345–1374. doi:10.1016/0022-5096(94)90001-9

Haque, M., Saif, M.A., 2002. Mechanical behavior of 30–50 nm thick aluminum films under uniaxial tension. Scr. Mater. 47, 863–867.

Harter, J., 2004. AFGROW Version 4.0009. 12, AFRL-VASM. Available Httpwww Afgrow Wpafb Af Mil.

Harter, J.A., 1999. AFGROW users guide and technical manual. AIR FORCE RESEARCH LAB WRIGHT-PATTERSON AFB OH AIR VEHICLES DIRECTORATE.

Hensberry, K., Kovvali, N., Chattopadhyay, A., 2013. Temperature-independent localization algorithm using guided wave interrogation methods. p. 86952A–86952A–15. doi:10.1117/12.2009885

Hensberry, K., Kovvali, N., Liu, K.C., Chattopadhyay, A., Papandreou-Suppappola, A., 2012. Guided Wave Based Fatigue Crack Detection and Localization in Aluminum Aerospace Structures 907–916. doi:10.1115/SMASIS2012-8241

Hestenes, M.R., Stiefel, E., 1952. Methods of conjugate gradients for solving linear systems. NBS.

Hong, J.-H., Goyal, M.K., Chiew, Y.-M., Chua, L.H.C., 2012. Predicting time-dependent pier scour depth with support vector regression. J. Hydrol. 468–469, 241–248. doi:10.1016/j.jhydrol.2012.08.038

Hopper, C., Miller, K., 1977. Fatigue crack propagation in biaxial stress fields. J. Strain Anal. Eng. Des. 12, 23–28.

Hu, W.P., Shen, Q.A., Zhang, M., Meng, Q.C., Zhang, X., 2012. Corrosion–Fatigue Life Prediction for 2024-T62 Aluminum Alloy Using Damage Mechanics-Based Approach. Int. J. Damage Mech. 21, 1245–1266. doi:10.1177/1056789511432791

Jiang, X., Adeli, H., 2004. Clustering-neural network models for freeway work zone capacity estimation. Int. J. Neural Syst. 14, 147–163.

Kermanidis, A.T., Pantelakis, S.G., 2001. Fatigue crack growth analysis of 2024 T3 aluminium specimens under aircraft service spectra. Fatigue Fract. Eng. Mater. Struct. 24, 699–710. doi:10.1046/j.1460-2695.2001.00435.x

Kim, S.B., Chattopadhyay, A., Nguyen, A.D., 2011. The use of matching pursuit decomposition for damage detection and localization in complex structures. pp. 798129-798129–9. doi:10.1117/12.880635

Kishimoto, K., Inoue, H., Hamada, M., Shibuya, T., 1995. Time Frequency Analysis of Dispersive Waves by Means of Wavelet Transform. J. Appl. Mech. 62, 841–846. doi:10.1115/1.2896009

Landers, M., Mueller, D., 1996. Evaluation of selected pier-scour equations using field data. Transp. Res. Rec. J. Transp. Res. Board 186–195.

Landers, M.N., 1992. Bridge scour data management. USGS Staff. Res. 141.

Lauth, T., Papanicolaou, A., 2008. Experimental/feasibility study of radio frequency tracers for monitoring sediment transport and scour around bridges, in: World Environmental and Water Resources Congress. pp. 12–16.

Lee, E.U., Taylor, R.E., 2011. Fatigue behavior of aluminum alloys under biaxial loading. Eng. Fract. Mech., Multiaxial FractureMultiaxial Fracture 78, 1555–1564. doi:10.1016/j.engfracmech.2010.11.005

Lim, S.-Y., Cheng, N.-S., 1998. Prediction of Live-Bed Scour at Bridge Abutments. J. Hydraul. Eng. 124, 635–638. doi:10.1061/(ASCE)0733-9429(1998)124:6(635)

Ling, Y., Mahadevan, S., 2012. Integration of structural health monitoring and fatigue damage prognosis. Mech. Syst. Signal Process. 28, 89–104.

Ling, Y., Shantz, C., Mahadevan, S., Sankararaman, S., 2011. Stochastic prediction of fatigue loading using real-time monitoring data. Int. J. Fatigue 33, 868–879. doi:10.1016/j.ijfatigue.2011.01.015

Liu, Y., Mahadevan, S., 2009. Probabilistic fatigue life prediction using an equivalent initial flaw size distribution. Int. J. Fatigue 31, 476–487. doi:10.1016/j.ijfatigue.2008.06.005

Liu, Y., Mahadevan, S., 2007a. Stochastic fatigue damage modeling under variable amplitude loading. Int. J. Fatigue 29, 1149–1161. doi:10.1016/j.ijfatigue.2006.09.009

Liu, Y., Mahadevan, S., 2007b. Threshold stress intensity factor and crack growth rate prediction under mixed-mode loading. Eng. Fract. Mech. 74, 332–345. doi:10.1016/j.engfracmech.2006.06.003

Liu, Y., Mohanty, S., Chattopadhyay, A., 2010. Condition Based Structural Health Monitoring and Prognosis of Composite Structures under Uniaxial and Biaxial Loading. J. Nondestruct. Eval. 29, 181–188. doi:10.1007/s10921-010-0076-2

Lu, Y., Ye, L., Su, Z., 2006. Crack identification in aluminium plates using Lamb wave signals of a PZT sensor network. Smart Mater. Struct. 15, 839. doi:10.1088/0964-1726/15/3/021

MacKay, D.J., 2003. Information theory, inference and learning algorithms. Cambridge university press.

Mall, S., Perel, V.Y., 2015. Crack growth behavior under biaxial fatigue with phase difference. Int. J. Fatigue 74, 166–172. doi:10.1016/j.ijfatigue.2015.01.005

Manning, R., Griffith, J.P., Pigot, T., Vernon-Harcourt, L.F., 1890. On the flow of water in open channels and pipes.

MathWorks, I., 2012a. MATLAB and Statistics Toolbox Release. Natick, MA: The MathWorks.

MathWorks, I., 2012b. MATLAB and Statistics Toolbox Release. Natick, MA: The MathWorks.

McIntosh, J., 1989. Use of scour prediction formulae, in: Proceedings of the Bridge Scour Symposium, McLean, VA, Federal Highway Administration Research Report FHWA–RD-90-035. pp. 78–100.

McMaster, F.J., Smith, D.J., 2001. Predictions of fatigue crack growth in aluminium alloy 2024–T351 using constraint factors. Int. J. Fatigue 23, Supplement 1, 93–101. doi:10.1016/S0142-1123(01)00134-7

Meischel, M., Stanzl-Tschegg, S., Arcari, A., Iyyer, N., Apetre, N., Phan, N., 2015. Constant and variable-amplitude loading of aluminum alloy 7075 in the VHCF regime. Procedia Eng. 101, 501–508.

Melville, B.W., 1997. Pier and Abutment Scour: Integrated Approach. J. Hydraul. Eng. 123, 125–136. doi:10.1061/(ASCE)0733-9429(1997)123:2(125)

Melville, B.W., 1992. Local Scour at Bridge Abutments. J. Hydraul. Eng. 118, 615–631. doi:10.1061/(ASCE)0733-9429(1992)118:4(615)

Melville, B.W., Chiew, Y.-M., 1999. Time Scale for Local Scour at Bridge Piers. J. Hydraul. Eng. 125, 59–65. doi:10.1061/(ASCE)0733-9429(1999)125:1(59)

Merati, A., Hellier, A., Zarrabi, K., 2012. On the mixed Mode II/III fatigue threshold behaviour for aluminium alloys 2014-T6 and 7075-T6. Fatigue Fract. Eng. Mater. Struct. 35, 2–12.

Mia, M.F., Nago, H., 2003. Design Method of Time-Dependent Local Scour at Circular Bridge Pier. J. Hydraul. Eng. 129, 420–427. doi:10.1061/(ASCE)0733-9429(2003)129:6(420)

Misak, H.E., Perel, V.Y., Sabelkin, V., Mall, S., 2013. Crack growth behavior of 7075-T6 under biaxial tension–tension fatigue. Int. J. Fatigue 55, 158–165. doi:10.1016/j.ijfatigue.2013.06.003

Mohamed, N., Abdelreheem, I., Abdelazim, N., 2009. Modeling local scour downstream of hydraulic structures using support vector machines (SVMs). - 1 - Proc 6 Th Int Conf. Environ. Hydrol. 1 St Symp Coast. Port Eng.

Mohanty, S., Chattopadhyay, A., Peralta, P., 2010a. Adaptive Residual Useful Life Estimation of a Structural Hotspot. J. Intell. Mater. Syst. Struct. 21, 321–335. doi:10.1177/1045389X09357972

Mohanty, S., Chattopadhyay, A., Peralta, P., Quech, D., 2010b. Fatigue damage prognosis of a cruciform structure under biaxial random and flight profile loading. p. 76490C–76490C–12. doi:10.1117/12.848814

Mohanty, S., Chattopadhyay, A., Rajadas, J.N., 2012. Dynamic Strain Mapping and Real-Time Damage-State Estimation Under Random Fatigue Loading. AIAA J. 50, 769–777.

Mueller, D.S., Wagner, C.R., 2005. Field observations and evaluations of streambed scour at bridges.

Murakami, Y., 1987. Handbook of stress intensity factors. Pergamon Press, Oxford.

Neerukatti, R.K., Fard, M.Y., Kim, I., Chattopadhyay, A., 2014a. Gaussian Process Based Prognosis Model for Bridge Scour. Int. J. Eng. Res. Technol. 3.

Neerukatti, R.K., Fard, M.Y., Kim, I., Chattopadhyay, A., 2014b. Gaussian Process Based Prognosis Model for Bridge Scour. Int. J. Eng. 3.

Neerukatti, R.K., Hensberry, K., Kovvali, N., Chattopadhyay, A., 2015. A novel probabilistic approach for damage localization and prognosis including temperature compensation. J. Intell. Mater. Syst. Struct. 1045389X15575084. doi:10.1177/1045389X15575084

Neerukatti, R.K., Kim, I., Yekani Fard, M., Chattopadhyay, A., 2013. Prediction of scour depth around bridge piers using Gaussian process. p. 86922Z–86922Z–7. doi:10.1117/12.2009901

Neerukatti, R.K., Liu, K.C., Kovvali, N., Chattopadhyay, A., 2014c. Fatigue Life Prediction Using Hybrid Prognosis for Structural Health Monitoring. J. Aerosp. Inf. Syst. 11, 211–232. doi:10.2514/1.I010094

Newman, J., 1982. Prediction of fatigue crack growth under variable-amplitude and spectrum loading using a closure model, in: Design of Fatigue and Fracture Resistant Structures. ASTM International.

Newman, J., 1981. A crack-closure model for predicting fatigue crack growth under aircraft spectrum loading, in: Methods and Models for Predicting Fatigue Crack Growth under Random Loading. ASTM International.

Newman, J.C., Jr., 1992. FASTRAN-2: A fatigue crack growth structural analysis program. NASA STIRecon Tech. Rep. N 92.

Newman, J.C.N., 1984. A crack opening stress equation for fatigue crack growth. Int. J. Fract. 24, R131–R135. doi:10.1007/BF00020751

Oh, H.-K., 1995. Characterization of dynamic fatigue life by the uniaxial tensile test. J. Mater. Process. Technol. 54, 365–371. doi:10.1016/0924-0136(94)01770-0

Ozaltun, H., Shen, M.-H.H., George, T., Cross, C., 2010. An Energy Based Fatigue Life Prediction Framework for In-Service Structural Components. Exp. Mech. 51, 707–718. doi:10.1007/s11340-010-9365-z

Pal, M., Singh, N.K., Tiwari, N.K., 2011. Support vector regression based modeling of pier scour using field data. Eng. Appl. Artif. Intell. 24, 911–916. doi:10.1016/j.engappai.2010.11.002

Papandreou-Suppappola, A., 2002. Applications in time-frequency signal processing. CRC press.

Papanicolaou, A., Elhakeem, M., Tsakiris, A., 2010. Autonomous Measurements of Bridge Pier and Abutment Scour Using Motion-Sensing Radio Transmitter.

Paris, P., Erdogan, F., 1963a. A critical analysis of crack propagation laws. J. Basic Eng. 85, 528–533.

Paris, P., Erdogan, F., 1963b. A critical analysis of crack propagation laws. J. Basic Eng. 85, 528–533.

Parola, A.C., Mahavadi, S.K., Brown, B.M., Khoury, A.E., 1996. Effects of Rectangular Foundation Geometry on Local Pier Scour. J. Hydraul. Eng. 122, 35–40. doi:10.1061/(ASCE)0733-9429(1996)122:1(35)

Payne, J., Welsh, G., Christ Jr., R.J., Nardiello, J., Papazian, J.M., 2010. Observations of fatigue crack initiation in 7075-T651. Int. J. Fatigue 32, 247–255. doi:10.1016/j.ijfatigue.2009.06.003

Raghavan, A., Cesnik, C.E.S., 2008. Effects of Elevated Temperature on Guided-wave Structural Health Monitoring. J. Intell. Mater. Syst. Struct. 19, 1383–1398. doi:10.1177/1045389X07086691

Rasmussen, C.E., Williams, C.K.I., 2006. Gaussian Processes for Machine Learning. MIT Press.

Ray, A., Patankar, R., 2001a. Fatigue crack growth under variable-amplitude loading: Part I – Model formulation in state-space setting. Appl. Math. Model. 25, 979–994. doi:10.1016/S0307-904X(01)00026-9

Ray, A., Patankar, R., 2001b. Fatigue crack growth under variable-amplitude loading: Part II – Code development and model validation. Appl. Math. Model. 25, 995–1013. doi:10.1016/S0307-904X(01)00027-0

Rice, J.R., 1968. A Path Independent Integral and the Approximate Analysis of Strain Concentration by Notches and Cracks. J. Appl. Mech. 35, 379–386. doi:10.1115/1.3601206

Richardson, E., Davis, S., 2001. Evaluating scour at bridges: Federal Highway Administration Hydraulic Engineering Circular No. 18. Publ. FHWA NHI 1–1.

Richardson, J., Richardson, E., 1994. Practical method for scour prediction at bridge piers, in: Hydraulic Engineering. ASCE, pp. 1–5.

Sankararaman, S., Ling, Y., Shantz, C., Mahadevan, S., 2009. Uncertainty quantification in fatigue damage prognosis, in: Annual Conference of the Prognostics and Health Management Society. pp. 1–13.

Schijve, J., Skorupa, M., Skorupa, A., Machniewicz, T., Gruszczynski, P., 2004. Fatigue crack growth in the aluminium alloy D16 under constant and variable amplitude loading. Int. J. Fatigue 26, 1–15. doi:10.1016/S0142-1123(03)00067-7

Sih, G.C., 1974. Strain-energy-density factor applied to mixed mode crack problems. Int. J. Fract. 10, 305–321. doi:10.1007/BF00035493

Simulia, A.U.M., 2007. Abaqus Version 6.7. 1. Dassault Systémes.

Soni, S., Kim, S.B., Chattopadhyay, A., 2010a. Fatigue crack detection and localization using reference-free method. p. 76480U–76480U–12. doi:10.1117/12.847891

Soni, S., Kim, S.B., Chattopadhyay, A., 2010b. Fatigue crack detection and localization using reference-free method, in: SPIE Smart Structures and Materials+ Nondestructive Evaluation and Health Monitoring. International Society for Optics and Photonics, p. 76480U–76480U.

Sonsino, C.M., 2001. Influence of load and deformation-controlled multiaxial tests on fatigue life to crack initiation. Int. J. Fatigue 23, 159–167. doi:10.1016/S0142-1123(00)00079-7

Srivatsan, T.S., Sriram, S., Veeraraghavan, D., Vasudevan, V.K., 1997. Microstructure, tensile deformation and fracture behaviour of aluminium alloy 7055. J. Mater. Sci. 32, 2883–2894. doi:10.1023/A:1018676501368

Stanzl-Tschegg, S., 2006. Fatigue crack growth and thresholds at ultrasonic frequencies. Int. J. Fatigue, Third International Conference on Very High Cycle Fatigue (VHCF-3)Third International Conference on Very High Cycle Fatigue 28, 1456–1464. doi:10.1016/j.ijfatigue.2005.06.058

Sunder, R., Ilchenko, B.V., 2011. Fatigue crack growth under flight spectrum loading with superposed biaxial loading due to fuselage cabin pressure. Int. J. Fatigue, Multiaxial Fatigue Models 33, 1101–1110. doi:10.1016/j.ijfatigue.2010.11.018

Suresh, S., 1998. Fatigue of materials. Cambridge university press.

Tibshirani, R., 2011. Regression shrinkage and selection via the lasso: a retrospective. J. R. Stat. Soc. Ser. B Stat. Methodol. 73, 273–282. doi:10.1111/j.1467-9868.2011.00771.x

Tipping, M.E., 2001. Sparse Bayesian Learning and the Relevance Vector Machine. J Mach Learn Res 1, 211–244. doi:10.1162/15324430152748236

Wang, P., Youn, B.D., Hu, C., 2012. A generic probabilistic framework for structural health prognostics and uncertainty management. Mech. Syst. Signal Process. 28, 622–637.

Warren, L., 2011. Scour at Bridges: Stream Stability and Scour Assessment at Bridges in Massachusetts. US Geol. Surv.

Wu, W.F., Ni, C.C., 2004. Probabilistic models of fatigue crack propagation and their experimental verification. Probabilistic Eng. Mech., Fifth International Conference on Stochastic Structural Dynamics 19, 247–257. doi:10.1016/j.probengmech.2004.02.008

Xue, Y., El Kadiri, H., Horstemeyer, M.F., Jordon, J.B., Weiland, H., 2007. Micromechanisms of multistage fatigue crack growth in a high-strength aluminum alloy. Acta Mater. 55, 1975–1984. doi:10.1016/j.actamat.2006.11.009

Zapatero, J., Domínguez, J., 1990. A statistical approach to fatigue life predictions under random loading. Int. J. Fatigue 12, 107–114. doi:10.1016/0142-1123(90)90680-D

Zhang, J., Johnston, J., Chattopadhyay, A., 2014. Physics-based multiscale damage criterion for fatigue crack prediction in aluminium alloy. Fatigue Fract. Eng. Mater. Struct. 37, 119–131.

Zhou, W., Kowali, N., Papandreou-Suppappola, A., Peralta, P., Chattopadhyay, A., 2009. Progressive damage estimation using sequential Monte Carlo techniques, in: DEStech Publications.